

# Oil & Natural Gas Technology

DOE Award No.: DE-FE0010496

## Application of Crunch-Flow Routines to Constrain Present and Past Carbon Fluxes at Gas-Hydrate Bearing Sites

### Final Scientific/Technical Report

Project Period: October 1, 2012 - January 31, 2014

Submitted by:  
Marta Torres

Oregon State University  
DUNS #: 053599908  
104 COAS Admin. Bldg.  
Corvallis, OR 97331-5503  
e-mail: mtorres@coas.oregonstate.edu  
Phone number: (541) 737-2902

Prepared for:  
United States Department of Energy  
National Energy Technology Laboratory

29 January 2014



Office of Fossil Energy

## **DISCLAIMER**

This report was prepared as an account of work sponsored by an agency of the United States Government. Neither the United States Government nor any agency thereof, nor any of their employees, makes any warranty, express or implied, or assumes any legal liability or responsibility for the accuracy, completeness, or usefulness of any information, apparatus, product, or process disclosed, or represents that its use would not infringe privately owned rights. Reference herein to any specific commercial product, process, or service by trade name, trademark, manufacturer, or otherwise does not necessarily constitute or imply its endorsement, recommendation, or favoring by the United States Government or any agency thereof. The views and opinions of authors expressed herein do not necessarily state or reflect those of the United States Government or any agency thereof.\*

## ABSTRACT

In November 2012, Oregon State University initiated the project entitled: **Application of Crunch-Flow routines to constrain present and past carbon fluxes at gas-hydrate bearing sites.** Within this project we developed Crunch-Flow based modeling modules that include important biogeochemical processes that need to be considered in gas hydrate environments. Our modules were applied to quantify carbon cycling in present and past systems, using data collected during several DOE-supported drilling expeditions, which include the Cascadia margin in US, Ulleung Basin in South Korea, and several sites drilled offshore India on the Bay of Bengal and Andaman Sea. Specifically, we completed modeling efforts that: 1) Reproduce the compositional and isotopic profiles observed at the eight drilled sites in the Ulleung Basin that constrain and contrast the carbon cycling pathways at chimney (high methane flux) and non-chimney sites (low methane, advective systems); 2) Simulate the Ba record in the sediments to quantify the past dynamics of methane flux in the southern Hydrate Ridge, Cascadia margin; and 3) Provide quantitative estimates of the thickness of individual mass transport deposits (MTDs), time elapsed after the MTD event, rate of sulfate reduction in the MTD, and time required to reach a new steady state at several sites drilled in the Krishna-Godavari (K-G) Basin off India. In addition we developed a hybrid model scheme by coupling a home-made MATLAB code with CrunchFlow to address the methane transport and chloride enrichment at the Ulleung Basins chimney sites, and contributed the modeling component to a study focusing on pore-scale controls on gas hydrate distribution in sediments from the Andaman Sea. These efforts resulted in two manuscripts currently under review, and contributed the modeling component of another paper, also under review. Lessons learned from these efforts are the basis of a mini-workshop to be held at Oregon State University (Feb 2014) to instruct graduate students (OSU and UW) as well as DOE staff from the NETL lab in Albany on the use of Crunch Flow for geochemical applications.

## TABLE OF CONTENTS

<b>I. EXECUTIVE SUMMARY</b>	<b>1</b>
<b>II. RESULTS AND DISCUSSION</b>	<b>2</b>
<b>1. Ulleung Basin carbon cycling</b>	<b>2</b>
<b>2. Cascadia margin paleo-methane flux</b>	<b>3</b>
<b>3. Gas hydrate and methane transport in the Ulleung Basin</b>	<b>3</b>
<b>4. Effect of mass transport deposits on pore water profiles in the Krishna-Godavari Basin</b>	<b>4</b>
<b>III. PRODUCTS</b>	<b>4</b>
<b>IV. APPENDIX 1.</b>	<b>6</b>
<b>Towards quantifying the reaction network around the sulfate-methane-transition-zone in the Ulleung Basin, East Sea, with a kinetic modeling approach</b>	
<b>V. APPENDIX 2-</b>	<b>50</b>
<b>Quantifying paleo-methane flux in Cascadia margin with barite record in the sediments</b>	
<b>VI. APPENDIX 3 –</b>	<b>67</b>
<b>Dynamic of gas hydrate and transport of methane gas in Ulleung Basin</b>	
<b>VII. APPENDIX 4-</b>	<b>74</b>
<b>A kinetic-model approach to quantify the effect of mass transport deposits on pore water profiles in the Krishna-Godavari Basin, Bay of Bengal</b>	

## EXECUTIVE SUMMARY

Within the DOE Award No.: DE-FE0010496, **Application of Crunch-Flow routines to constrain present and past carbon fluxes at gas-hydrate bearing sites**, we developed Crunch-Flow based modules to simulate important biogeochemical processes that need to be considered in gas hydrate environments. Kinetic model nodules were developed to: 1) Fully characterize the methane cycling at the sulfate-methane transition zone in systems in both diffusive and advective (chimney sites) flux regimes; 2) Reconstruct paleo-methane fluxes; and 3) Quantify the effect of sediment slumping on pore water profiles. We show the applicability of these modules by contributing to an additional study led by Kelly Rose, on pore-scale effects of gas hydrate distribution in the Andaman Sea.

Our efforts within the scope of this project have allowed us to better quantify the reactions involved in generation and cycling of methane in present day system, both those controlled by purely diffusive fluxes as well as those in which methane advection constitutes a significant component of the methane budgets. Model assessment of processes at play in the Ulleung Basin, Korea, revealed the very different biogeochemistry between the two environments. Organic matter decomposition is an important process for production of methane, dissolved inorganic carbon (DIC) and consumption of sulfate in the non-chimney sites while anaerobic oxidation of methane (AOM) predominates both carbon and sulfur cycles in the chimney environment. AOM is mediated by methane from different sources between the two settings. The internally produced methane, through CO<sub>2</sub> reduction (CR) and methanogenesis, fuels AOM in the non-chimney sites while AOM is primarily induced by methane from external sources in the chimney sites.

By conducting a simulation of system evolution from a non-chimney to a chimney condition by increasing the bottom methane supply, we showed that the higher CH<sub>4</sub> flux leads to a higher microbial activity of AOM, and more organic matter decomposition through methanogenesis. The higher rate ratios between AOM and CR and methanogenesis rates in the chimney sites are responsible for the isotopically lighter DIC and heavier methane in this environment relative to the non-chimney sites.

By extending the reaction network that describes the full suite of biogeochemical reactions to include precipitation/dissolution of authigenic barite we were able to reconstruct methane fluxes in the past, and differentiate the methane that is produced in-situ through methanogenesis from that supplied externally from other sources such as gas hydrate dissociation. By identifying and timing pulses of high methane flux, the model allow us to correlate these events to other known environmental perturbations (e.g. climate, slope failure, earthquakes), and thus constrain the causing mechanism(s) responsible for methane flux changes in the geologic record. The Crunch Flow model developed here is the most comprehensive model to date and is expected to be highly applicable in other regions for the purpose of quantifying paleo methane flux through the sedimentary Ba profile.

Another example of the use of Crunch Flow in understanding the role of sediment mass transport in the carbon cycle at gas hydrate bearing sites is the quantification of mass transport events in sediments from the Krishna-Godavary basin. By simulating the pore water sulfate and ammonium concentrations measured at seven sites drilled in the K-G Basin during the NGHP-01 expedition, we provide a quantitative description of how the MTDs can affect the geochemistry profiles, not only for sulfate and ammonium but potentially all pore water species. Our model provides reliable estimates of the MTDs thickness, the time elapsed after the most recent event, and the organoclastic sulfate reduction rate (RSR) at these seven sites. We also estimated the time required for the system to reach a new steady state after the MTD events. In addition our results are highly relevant in that they illustrate the potential miss-interpretations that can arise when using the pore water profiles of sites experiencing significant MTDs to infer metabolic processes. In particular, we question the postulated sulfate-reducing ammonium oxidation pathway by Schrum et al. (2009), based on the low ammonium concentration observed within the first sulfate reduction zone at Site 14A. Our model clearly shows that the aforementioned profiles instead reflect a non-steady state condition triggered by MTD in this basin.

Yet another application of this model was to quantify mineral phases that can be formed in sediments from Site 17A in the Andaman Sea, and their role in pore-scale phenomena can affect presence of gas hydrates. This study integrates field-generated datasets with newly acquired sedimentology data, physical property data, and geochemical analyses from scanning electron microscopy and grain size measurements, and mineral saturation and ion activity products of key mineral phases such as amorphous silica and calcite. This study documents the presence and nature of secondary precipitates that contributed to anomalous porosity preservation, and discuss the likely role they play to enhance permeability at Site 17A in the Andaman Sea. Though a minor component of this study, our contribution demonstrates the applicability of the Crunch Flow modules developed in this project to address other gas-hydrate related questions.

## **RESULTS AND DISCUSSION**

### **1. Ulleung Basin carbon cycling at the SMTZ**

We developed a kinetic model that simulates the composition and isotopic profiles of pore water from eight sites drilled in Ulleung Basin (offshore Korea) during the second gas hydrate drilling expedition (UBGH2) in 2010. Three sites were drilled at locations where acoustic chimneys were identified in other seismic data, and the rest were drilled on non-chimney environment. We included all necessary compositional and isotopic profiles to understand the difference between the two environments in terms of reactions involved around the sulfate-methane-transition-zone (SMTZ). We show that organic matter that is buried in a non-chimney environment is degraded in the 6-8 m thick sulfate reduction zone through POCSR, and is responsible for the majority of the DIC production in the pore water. This process consumes 40-65% of the sulfate inflow from the seafloor while the rest of sulfate reacts with the methane from beneath the SMTZ. 19-33% of the AOM is mediated by the methane produced internally through CO<sub>2</sub> reduction, which utilizes the hydrogen gas produced from pyrite formation. Methane produced by organic

matter degradation through ME can also account for 8.2-35% of the AOM rate. External methane pool contributes less than 65% of the total AOM rate in all non-chimney sites. In contrast, the strong external methane inflow dominates the consumption of sulfate and production of DIC through AOM in the chimney sites. Organic matter degradation becomes less important. While most (67-95%) of the organic matter is degraded through POCSR in the non-chimney sites, more organic matter (56-~100%) is now degraded through ME at the chimney sites due to the shrink of sulfate reduction zone (i.e., shoaling of the SMTZ). Our model experiment suggests the different response time between pore water and solid species. The depth of SMTZ rapidly responds to the increase of bottom methane flux, in the order of several thousand years, while the mode of organic matter degradation responds to such shift much slower, i.e., in the order of several tens of thousand years afterward. Such difference in response time precludes a positive feedback triggered by the methane produced through ME. These results were written on a manuscript and submitted to *Gechimica et Cosmochimica Acta*. A copy of the manuscript is included in Appendix 1

## **2. Cascadia margin paleo-methane flux**

We successfully extended our Crunch Flow model to account for the precipitation/dissolution of authigenic barite. Records of authigenic barite distribution in the sediments can be used to infer the depth of SMTZ, which can be linked to the strength of methane flux in the past. The complexity behind this effort lies in the fact that barite could be both authigenic and detrital origin. Besides, increases in methane flux could result from external sources, such as gas hydrate dissociation, or intense methanogenesis from organic matter degradation when a layer of organic matter rich sediments is deposited. It is very difficult to decouple one factor from another from the records alone. In our current kinetic model, the detrital input of barite is accounted for by a assigning boundary barite condition; in our current model this boundary condition can be time dependent. Moreover, the effect from organic matter degradation was teased out by matching the observed TOC profile. Methane produced through methanogenesis can shoal the SMTZ; however, as our model suggest, this amount of methane is not enough to account for the observed barite records and the need for an external methane source (i.e., methane inflow from outside the model regime) is established. Our model results revealed that a pulse of high methane flux occurred between 75.7 ka and 33 ka. As this period of time is sandwiched by two slope failure events and does not correlate to any specific change in paleo-oceanographic circulation, we conclude that such high methane flux is likely the result of sediment disturbance by slope failures. Full description of the model and results are given in Appendix 2

## **3. Gas hydrate and methane transport in Ulleung Basin.**

The primary goal of this project is to develop a model scheme that can simulate gas hydrate dissociation, dissolution, and formation in the shallow sediments of Ulleung Basin. This model can be constrained by pore water Cl profiles from this basin, where positive anomalies of Cl (up to 1400 mM) was observed from the depth as shallow as 25 mbsf. Cl is considered as an inert tracer since it is free from most of the biogeochemical reactions and reflects only transport processes and the amount of water in the sediments. We intended to develop the model scheme by using CrunchFlow, which was used

throughout this project to simulate various biogeochemical reactions in the sediments. However we discovered that CrunchFlow alone is not capable of dealing with this topic as some of the important properties (e.g., temperature, permeability, porosity, and Darcy velocity) are not time-dependent. CrunchFlow is still attractive to attain our project goal because of its full capability in dealing with biogeochemical reactions and its very efficient built-in mathematical engine to solve the partial differential equations. We therefore developed a hybrid model scheme by coupling a home-made MATLAB code with CrunchFlow. The MATLAB code is used to calculate all reactions and the corresponding changes in sediment and fluid properties, whereas CrunchFlow will be used to redistribute chemical species based on their transport behaviors. Such scheme will provide us the flexibility we need for our task while we can still take advantage of the computational capability and geochemistry database in CrunchFlow. Description of the model architecture and results is given in Appendix 3.

**4. Effect of mass transport deposits on pore water profiles in the Krishna-Godavari Basin, India.** Mass transfer deposits (MTDs) in the Krishna-Godavari Basin on the eastern Indian margin are common sedimentary features over the modern continental slope. Quantitative understanding of the scale and age of these MTDs is especially important when studying their triggering mechanisms and environmental feedbacks, and is also important for interpreting pore fluid chemical profiles. Pore water profiles in sediments recovered during the 2006 Indian National Gas Hydrate Project (NGHP-01) expedition suggest that MTDs are present at seven of the sites cored in the Krishna-Godavari Basin. Kinetic modeling of the S-shaped pore water sulfate profiles as well as the pore water ammonium profiles from these sites provides quantitative estimates of the thickness of individual MTDs, time elapsed after the MTD event, rate of sulfate reduction in the MTD, and time required to reach a new steady state. The model results suggest that the MTDs at the seven study sites are 8 to 25 meters thick and 300 to 1600 years old. Within the MTD sections, sulfate reduction rates are 126 to 1215 mmol/m<sup>2</sup>yr. In comparison to depth-integrated sulfate reduction rates estimated in other regions, our estimates are relatively high reflecting a much thicker sulfate reduction zone as a result of the MTDs. A positive correlation is observed between water depth and the sedimentation rate in the MTD sections (i.e., thickness of MTD divided by its age), which agrees with previous studies of MTDs in this region. We caution against using the pore water profiles of sites experiencing significant MTDs to infer metabolic processes and to quantify steady-state reaction rates as our model results confirm the remarkable influence of transient MTDs on pore water profiles. Results of this effort are given on a manuscript that will be submitted for publication as part of the JPMG special issue on gas hydrates results from the NGHP-01 drilling project offshore India, and is given in Appendix 4.

## PRODUCTS

→ This final report

→ Contributed the modeling component to a manuscript entitled “Anomalous porosity preservation and preferential accumulation of gas hydrate in the Andaman Accretionary

Wedge, NGHP-01 Site 17” by Kelly K. Rose, Joel E. Johnson, Marta E. Torres, Philip E. Long, Liviu Giosan, Evan S. Solomon, Miriam Kastner, WeiLi Hong, and H. Todd Schaef, for publication in the JMPG Special Results volume focusing on NGHP-01 results.

→ Submitted a manuscript entitled “Towards quantifying the reaction network around sulfate-methane-1 transition-zone in the Ulleung Basin, East Sea, with a kinetic modeling approach” by Wei-Li Hong, Marta E. Torres, Ji-Hoon Kim, Jiyong Choi, and Jang-Jun Bahk, for publication in *Geochimica et Comochimica Acta*

→ Submitted a second manuscript entitled “A kinetic-model approach to quantify the effect of mass transport deposits on pore water profiles in the Krishna-Godavari Basin, Bay of Bengal” by Wei-Li Hong, Evan Solomon, and Marta Torres for publication in the JMPG Special Results volume focusing on NGHP-01 results

→ A mini-workshop to be held at OSU, with the purpose of training graduate students and researchers from NETL in the use of Crunch Flow to model geochemical processes.

## **Appendix 1**

**Towards quantifying the reaction network around the sulfate-methane-transition-zone in the Ulleung Basin, East Sea, with a kinetic modeling approach**

Towards quantifying the reaction network around the sulfate-methane-transition-zone in the Ulleung Basin, East Sea, with a kinetic modeling approach

Wei-Li Hong<sup>1</sup>, Marta E. Torres<sup>1</sup>, Ji-Hoon Kim<sup>2</sup>, Jiyoung Choi<sup>2,3</sup>, Jang-Jun Bahk<sup>2</sup>

<sup>1</sup>College of Earth, Ocean, and Atmospheric Sciences, Oregon State University, 104 CEOAS administration bldg, Corvallis, OR 97331, USA

<sup>2</sup>Petroleum and Marine Research Division, Korea Institute of Geosciences and Mineral Resources, 124 Gwahang-no Yuseong-gu, Daejeon 305-350, South Korea

<sup>3</sup>Division of Marine Environment & Bioscience, Korea Maritime University, 1 Dongsam-dong, Yeongdo-gu, Busan 606-791, South Korea

## **Abstract**

We present a kinetic model based upon the pore water data collected from eight sites drilled during the second Ulleung Basin gas hydrate drilling expedition (UBGH2) in 2010. Three sites were drilled at locations where acoustic chimneys were identified in the seismic data, and the rest were drilled on non-chimney environment. We employ our model and include all necessary compositional and isotopic profiles to understand the difference between the two environments in terms of reactions involved around the sulfate-methane-transition-zone (SMTZ). Our model assessment reveals the very different biogeochemistry between the two environments. Organic matter decomposition is an important process for production of methane, dissolved inorganic carbon (DIC) and consumption of sulfate in the non-chimney sites while anaerobic oxidation of methane (AOM) predominates both carbon and sulfur cycles in the chimney environment. AOM is mediated by methane from different sources between the two settings. The internally produced methane, through CO<sub>2</sub> reduction (CR) and methanogenesis, fuels AOM in the non-chimney sites while AOM is primarily induced by methane from external sources in the chimney sites. We also conduct a simulation of system evolution from a non-chimney to a chimney condition by increasing the bottom methane supply. We show that the higher CH<sub>4</sub> flux leads to a higher microbial activity of AOM, and more organic matter decomposition through methanogenesis. The higher rate ratios between AOM and CR and

methanogenesis rates in the chimney sites are responsible for the isotopically lighter DIC and heavier methane in this environment relative to the non-chimney sites.

## Introduction

Anaerobic oxidation of methane (AOM) in marine sediments is the main reaction that prevents methane from leaking into water column and potentially the atmosphere (Barnes and Goldberg, 1976; Heeschen et al., 2005; Chuang et al., 2006; Yang et al., 2006; Reeburgh, 2007; Regnier et al., 2011). A thorough understanding of AOM is thus critical to assess the role of deep-subseafloor methane (*e.g.*, gas hydrate, gas/oil reservoirs, etc) on the carbon cycle under past, present or future environmental changes. The sulfate-methane-transition-zone (SMTZ) in marine sediments, where sulfate is exhausted and methane concentration starts to increase, is intuitively related to the strength of AOM (Borowski et al., 1996; Dickens, 2001; Chuang et al., 2010); though the actual reaction pathways can not be easily inferred from concentration profiles and may require consideration of carbon isotopic data (Borowski et al., 1997; Chatterjee et al., 2011; Hong et al., 2013).

Previous studies have already sketched a first-order picture of the many interdependent biogeochemical reactions around SMTZ (Borowski et al., 1996; Dale et al., 2006; Wallmann et al., 2006; Chatterjee et al., 2011; Regnier et al., 2011; Hong et al., 2013), and it is now widely accepted that the depth of SMTZ is controlled by the interaction of several reactions, such as organoclastic sulfate reduction (Fossing et al., 2000; Wallmann et al., 2006), CO<sub>2</sub> reduction (Borowski et al., 1997; Pohlman et al., 2008; Hong et al., 2013), and methanogenesis (Chatterjee et al., 2011). To move forward, we need a more comprehensive and quantitative understanding of how the carbon and sulfur cycles are connected at the SMTZ. Hong et al. (2013) presented a box model calculation, based on the balances of mass, flux, and isotopes of carbon, which allows for first-order estimates of the relative weight of these different reactions based on the geochemical profiles in various diffusion-dominated locations. Such calculation is, however, restricted to steady-state condition and only applicable to environments where diffusion is the dominant mechanism supplying methane to the SMTZ. In the Ulleung Basin, there are many locations where acoustic chimneys have been identified in the seismic data (*e.g.*, Haacke et al., 2009; Horozal et al., 2009; Torres et al., 2011; Yoo et al., 2013), which are known

to act as advective methane gas conduits that fuel massive gas hydrate formation near the seafloor (Torres et al., 2011; Kim et al., 2012; Choi et al., 2013).

In this work, we present a kinetic model that simulates the compositional and isotopic profiles of pore water from eight sites drilled in Ulleung Basin (offshore Korea) during the second gas hydrate drilling expedition (UBGH2) (Figure 1). We build our kinetic model using data from the five sites that are apparently diffusion-dominated, as they were drilled away from seismic blanking structures (non-chimney sites hereafter). These are the same data used by Hong et al. (2013) on their box model, and permit comparison between the steady state and kinetic model approaches. We also apply the kinetic model to three additional sites, drilled on acoustic chimneys, and represent a high methane flux end member (Torres et al., 2011; Kim et al., 2012) (chimney sites hereafter). We will compare carbon and sulfur cycles in these two environments and study the biogeochemical response of the system to an increase of methane flux.

### **Model architecture**

The model was developed using CrunchFlow, a FORTRAN routine developed by Steefel (2009) and have been applied to many other studies (Maher et al., 2009; Yang et al., 2010; Hong et al., 2013). The model setup, including the geochemical database and input file, can be found in the Appendices.

#### *Fundamental parameters*

In CrunchFlow, a global implicit scheme (GIMRT; Steefel and Yabusaki, 1996), which solves the reaction and transportation terms simultaneously in each step, is used for the diffusion dominated systems (*i.e.*, systems with low Péclet number). An explicit, operator splitting numerical scheme (OS3D; Steefel and Yabusaki, 1996), which provides better numerical stability in the environments with high Péclet numbers, is adopted as solver. CrunchFlow chooses the type of scheme automatically based on the transportation behavior of the simulation.

We chose a 20-m model frame for the non-chimney sites and a 5-m long frame for the chimney sites, such that it excludes free gas from the model regime. We ran the simulation for 400 and 100 kyr for the non-chimney and chimney sites, respectively, which are the time periods required to pass the first sediment parcel through the model frame. Although steady state is not assumed, the simulation time is long enough for all dissolved and solid species to reach steady state. We chose 15 primary species as the fundamental building blocks of the model. In addition, we selected ten secondary species, five gases, and five minerals, which can all be formulated exclusively by primary species. The full list of species considered can be found from Table 1. The porosity profiles at each site were obtained by fitting the observed profiles with the classic equation for depth-dependent porosity (Boudreau, 1997):

$$\phi(z) = \phi_f + (\phi_0 - \phi_f) \exp(\gamma z) \quad (1)$$

where  $\phi_f$  and  $\phi_0$  are the asymptotic porosity and porosity at the water-sediment interface, respectively.  $\gamma$  is an empirical constant obtained from data-fitting. These parameters are reported in Table 2. Seafloor temperature and geothermal gradient at each site (Ryu et al., 2012; Riedel et al., 2013) are also listed in Table 2. We used the formulations of Boudreau (1997) to calculate the molecular diffusion coefficients for all dissolved species at 25 °C, and a diffusion activation energy of 4.5 kcal/mol was chosen to calculate diffusion coefficients at temperatures other than 25 °C (Appendix 1). Formation factors are required to calculate the effective diffusion coefficients in the porous media. Riedel et al. (2013) used the Pickett relationship to obtain the formation factor which ranges from 1.5 to 2.3. We adopted an average value of 1.9 for our simulation. Based on the age model derived from the micro-fossil records (Yi et al., 2012), sedimentation rates were calculated and range from  $4.6 \times 10^{-5}$  to  $6.6 \times 10^{-5}$  m/yr. An average value ( $5.6 \times 10^{-5}$  m/yr) was chosen as solid burial rate for all sites. With steady-state compaction assumption, Berner (1980) showed that pore water burial rate can be related to solid burial rate through the porosity change with depth. Based on our porosity profiles, we estimated a pore water burial rate of  $3.1 \times 10^{-5}$  m/yr (55% of solid burial rate). We chose Dirichlet

type upper and lower boundary conditions and assigned them based on the measured concentrations. Bottom water composition was used as the initial condition at each site.

### *Reaction network and carbon isotopes*

Our model includes 19 reactions (Table 3). The reaction network is illustrated in Figure 2, and comprises the carbon (upper middle in Figure 2) and sulfur (lower left in Figure 2) cycles, which are linked via AOM (Eq.(17)). CO<sub>2</sub> reduction (CR, Eq.(18)), which we describe here as methane generated from the dissolved inorganic carbon (DIC) produced from both organic carbon degradation and AOM, has been commonly ignored in previous studies. Hong et al. (2013), however, has shown the significance of this reaction to achieve an isotopic mass balance of carbon around the SMTZ. Particulate organic matter (POC) is consumed via either sulfate reduction (POCSR) (Eq.(20)) or methanogenesis (ME) (Eq.(21)). Authigenic carbonate (CP, Eq.(19)) removes dissolved carbonate species from the pore water. Methane in our model can be generated in-situ through CR and ME or delivered to our modeled sediment layer by external fluid.

Hydrogen sulfide is produced from both AOM and POCSR. Formation of pyrite (Eq.(22) ) down to the depth of SMTZ has often been associated with these reactions (*e.g.*, Wallmann et al., 2006; Lim et al., 2011), but the exact formation mechanism remains controversial (Burdige, 2006). For our modeling purposes we adopted a pyrite precipitation from the less crystalline mineral mackinawite, as inferred from both theoretical calculations and lab experiments (Rickard, 1997; Rickard and Luther, 1997, 2007; Dale et al., 2009). This process fixes hydrogen sulfide from pore water and produces hydrogen gas, which supports CR. The most likely iron sources for mackinawite formation are the labile Fe oxyhydroxides. Other minerals, such as hematite may also act as Fe sources. These minerals are not included in the current model.

To correctly account for the change of alkalinity and pH, we included all major cations and anions, as well as various acid-base pairs of carbon, sulfur, nitrogen, and phosphate species (Eq. (6) to (13)). The acid-base pairs are treated as secondary species in CrunchFlow, and are assumed to reach immediate equilibrium. CH<sub>4</sub> and CO<sub>2</sub> gases are

allowed to form (Eq. (14) and (15)), but for simplicity in this current version of the model, the gas phase is pinned to the pore water and is not allowed to migrate as a separate phase and the fluid is considered to reach up to 100% saturation. Kim et al. (2012) presented evidence from carbon isotopic fractionation in support of a two-phase transport (gas and liquid) at chimney sites. We acknowledge this process but have not included this two-phase transportation in the current model.

The carbon isotopic profiles were modeled by tracking  $^{12}\text{C}$  and  $^{13}\text{C}$  in all carbon species individually. Within our formulation, the measured isotopic variability can be explained by four different processes. First, a diffusion-induced fractionation has been quantified by Zeebe and Wolf-Gladrow (2001), who showed that the diffusion coefficients are inversely proportional to the square root of the reduced masses. Secondly, isotopic changes can result in mixing of carbon with different isotopic signatures and without any isotopic fractionation. For example, DIC released from POCSR (Eq. (20)) has a constant carbon isotopic signature that is similar to the organic matter (values of -23 or -19 ‰ from Kim et al., unpublished data were used for non-chimney and chimney sites, respectively). ME (Eq. (21)) releases methane and DIC with very different isotopic signatures (Table 4) that reflects the isotopic fractionation during this reaction. The authigenic carbonate also has a constant carbon isotopic signature of -38‰ (Nehza et al., 2012). Noticeable difference in carbon isotopes was not observed from the authigenic carbonates between chimney and non-chimney sites (Nehza et al., 2012). The third type of isotopic fractionation is the equilibrium reaction between the various carbonate species, which can be as large as 9‰ between  $\text{CO}_{2(\text{aq})}$  and  $\text{HCO}_3^-$  (Mook, 1986; Zhang et al., 1995). This is accounted for in our model by including the  $^{12}\text{C}$  and  $^{13}\text{C}$  carbonate species. The last source of fractionation comes from the kinetic effect of the non-equilibrium reactions such as AOM and CR. We estimated this fractionation effect by assigning different kinetic constants for each of these reactions as detailed in the next section.

### *Reaction Formulation*

Reactions can be classified as either homogeneous or heterogeneous (Table 3).

Homogenous reactions include acid-base, gas dissolution, and aquatic redox reactions (Table 3a). Acid-base reaction and gas dissolution are described by assigning appropriate equilibrium constants (*i.e.*,  $K_a$  and  $K_H$ ) from either the CrunchFlow database or by theoretical estimates using the Zeebe and Wolf-Gladrow, (2001) approach (Appendix 2). Aquatic redox reactions (*i.e.*, AOM and CR) were formulated as double-Monod-type kinetic reactions, which require inputs for equilibrium constants ( $K_{eq}$ ), half saturation constants ( $K_{half}$ ), maximum reaction rates ( $k_{max}$ ), and inhibition constants ( $K_{in}$ ). AOM rates for  $^{12}\text{C}$  and  $^{13}\text{C}$  were formulated as follow:

$$^{12/13}R_{AOM} = ^{12/13}k_{max} \left( \frac{C_{SO_4}}{C_{SO_4} + K_{half-SO_4}} \right) \left( \frac{C_{^{12/13}CH_4}}{C_{^{12/13}CH_4} + ^{12/13}K_{half-CH_4}} \right) \left( 1 - \frac{Q}{K_{eq}} \right) \quad (2)$$

where  $C$  is the concentration of electron donors or acceptors,  $Q$  is the ion activity product,  $K_{half-SO_4}$  and  $^{12}K_{half-CH_4}$  were set to be 500  $\mu\text{M}$  (Wegener and Boetius, 2009) and 5 mM (Nauhaus et al., 2002; Vavilin, 2013), respectively.  $^{12}k_{max}$ ,  $^{13}k_{max}$  and  $^{13}K_{half-CH_4}$  were obtained from fitting curves to our data and reported in Table 4. The equilibrium constant,  $K_{eq}$ , was calculated from the standard molar Gibbs free energy ( $G_f^0$ ) of each reaction at 25 °C (Table 5). The same  $K_{eq}$  was applied for the reactions involving isotopically light and heavy methane. For the Monod type of reaction, isotopic fractionation of AOM ( $\alpha_{AOM}$ ) was defined as (Maggi and Riley, 2009):

$$\alpha_{AOM} = \frac{^{12}k_{max} \ ^{13}K_{half-CH_4}}{^{13}k_{max} \ ^{12}K_{half-CH_4}} \quad (3)$$

A fractionation factor of 1.01 (Whiticar, 1999; Holler et al., 2009) was used for all the study sites.

A similar formulation was used for CR, with an additional inhibition term that describes the suppression of the reaction by the presence of sulfate:

$${}^{12/13}R_{CR} = {}^{12/13}k_{\max} \left( \frac{C_{H_2(aq)}}{C_{H_2(aq)} + K_{half-H_2}} \right) \left( \frac{C_{{}^{12/13}HCO_3}}{C_{{}^{12/13}HCO_3} + {}^{12/13}K_{half-HCO_3}} \right) \left( 1 - \frac{Q}{K_{eq}} \right) \left( \frac{K_{in} + C_{SO_4}}{K_{in}} \right) \quad (4)$$

$K_{half-H_2}$  of 1  $\mu\text{M}$  was used (Jin and Bethke, 2005) and the rest kinetic parameters in Eq. (4) are reported in Table 4. Same expression was used to describe the fractionation for CR ( $\alpha_{CR}$ ). A constant value 1.098 was used at all sites (Whiticar, 1999; Holler et al., 2009).

Heterogeneous reactions, or water-rock interactions, include organic matter degradation, mineral precipitation/dissolution (calcite, pyrite, and mackinawite) and ammonium adsorption (Table 3b). POCSR follows Eq.(20) (Table 3b) in the sulfate reduction zone while  $\text{CH}_4$  and  $\text{CO}_2$  are produced following Eq. (21) in the methanogenesis zone (ME). These reactions were formulated as Monod-type, using the default expression in CrunchFlow. POCSR has one Monod term (half saturation constant of 100  $\mu\text{M}$  for sulfate was adopted; Wegener and Boetius, 2009), whereas ME has no Monod term but it is inhibited by sulfate, bicarbonate, and methane (Wallmann et al., 2006). Concentrations of 1.6 mM, 15 mM, and 15 mM for sulfate, bicarbonate, and methane, respectively, are inhibition constants for ME. Nutrients ( $\text{NH}_4^+$  and  $\text{HPO}_4^{2-}$ ) released during organic matter degradation follow the Redfield ratio (Park et al., 2005). The model takes into account the change of alkalinity due to the release of these nutrients. Calcite, aragonite, pyrite, and mackinawite were formulated as *tst*-type reactions in CrunchFlow. Their reaction rates are determined by their assigned saturation and the kinetic constants. Ammonium adsorption is formulated as an ion exchange reaction in CrunchFlow, adopting the Gaines-Thomas convention. The concentration of available exchange sites was expressed as the charge equivalent concentrations (CEC). The value of  $1.5 \times 10^{-4}$  equivalents/g sediments was used for CEC concentration (Rosenfeld, 1979).

### *Model-experiment setup*

To investigate how each reaction responds to an increase in methane flux, we let the model simulate the changes from the geochemical conditions of UBGH2-1\_1 (a non-chimney site) to the conditions observed in UBGH2-3 (a chimney site) by delivering more methane from the bottom of the model frame. In other words, we suddenly increase the methane concentration at the lower boundary condition. Any other modification that is necessary for the transition will also be included. The detail of this modification and the logic behind will be explained later in the *Results and Discussion* section.

### **Pore water data and geochemical environment**

The available data allow us to constrain our model results including carbon isotopes of DIC and methane (Figure 3) as well as the concentration of sulfate, calcium, magnesium, ammonium, alkalinity, hydrogen sulfide (only available in 3 sites), and pH (Figure 4). All these data and their corresponding analytic procedures have been reported elsewhere (*e.g.*, Ryu et al., 2012; Choi et al., 2013; Hong et al., 2013; Kim et al., 2013a).

At the non-chimney sites, the depth of SMTZ ranges from 5 to 10 meters below seafloor (mbsf) (Table 2), and gas hydrates occurred disseminated within the sediment or concentrated within coarse layers at depths ranging from ~70-190 mbsf (Table 2), where it occupies 12 to 79% of the pore space (Bahk et al., 2013). In contrast, the shallow depths of the SMTZ (<2 mbsf) at the three chimney sites point to a higher methane flux, where it is thought to support formation of massive gas hydrate at shallow depths (<10 mbsf) (Table 2; Torres et al., 2011; Kim et al., 2013b).

Distinct geochemical features can be observed from the isotopic profiles between the two groups. There is no significant difference in the isotopic signatures in the deep fluids and gas (>150 mbsf) among all sites (Figure 3 and Table 2). However, around the SMTZ,  $\delta^{13}\text{C-DIC}$  is ~12-20 ‰ lighter at chimney sites relative to the non-chimney sites while  $\delta^{13}\text{C-CH}_4$  is enriched (~10-15 ‰) in chimney sites. These patterns indicate that reactions around the SMTZ, rather than variations in the fluid source, are responsible for our isotopic observations.

## Results and Discussion

By fitting our model results to the available data (Figure 4), we are able to derive reaction rate profiles. From these, we calculated the depth-integrated rates in terms of DIC, methane, and hydrogen sulfide production/consumption and reported them in Table 6 and Figure 5. The difference in reaction rates between the non-chimney and chimney sites is discussed in the following paragraphs.

### *DIC cycling around SMTZ*

At all sites, we calculated a  $\Delta F_{\text{DIC}}$  parameter (Figure 5a), defined as the difference between inflow and outflow of DIC, a negative value of this parameter represents a net outflux. For all of the non-chimney sites, the DIC production rates through organic matter degradation (POCSR+ME) within the model frame are at least 76% of the  $\Delta F_{\text{DIC}}$ , indicating that the DIC produced through organic matter degradation can account for most of the observed DIC outflux. At these sites, DIC production rate via AOM is always lower than that from organic matter decomposition and accounts for only ~25 to 46% of the total  $\Delta F_{\text{DIC}}$ . On the other hand, at chimney sites, organic matter degradation contributes only slightly to the overall rate, and AOM accounts for more than 85% of the total  $\Delta F_{\text{DIC}}$ .

At the non-chimney sites, the primary pathway for organic matter degradation is POCSR, which can account for up to 96% of total organic matter degradation. At chimney sites, however, POCSR within the shallow SMTZ becomes less important. In order to fit the isotopic data at the chimney sites, it is necessary to use higher kinetic constants for ME, which in turn result in higher ME rates in this setting. These results illustrate how the shallow sulfate reduction zone typical of chimney sites in the Ulleung Basin and elsewhere, act to deliver more labile organic matter to the methanogenesis zone, where high ME rates lead to enhanced methane generation.

CR, the reaction which methane is produced by reduction of in situ DIC plus that derived from AOM, is an important sink of DIC for all sites (7-8.3%). However, the ratio of CR to AOM, which represents the portion of self-supported AOM fueled by the cycling

between AOM and CR, is remarkably different between the non-chimney and chimney sites. These ratios range from ~20 to ~30% at non-chimney sites, but are only ~10% at chimney sites. These differences indicate that CR is less important when AOM is actively fueled by high methane flux.

#### *CH<sub>4</sub> cycling around SMTZ*

Methane produced by organic matter degradation (*i.e.*, ME) within the model frame supports a fraction of the AOM at all sites (Figure 5b). At the non-chimney sites, ~8 to 35% of methane consumed by AOM comes from ME, whereas ~10 to 18% of AOM is supported by ME at chimney sites. The other internally-produced source of methane, CR, mediates about 19 to 33% of the AOM in the non-chimney sites and less than 10% in the chimney sites. This reaction describes the carbon cycling between AOM and CR, which helps stabilize the SMTZ when the methane flux is low (*i.e.*, non-chimney sites) and becomes less important when methane flux is high (*i.e.*, chimney sites). The methane that is delivered externally fuels only 37 to 57% of AOM in non-chimney sites but becomes much more important (fuels >74% of AOM) at chimney sites.

If we compare the magnitude of the external methane flux with the SMTZ depth in our sites (Figure 6a), we can observe how the external methane flux increases exponentially as SMTZ depth shoals. Such non-linear relationship was already emphasized by the global dataset of AOM rate and SMTZ depth compiled by Regnier et al. (2011). Thus, if a linear extrapolation based on the depth of SMTZ, for example, at sites UBGH2-5 and UBGH2-7 and assuming AOM is totally fueled by external methane, the external methane flux at site UBGH2-7 is only four times higher than that at site UBGH2-5. The better estimation based on our model shows that the methane flux at site UBGH2-7 is ~10 times higher than that at site UBGH2-5.

From Figure 6b, a loosely proportional relationship between external methane flux and the thickness of gas hydrate occurrence zone (GHOZ; BSR depth minus depth of first gas hydrate observed) suggests that the thickness of gas hydrate reservoir does influence the external methane flux, but factors such as lithology are also significant in controlling the

abundance and the type of gas hydrate reservoir in Ulleung Basin (Bahk et al., 2013) and elsewhere (Torres et al., 2008). A universal relationship between geochemical- or geophysical-defined boundaries (*e.g.*, SMTZ, BSR, or GHZ) and external methane fluxes as proposed by Bhatnagar et al. (2008) maybe possible but will require more information.

The source of methane from outside the model frame cannot be directly investigated by our model. However, we can make educated inferences based on the assigned boundary conditions. At chimney sites, the carbon isotopic composition of the methane present at the lower boundary conditions is similar to that reported for the gas hydrate-bounded methane recovered from the Ulleung Basin (Choi et al., 2013; Kim et al., 2013b), and it is commonly heavier than that for the non-chimney sites (Table 4). However, at all sites this isotopic signature reflects a microbial source (Choi et al., 2013; Kim et al., 2013b), suggesting that a large portion of the methane is produced by ME at depths deeper than those defined by our model frames, as suggested by Kim et al. (2011, 2012).

Furthermore, since the dimension of our simulation is intended to exclude the depth where free gas may form, it is also possible the migration of free gas phase is responsible for the high methane flux in chimney sites, as suggested by Kim et al. (2012).

#### *Sulfur cycling around SMTZ*

The entire sulfate flux from seafloor is converted to hydrogen sulfide by either POCSR or AOM within the model frame (Figure 5c). For the non-chimney sites, POCSR accounts for 40 to 65% of the total sulfate reduction but only less than 8% is consumed by POCSR in the chimney sites. Hydrogen sulfide was not measured at all sites but only at two non-chimney sites (UBGH2-1\_1 and UBGH2-10) (Figure 4a) and one chimney site (UBGH2-7) (Figure 4b). In these limited sample sets, only trace amount of hydrogen sulfide was detected, suggesting a rapid turnover rate for this species. Our model can correctly reproduce the hydrogen sulfide profiles at these sites by the removal terms that define pyrite and mackinawite formation. Precipitation of pyrite in turn produces hydrogen gas, which is required for CR, thus linking the sulfur cycle back to the carbon cycle.

In order to verify the rate of mackinawite and pyrite formation derived from our model, we estimated the solid Fe consumption rate in the shallow (<20 mbsf) sediments, using the Fe content in sediments in **piston cores** recovered from the Ulleung Basin in 2003 (Kim, 2007). Assuming a sediment bulk density of sediments is 1.35 g/cm<sup>3</sup> (Ryu et al., 2012) and a long-term sedimentation rate of 5.6×10<sup>-5</sup> m/yr (rate used in our model, Yi et al., 2012), the observed decrease in solid phase Fe of 1 wt% of Fe in the sediments is equivalent to:

$$\frac{1 \text{ (wt\%)} \times 1.35 \times 10^6 \text{ (g/m}^3\text{)} \times 5.6 \times 10^{-5} \text{ (m/yr)}}{55.8 \text{ (g / mol)}} = 0.014 \text{ (mol/m}^2\text{/yr)} \quad (5)$$

or 1.4 μmol/cm<sup>2</sup>/yr of solid Fe consumption. This value is somewhat lower than the modeled mackinawite formation rate at the non-chimney sites, which ranges from 6.21 to 8.77 μmol/cm<sup>2</sup>/yr (Table 6). Considering that the sedimentation rate used in this calculation represents a long-term average, which may underestimate the short-term rate (*i.e.*, sedimentation rate for the 20 meters), the slightly lower Fe consumption rate calculated in Eq. (5) is expected. Nonetheless, the rate is of the same order of magnitude as the mackinawite formation in the non-chimney sites derived from our model (Table 6). Such agreement not only suggests a reasonable rate estimation from our model, but also points that pyrite formation can be sustained with these newly-formed mackinawite. Although more studies are required to verify the pyrite formation process in Ulleung Basin, this rate is large enough to produce hydrogen gas and sustain the required CO<sub>2</sub> reduction inferred from the carbon isotopic records.

#### *Kinetic model vs. box model*

If we compare the reaction rate calculated by our previous box model (Hong et al., 2013) with the rates estimated by the new kinetic modeling (Figure 7), we note that both models point to an approximately equal contribution of AOM in DIC production (Figure 7a). The largest difference in terms of the absolute AOM rate was noted at site UBGH2-2\_1. The concave-downward shape of chlorinity profile at this site (Kim et al., 2013a) suggests the

presence of an advective component, such that the pure diffusion assumption used in the box model may not be valid for this site.

The importance of the CR is apparent in both models, and the absolute estimated CR rates are also similar in both models (Figure 7b). These agreements suggest that the simpler box model approach can indeed provide an adequate estimation of the CR rate and its significance to the overall AOM. In the kinetic model approach, CR has a better theoretical formulation but it also requires more input parameters (*e.g.*,  $k_{max}$ ,  $K_{half}$ , and  $K_{in}$ ), which may not always be available. When information is limited, the box model approach can provide adequate rate estimates with only one parameter needed as input (parameter  $b$  in Eq. (21) from Hong et al., 2013).

Rates of the total organic matter degradation (POCSR+ME) estimated by both model are pretty similar (Figure 7c). However, the two models suggest different modes of organic matter degradation. Most of the organic matter is degraded through ME according to the box model calculation while our kinetic model suggests otherwise. Such differences likely arise from the fact that the ME contribution in the box model is calculated based on an asymptotic carbon isotopic signature of methane, which inevitably includes the entire methanogenesis zone (*i.e.*, from within and outside the model frames). The excess ME estimated by the box model also leads to the conclusion that no or very little external methane source is required (*i.e.*,  $R_{ME}+R_{CR}$  is always greater than  $R_{AOM}$  in Table 5 from Hong et al., 2013). This inference results from the fact that external methane flux is already included in the ME rate estimated by the box model, since it includes the entire methanogenesis zone. In contrast, only the 10-15m of the methanogenesis zone is considered by the kinetic model. Such overestimation of ME rate may be avoided by using isotopic signatures that include only the depth of interest when available.

In summary, the box model approach can provide satisfactory estimation of the aqueous redox reactions (AOM and CR) but underestimate the significance of organic matter degradation. Therefore, it provides only a semi-quantitative picture of the reaction network around the SMTZ. It is useful when a crude understanding is required or the

available data is limited. Our kinetic model is more advanced in that it takes all the concentration profiles into consideration and provides more accurate estimation of the reaction rates as well the location where reactions occur.

#### *Model experiment result*

To develop an understanding of the change that a system experiences when subjected to an increase in bottom methane supply, we allowed the model to evolve from the current concentration and isotopic profiles of the non-chimney site UBGH2-1\_1 to the conditions observed at the chimney site UBGH2-3. In addition to the forced increase in bottom methane supply that characterizes chimney locations (Figure 8a, 8b, and 8c), two other modifications are required to accurately account for the observations. First, the simulation necessitates a larger AOM kinetic constant, which indicates that at high methane flux sites there is a higher microbial activity. Second, when there is more methane delivered externally to the system, more organic matter is subject to the degradation through ME rather than POCSR, due to the shoaling of the SMTZ.

If only the strength of external methane source is increased, the AOM rate calculated for the non-chimney sites is not able to keep up with the flux of methane from the bottom supply, and the model will yield an erroneous result of a high methane concentration in the sulfate reduction zone. With a higher AOM kinetic constant methane is now exhausted in the sulfate reduction zone faster and SMTZ becomes shallower. This 2-orders-of-magnitude higher AOM rate (Figure 8d and 8e) is in agreement with the higher concentration of methyl coenzyme M reductase (*mcrA*) observed at chimney sites relative to the non-chimney sites (KIGAM, 2011; Choi et al., 2013). Wegener and Boetius (2009), who studied the response of AOM strength to changes such as an increase of methane flux or fluid flow in a flow-through simulator, also observed the timely response in AOM rate to an increase of methane supply.

If only a high AOM rate fueled by the high methane flux is considered, the pH and carbon isotopes resulting from this enhanced reaction rate will not match our observations. A good fit to the data is obtained by increasing the decomposition rate of

organic matter through ME rather than POCSR (Figure 8f). This is consistent with the fact that a shallow sulfate reduction zone will limit the extent of POCSR, since the organic matter will not spend enough time in that redox zone before burial in sediments devoid of sulfate, where it is then available for ME. Collectively, these changes (lower CR to AOM ratios and higher ME rates), are responsible for the isotopically lighter DIC and heavier methane observed in the SMTZ region of the chimney sites comparing to the non-chimney sites (Figure 3).

This shift in the organic matter degradation pathways (from POCSR to ME) may result in a positive feedback to the high methane flux systems. However, due to the difference in response time between the dissolved and solid phases, such positive feedback is limited. As the external methane flux is enhanced, driven by changes in state of the deep gas reservoirs (*e.g.*, gas hydrate, pore pressure, seismicity etc), the SMTZ rapidly migrates upwards and adjusts itself to a new position, determined by the strength of the external methane flux. Such adjustment is complete in couple thousand years (2 kyr in our experiment), depending on the attendant sedimentation rate (*i.e.*, less time required if sedimentation is higher). With the sedimentation rate ( $5.6 \times 10^{-5}$  m/yr) assigned in our model, only ~10 cm of sediments will be buried during this time. However, due to the shoaling of SMTZ, more sediment is now exposed to the attack by ME. The carbon isotopic data and pH will begin to reflect the increase in ME rate after 2 kyr. The depth of SMTZ also slightly decreases in this stage (~10 cm). Due to the lower ME rate relative to the AOM rate, it takes in the order of  $10^4$  years (50 kyr in our experiment) for the system to reach steady state.

## **Conclusions**

Our kinetic model can successfully reproduce the compositional and isotopic profiles observed at the eight UBGH2 drilled sites. Striking differences in the biogeochemical processes between the chimney and non-chimney environment were revealed and illustrated in Figure 9:

Organic matter that is buried in a non-chimney environment is degraded in the 6-8 m thick sulfate reduction zone through POCSR, and is responsible for the majority of the DIC production in the pore water. This process consumes 40-65% of the sulfate inflow from the seafloor while the rest of sulfate reacts with the methane from beneath the SMTZ. 19-33% of the AOM is mediated by the methane produced internally through CO<sub>2</sub> reduction which utilizes the hydrogen gas produced from pyrite formation. Methane produced by organic matter degradation through ME can also account for 8.2-35% of the AOM rate. External methane pool contributes less than 65% of the total AOM rate in all non-chimney sites.

In contrast, the strong external methane inflow dominates the consumption of sulfate and production of DIC through AOM in the chimney sites. Organic matter degradation becomes less important. While most (67-95%) of the organic matter is degraded through POCSR in the non-chimney sites, more organic matter (56-~100%) is now degraded through ME at the chimney sites due to the shrink of sulfate reduction zone (*i.e.*, shoaling of the SMTZ). Our model experiment suggests the different response time between pore water and solid species. The depth of SMTZ rapidly responds to the increase of bottom methane flux, in the order of several thousand years, while the mode of organic matter degradation responds to such shift much slower, *i.e.*, in the order of several tens of thousand years afterward. Such difference in response time precludes a positive feedback triggered by the methane produced through ME.

From this model assessment, we conclude that the observed difference in carbon isotopic signatures between high and low methane flux conditions around SMTZ (Figure 3 and 8) is the result of lower CR to AOM rate ratio and higher ME reactivity in sites experiencing a higher methane flux.

Both the box model (Hong et al., 2013) and the kinetic model can provide similar rate estimates for both the aqueous redox reactions (AOM and CR) and the total organic matter degradation (POCSR+ME), though the two models suggest different modes of

organic matter degradation. The advantages of the current kinetic model are as follow: reactions can be better formulated based on thermodynamics and kinetic considerations, steady-state assumption is no longer necessary, and fluid advection can be better described. The kinetic model, however, requires more information than the box model, which is not always available.

### **Acknowledgements**

This project was made possible with the funding support from US Department of Energy, contract numbers: DE-FE0004000 and DOE Award No.: DE-FE0010496. In addition we acknowledge support from Korea Institute of Geosciences and Mineral Resources (KIGAM) (GP2012-026) and the Hanse-Wissenschaftskolleg, Institute for Advanced Study in Delmenhorst, Germany through a fellowship to MT during the spring of 2013.

## References

- Bahk JJ, Kim G-Y, Chun JH, Lee JY, Ryu BJ, Lee J-H, Son B-K & Collett TS (2013) Characterization of gas hydrate reservoirs in the Ulleung Basin, East Sea (Korea), by integration of core and log data. *Marine and Petroleum Geology*, *in press*.
- Barnes RO & Goldberg ED (1976) Methane production and consumption in anoxic marine-sediments. *Geology* 4: 297-300.
- Benjamin MM (2002) *Water chemistry*. McGraw-Hill New York,
- Berner RA (1980) *Early Diagenesis. A Theoretical Approach*. Princeton University Press, Princeton, N. J.
- Bhatnagar G, Chapman WG, Dickens GR, Dugan B & Hirasaki GJ (2008) Sulfate-methane transition as a proxy for average methane hydrate saturation in marine sediments. *Geophysical Research Letters* 35, L03611, doi:10.1029/2007GL032500.
- Borowski WS, Paull CK & Ussler W (1996) Marine pore-water sulfate profiles indicate in situ methane flux from underlying gas hydrate. *Geology* 24: 655-658.
- Borowski WS, Paull CK & Ussler W (1997) Carbon cycling within the upper methanogenic zone of continental rise sediments: An example from the methane-rich sediments overlying the Blake Ridge gas hydrate deposits. *Marine Chemistry* 57: 299-311.
- Boudreau BP (1997) *Diagenetic models and their implementation: modeling transport and reactions in aquatic sediments*. Springer, Berlin.
- Burdige DJ (2006) *Geochemistry of marine sediments*. Princeton University Press, Princeton New Jersey.
- Chatterjee S, Dickens GR, Bhatnagar G, Chapman WG, Dugan B, Snyder GT & Hirasaki GJ (2011) Pore water sulfate, alkalinity, and carbon isotope profiles in shallow sediment above marine gas hydrate systems: A numerical modeling perspective. *Journal of Geophysical Research-Solid Earth* 116, B09103, doi: 10.1029/2011JB008290.
- Choi J, Kim J-H, Torres ME, Hong W-L, Lee J-W, Yi BY, Bahk JJ & Lee K-E (2013) Gas origin and migration in the Ulleung Basin, East Sea; results from the Second Ulleung Basin Gas Hydrate Drilling Expedition (UBGH2). *Marine and Petroleum Geology*, *in press*.

- Chuang PC, Yang TF, Hong WL, Lin S, Sun CH, Lin ATS, Chen JC, Wang Y & Chung SH (2010) Estimation of methane flux offshore SW Taiwan and the influence of tectonics on gas hydrate accumulation. *Geofluids* 10: 497-510.
- Chuang PC, Yang TF, Lin S, Lee HF, Lan TFF, Hong WL, Liu CS, Chen JC & Wang Y (2006) Extremely high methane concentration in bottom water and cored sediments from offshore southwestern Taiwan. *Terrestrial Atmospheric and Oceanic Sciences* 17: 903-920.
- Dale AW, Bruchert V, Alperin M & Regnier P (2009) An integrated sulfur isotope model for Namibian shelf sediments. *Geochimica et Cosmochimica Acta* 73: 1924-1944.
- Dale AW, Regnier P & Van Cappellen P (2006) Bioenergetic controls on anaerobic oxidation of methane (AOM) in coastal marine sediments: A theoretical analysis. *American Journal of Science* 306: 246-294.
- Dickens GR (2001) Sulfate profiles and barium fronts in sediment on the Blake Ridge: Present and past methane fluxes through a large gas hydrate reservoir. *Geochimica et Cosmochimica Acta* 65: 529-543.
- Fossing H, Ferdelman TG & Berg P (2000) Sulfate reduction and methane oxidation in continental margin sediments influenced by irrigation (South-East Atlantic off Namibia). *Geochimica et Cosmochimica Acta* 64: 897-910.
- Haacke RR, Hyndman RD, Park KP, Yoo DG, Stoian I & Schmidt U (2009) Migration and venting of deep gases into the ocean through hydrate-choked chimneys offshore Korea. *Geology* 37: 531-534.
- Heeschen KU, Collier RW, de Angelis MA, Suess E, Rehder G, Linke P & Klinkhammer GP (2005) Methane sources, distributions, and fluxes from cold vent sites at Hydrate Ridge, Cascadia Margin. *Global Biogeochemical Cycles* 19, GB2016, doi:10.1029/2004GB002266.
- Holler T, Wegener G, Knittel K, Boetius A, Brunner B, Kuypers MMM & Widdel F (2009) Substantial C-13/C-12 and D/H fractionation during anaerobic oxidation of methane by marine consortia enriched in vitro. *Environmental Microbiology Reports* 1: 370-376.

- Hong W-L, Torres ME, Kim J-H, Choi J & Bahk J-J (2013) Carbon cycling within the sulfate-methane-transition-zone in marine sediments from the Ulleung Basin. *Biogeochemistry*, 1-20.
- Hong W-L, Torres ME & Spinelli GA (2013) Diagenetic formation and dissolution of silica cements in sediments approaching the Nankai margin subduction zone. *Geochemistry Geophysics Geosystems*, *in review*.
- Horozal S, Lee GH, Yi BY, Yoo DG, Park KP, Lee HY, Kim W, Kim HJ & Lee K (2009) Seismic indicators of gas hydrate and associated gas in the Ulleung Basin, East Sea (Japan Sea) and implications of heat flows derived from depths of the bottom-simulating reflector. *Marine Geology* 258: 126-138.
- Jin QS & Bethke CM (2005) Predicting the rate of microbial respiration in geochemical environments. *Geochimica et Cosmochimica Acta* 69: 1133-1143
- KIGAM (2011) Studies on Gas Hydrate Geology and Geochemistry. KIGAM research report (p 951). Daejeon.
- Kim JH, Park MH, Chun JH & Lee JY (2011) Molecular and isotopic signatures in sediments and gas hydrate of the central/southwestern Ulleung Basin: high alkalinity escape fuelled by biogenically sourced methane. *Geo-Marine Letters* 31: 37-49.
- Kim JH, Torres ME, Choi J, Bahk JJ, Park MH & Hong WL (2012) Inferences on gas transport based on molecular and isotopic signatures of gases at acoustic chimneys and background sites in the Ulleung Basin. *Organic Geochemistry* 43: 26-38.
- Kim J-H, Torres ME, Hong W-L, Choi J, Riedel M, Bahk JJ & Kim S-H (2013a) Pore fluid chemistry from the Second Gas Hydrate Drilling Expedition in the Ulleung Basin (UBGH2): Source, mechanisms and consequences of fluid freshening in the central part of the Ulleung Basin, East Sea. *Marine and Petroleum Geology*, *in press*.
- Kim J-H, Torres ME, Lee JY, Hong W-L, Holland M, Park M-H, Choi J & Kim G-Y (2013b) Depressurization experiment of pressure cores from the central Ulleung Basin, East Sea; insights into gas chemistry. *Organic Geochemistry*, *accepted*.

- Lim YC, Lin S, Yang TF, Chen YG & Liu CS (2011) Variations of methane induced pyrite formation in the accretionary wedge sediments offshore southwestern Taiwan. *Marine and Petroleum Geology* 28: 1829-1837.
- Maggi F & Riley WJ (2009) Transient competitive complexation in biological kinetic isotope fractionation explains nonsteady isotopic effects: Theory and application to denitrification in soils. *Journal of Geophysical Research-Biogeosciences* 114, G04012, doi: 10.1029/2008jg000878.
- Maher K, Steefel CI, White AF & Stonestrom DA (2009) The role of reaction affinity and secondary minerals in regulating chemical weathering rates at the Santa Cruz Soil Chronosequence, California. *Geochimica et Cosmochimica Acta* 73: 2804-2831.
- Mook WG (1986) C-13 in a atmospheric CO<sub>2</sub>. *Netherlands Journal of Sea Research* 20: 211-223.
- Nauhaus K, Boetius A, Kruger M & Widdel F (2002) In vitro demonstration of anaerobic oxidation of methane coupled to sulphate reduction in sediment from a marine gas hydrate area. *Environmental Microbiology* 4: 296-305.
- Nehza O, Woo KS, Chun J-H, Bahk J-J, Kim JK & Hyun S (2012) The origin of cold-water authigenic carbonates from deep-water, muddy sediments in the Ulleung Basin, East Sea of Korea. *Geosciences Journal* 16: 25-34.
- Park MH, Kim JH, Kim IS, Ryu BJ & Yu KM (2005) Tephrostratigraphy and paleo-environmental implications of Late Quaternary sediments and interstitial water in the western Ulleung Basin, East/Japan Sea. *Geo-Marine Letters* 25: 54-62.
- Pohlman JW, Ruppel C, Hutchinson DR, Downer R & Coffin RB (2008) Assessing sulfate reduction and methane cycling in a high salinity pore water system in the northern Gulf of Mexico. *Marine and Petroleum Geology* 25: 942-951.
- Reeburgh WS (2007) Oceanic methane biogeochemistry. *Chemical Reviews* 107: 486-513.
- Regnier P, Dale AW, Arndt S, LaRowe DE, Mogollon J & Van Cappellen P (2011) Quantitative analysis of anaerobic oxidation of methane (AOM) in marine sediments: A modeling perspective. *Earth-Science Reviews* 106: 105-130

- Rickard D (1997) Kinetics of pyrite formation by the H<sub>2</sub>S oxidation of iron (II) monosulfide in aqueous solutions between 25 and 125 degrees C: The rate equation. *Geochim. Cosmochim. Acta* 61: 115-134.
- Rickard D & Luther GW (1997) Kinetics of pyrite formation by the H<sub>2</sub>S oxidation of iron(II) monosulfide in aqueous solutions between 25 and 125 degrees C: The mechanism. *Geochimica et Cosmochimica Acta* 61: 135-147.
- Rickard D & Luther GW (2007) Chemistry of iron sulfides. *Chemical Reviews* 107: 514-562.
- Riedel M, Collett TS, Kim H-S, Bahk JJ, Kim J-H, Ryu BJ & Kim GY (2013) Large-scale depositional characteristics of the Ulleung Basin and its impact on electrical resistivity and Archie-parameters for gas hydrate saturation estimates. *Marine and Petroleum Geology*, *in press*.
- Rosenfeld JK (1979) Ammonium adsorption in nearshore anoxic sediments. *Limnology and Oceanography* 24: 356-364.
- Ryu B-J, Kim GY, Chun JH, Bahk JJ, Lee JY, Kim J-H, Yoo DG, Collett TS, Riedel M, Torres ME, Lee S-R & UBGH2 S (2012) Ulleung Basin Gas Hydrate Drilling Expedition 2 (UBGH2). Expedition Report (p 667). KIGAM, Daejeon.
- Steeffel CI (2009) CrunchFlow- Software for Modeling Multicomponent Reactive Flow and Transport: User's Manual, pp 91.
- Steeffel C & Yabusaki S (1996) OS3D/GIMRT, software for multicomponent-multidimensional reactive transport. User Manual and Programmer's Guide, PNL-11166. Pacific Northwest National Laboratory, Richland, WA.
- Torres ME, Kim J-H, Choi J-Y, Ryu B-J, Bahk J-J, Riedel M, Collett T, Hong W-L & Kastner M (2011) Occurrence of High Salinity Fluids Associated with Massive Near-seafloor Gas Hydrate Deposits. 7th International Conference on Gas Hydrates, Edinburgh, Scotland, United Kingdom.
- Torres ME, Trehu AM, Cespedes N, Kastner M, Wortmann UG, Kim JH, Long P, Malinverno A, Pohlman JW, Riedel M & Collett T (2008) Methane hydrate formation in turbidite sediments of northern Cascadia, IODP Expedition 311. *Earth Planet. Sci. Lett.* 271: 170-180.

- Vavilin V (2013) Estimating changes of isotopic fractionation based on chemical kinetics and microbial dynamics during anaerobic methane oxidation: apparent zero-and first-order kinetics at high and low initial methane concentrations. *Antonie van Leeuwenhoek* 103: 375-383.
- Wallmann K, Aloisi G, Haeckel M, Obzhirov A, Pavlova G & Tishchenko P (2006) Kinetics of organic matter degradation, microbial methane generation, and gas hydrate formation in anoxic marine sediments. *Geochimica et Cosmochimica Acta* 70: 3905-3927.
- Wegener G & Boetius A (2009) An experimental study on short-term changes in the anaerobic oxidation of methane in response to varying methane and sulfate fluxes. *Biogeosciences* 6: 867-876.
- Whiticar MJ (1999) Carbon and hydrogen isotope systematics of bacterial formation and oxidation of methane. *Chem. Geol.* 161: 291-314.
- Yang L, Steefel CI, Marcus MA & Bargar JR (2010) Kinetics of Fe(II)-Catalyzed Transformation of 6-line Ferrihydrite under Anaerobic Flow Conditions. *Environmental Science & Technology* 44: 5469-5475.
- Yang TF, Chuang PC, Lin S, Chen JC, Wang Y & Chung SH (2006) Methane venting in gas hydrate potential area offshore of SW Taiwan: Evidence of gas analysis of water column samples. *Terrestrial Atmospheric and Oceanic Sciences* 17: 933-950.
- Yi S, Bahk J-J, Jia H & Yoo D-G (2012) Pliocene-Pleistocene boundary determination in hemipelagic sediment from the Ulleung Basin (East Sea, offshore Korea) inferred from terrigenous and marine palynofloras. *Review of Palaeobotany and Palynology* 181: 54-63.
- Yoo DG, Kang NK, Yi BY, Kim GY, Ryu BJ, Lee K, Lee GH & Riedel M (2013) Occurrence and seismic characteristics of gas hydrate in the Ulleung Basin, East Sea. *Marine and Petroleum Geology*, *in press*.
- Zeebe RE & Wolf-Gladrow D (2001) *CO<sub>2</sub> in Seawater Equilibrium, Kinetics, Isotopes*. Elsevier Oceanography Series, Vol. 65, Elsevier Science, New York.
- Zhang J, Quay PD & Wilbur DO (1995) Carbon-isotope fractionation during gas-water exchange and dissolution of CO<sub>2</sub>. *Geochimica et Cosmochimica Acta* 59: 107-114.

Table 1: List of pore water and solid species considered in the model

<i>Primary species</i>	$\text{H}^{12}\text{CO}_3^-$	$\text{H}^{13}\text{CO}_3^-$	$^{12}\text{CH}_{4(\text{aq})}$	$^{13}\text{CH}_{4(\text{aq})}$	$\text{NH}_4^+$
	$\text{HPO}_4^{-2}$	$\text{HS}^-$	$\text{SO}_4^{-2}$	$\text{Fe}^{+2}$	$\text{H}^+$
	$\text{H}_{2(\text{aq})}$	$\text{Cl}^-$	$\text{Ca}^{+2}$	$\text{Mg}^{+2}$	$\text{Na}^+$
<i>Secondary species</i>	$^{12}\text{CO}_{2(\text{aq})}$	$^{13}\text{CO}_{2(\text{aq})}$	$^{12}\text{CO}_3^{-2}$	$^{13}\text{CO}_3^{-2}$	$\text{NH}_{3(\text{aq})}$
	$\text{H}_3\text{PO}_{3(\text{aq})}$	$\text{H}_2\text{PO}_4^-$	$\text{PO}_4^{-3}$	$\text{H}_2\text{S}_{(\text{aq})}$	$\text{S}^{-2}$
<i>Gases</i>	$^{12}\text{CO}_{2(\text{g})}$	$^{13}\text{CO}_{2(\text{g})}$	$\text{H}_2\text{S}_{(\text{g})}$	$^{12}\text{CH}_{4(\text{g})}$	$^{13}\text{CH}_{4(\text{g})}$
<i>Minerals</i>	Calcite-Ca	Calcite-Mg	$\text{CH}_2\text{O}$	Pyrite	Mackinawite

Table 2: Site-specific information<sup>2</sup>

Site	RSD <sup>3</sup> (mbar) <sup>4</sup>	Flow-GH <sup>5</sup> apparent depth (mbar) <sup>4</sup>	SMTZ depth (mbar) <sup>4</sup>	POC <sup>5</sup> concentration (%) <sup>4</sup>	$\delta^{13}C_{org}$ (‰) <sup>4</sup>	$\delta^{13}C_{org}$ (‰) <sup>4</sup>	$\delta^{13}C_{org}$ (‰) <sup>4</sup>	$\delta^{13}C_{org}$ (‰) <sup>4</sup>	$\phi$ <sup>4</sup>	$\phi$ <sup>4</sup>	$\gamma$ <sup>4</sup>	Surface temperature (°C) <sup>4</sup>	Geothermal gradient (°C/m) <sup>4</sup>
URGH2-1_1 <sup>4</sup>	365 <sup>4</sup>	93 <sup>4</sup>	7.7 <sup>4</sup>	0.62/1.03/4.03 <sup>4</sup>	-13.0 <sup>4</sup>	17.0 <sup>4</sup>	-68.3 <sup>4</sup>	-68.3 <sup>4</sup>	86.50 <sup>4</sup>	68.80 <sup>4</sup>	-0.23 <sup>4</sup>	1.3 <sup>4</sup>	0.180 <sup>4</sup>
URGH2-2_1 <sup>4</sup>	116 <sup>4</sup>	71 <sup>4</sup>	7.0 <sup>4</sup>	0.31/1.50/3.66 <sup>4</sup>	-17.0 <sup>4</sup>	22.0 <sup>4</sup>	-90.0 <sup>4</sup>	-62.0 <sup>4</sup>	81.80 <sup>4</sup>	65.80 <sup>4</sup>	-0.33 <sup>4</sup>	1.3 <sup>4</sup>	0.198 <sup>4</sup>
URGH2-3 <sup>4</sup>	188.5 <sup>4</sup>	153 <sup>4</sup>	8.0 <sup>4</sup>	0.16/1.46/3.81 <sup>4</sup>	-14.3 <sup>4</sup>	18.5 <sup>4</sup>	-87.3 <sup>4</sup>	-62.0 <sup>4</sup>	86.87 <sup>4</sup>	68.80 <sup>4</sup>	-0.25 <sup>4</sup>	1.3 <sup>4</sup>	0.096 <sup>4</sup>
URGH2-6 <sup>4</sup>	363 <sup>4</sup>	133 <sup>4</sup>	6.8 <sup>4</sup>	0.09/1.23/4.13 <sup>4</sup>	-20.3 <sup>4</sup>	17.0 <sup>4</sup>	-85.9 <sup>4</sup>	-67.3 <sup>4</sup>	86.48 <sup>4</sup>	68.80 <sup>4</sup>	-0.25 <sup>4</sup>	1.3 <sup>4</sup>	0.112 <sup>4</sup>
URGH2-8 <sup>4</sup>	171 <sup>4</sup>	71 <sup>4</sup>	6.2 <sup>4</sup>	0.21/1.80/3.44 <sup>4</sup>	-18.9 <sup>4</sup>	20.0 <sup>4</sup>	-86.6 <sup>4</sup>	-68.3 <sup>4</sup>	86.34 <sup>4</sup>	68.80 <sup>4</sup>	-0.25 <sup>4</sup>	1.3 <sup>4</sup>	0.113 <sup>4</sup>
URGH2-9 <sup>4</sup>	131.6 <sup>4</sup>	6.2 <sup>4</sup>	1.3 <sup>4</sup>	0.05/1.50 <sup>4</sup> (3.34) <sup>4</sup>	-32.5 <sup>4</sup>	20.0 <sup>4</sup>	-77.3 <sup>4</sup>	-62.0 <sup>4</sup>	83.53 <sup>4</sup>	57.80 <sup>4</sup>	-0.01 <sup>4</sup>	1.3 <sup>4</sup>	0.095 <sup>4</sup>
URGH2-7 <sup>4</sup>	124 <sup>4</sup>	6 <sup>4</sup>	2.0 <sup>4</sup>	0.61/1.56 <sup>4</sup> (3.71) <sup>4</sup>	-25.0 <sup>4</sup>	15.8 <sup>4</sup>	-67.8 <sup>4</sup>	-62.0 <sup>4</sup>	80.80 <sup>4</sup>	62.50 <sup>4</sup>	-0.015 <sup>4</sup>	1.3 <sup>4</sup>	0.171 <sup>4</sup>
URGH2-11 <sup>4</sup>	258 <sup>4</sup>	3 <sup>4</sup>	1.2 <sup>4</sup>	0.18/1.61 <sup>4</sup> (5.63) <sup>4</sup>	-31.8 <sup>4</sup>	19.5 <sup>4</sup>	-90.2 <sup>4</sup>	-62.0 <sup>4</sup>	83.80 <sup>4</sup>	65.80 <sup>4</sup>	-0.015 <sup>4</sup>	1.2 <sup>4</sup>	0.126 <sup>4</sup>

2 <sup>4</sup>Carbon isotope measurements is extremely difficult for methane at SMTZ due to the low concentration. Therefore, the lightest value was

3 chosen for approximation. <sup>4</sup>

4 <sup>4</sup>Good measurement around SMTZ was not possible for this site. An estimated value was provided. <sup>4</sup>

5 <sup>4</sup>This value is -2 mbar below the SMTZ, which may not be representative to the value at SMTZ. <sup>4</sup>

1 Table 3: Full list of reactions considered in the model

<i>(a) Homogeneous reactions</i>		<i>Abbreviation</i>	<i>Eq.#</i>
		<i>in Fig. 2-8</i>	
Acid-base	$H_2O + {}^{12/13}CO_2 \rightleftharpoons H^{12/13}CO_3^- + H^+$		(6)
	$H^{12/13}CO_3^- \rightleftharpoons {}^{12/13}CO_3^{-2} + H^+$		(7)
	$NH_4^+ \rightleftharpoons NH_{3(aq)} + H^+$		(8)
	$H_3PO_4 \rightleftharpoons H_2PO_4^-$		(9)
	$H_2PO_4^- \rightleftharpoons HPO_4^{-2}$		(10)
	$HPO_4^{-2} \rightleftharpoons PO_4^{-3}$		(11)
	$H_2S_{(aq)} \rightleftharpoons HS^- + H^+$		(12)
	$HS^- \rightleftharpoons S^{-2} + H^+$		(13)
Gas-dissolvent	${}^{12/13}CH_{4(g)} \rightleftharpoons {}^{12/13}CH_{4(aq)}$		(14)
	${}^{12/13}CO_{2(g)} \rightleftharpoons {}^{12/13}CO_{2(aq)}$		(15)
	$H_2S_{(g)} \rightleftharpoons H_2S_{(aq)}$		(16)
Aquatic redox	${}^{12/13}CH_{4(aq)} + SO_4^{-2} \rightleftharpoons H^{12/13}CO_3^- + HS^- + H_2O$	AOM	(17)
	$H^{12/13}CO_3^- + H^+ + 4H_{2(aq)} \rightleftharpoons {}^{12/13}CH_{4(aq)} + 3H_2O$	CR	(18)
<hr/>			
<i>(b) Heterogeneous reactions</i>			
Calcite	$(Ca, Mg)CO_{3(s)} + H^+ \rightleftharpoons (Mg^{+2}, Ca^{+2}) + (1-$	CP	(19)
	$a)H^{12}CO_3^- + aH^{13}CO_3^-$		
CH <sub>2</sub> O-SO <sub>4</sub>	$(CH_2O)_{106}(NH_3)_{16}(H_3PO_4) + 53SO_4^{-2} + 14H^+ \rightleftharpoons$	POCSR	(20)
	$53H_2S + (106-b)H^{12}CO_3^- + bH^{13}CO_3^- + 16NH_4^+$		
	$+ HPO_4^{-2}$		
CH <sub>2</sub> O-ME	$(CH_2O)_{106}(NH_3)_{16}(H_3PO_4) + 14H_2O$	ME	(21)
	$\rightleftharpoons (53-c)^{12}CH_4 + c^{13}CH_4 + (39-d)^{12}CO_2 + d^{13}CO_2$		
	$+ (14-e)H^{12}CO_3^- + eH^{13}CO_3^- + 16NH_4^+ + HPO_4^{-2}$		
Pyrite (FeS <sub>2(s)</sub> )	Pyrite + H <sub>2(aq)}</sub> $\rightleftharpoons$ Mackinawite + H <sub>2S(aq)}</sub>		(22)
Mackinawite (FeS <sub>(s)</sub> )	Mackinawite + H <sup>+</sup> $\rightarrow$ Fe <sup>+2</sup> + HS <sup>-</sup>		(23)
Ammonium adsorption	$NH_4^+ + MX \rightleftharpoons NH_4X + M^+$		(24)

2 Table 4: Model input parameters

	UBGH2	UBGH2	UBGH2	UBGH2	UBGH2	UBGH2	UBGH2	UBGH2
	-1-1	-2-1	-5	-6	-10	-3	-7	-11
$^{12}k_{max}$ (AOM)	5.00E-5	1.05E-4	1.90E-4	1.00E-04	1.00E-4	2.00E-3	3.00E-4	9.00E-4
$^{13}k_{max}$ (AOM)	3.96E-7	7.92E-7	1.20E-6	7.92E-07	7.92E-7	1.97E-5	2.97E-6	8.91E-6
$^{13}K_{half-CH_4}$ (AOM)	4.00E-5	3.81E-5	3.19E-5	4.00E-05	4.00E-5	4.97E-5	5.00E-5	5.00E-5
$^{12}k_{max}$ (CR)	2.35E-5	5.00E-5	5.00E-5	5.00E-05	5.00E-5	2.00E-3	5.00E-2	5.00E-2
$^{13}k_{max}$ (CR)	2.00E-7	2.73E-7	4.10E-7	3.60E-07	4.00E-7	1.28E-5	1.82E-4	5.00E-5
$^{12}K_{half-HCO_3}$ (CR)	1.00E-2	1.00E-2	1.00E-2	1.00E-02	1.00E-2	1.00E-2	1.00E-2	1.00E-2
$^{13}K_{half-HCO_3}$ (CR)	9.34E-5	6.00E-5	9.00E-5	7.91E-05	8.78E-5	7.00E-5	4.00E-5	1.10E-5
$K_{in}$ (CR)	1.00E-4	5.00E-5	1.00E-5	5.00E-05	5.00E-5	1.00E-5	2.00E-5	1.00E-5
$k_{CH_2O-SO_4}$	1E-9.6	1E-9.6	1E-9.6	1E-9.7	1E-9.4	1E-11	1E-9.6	1E-9.4
$k_{CH_2O-ME}$	1E-9.8	1E-9.1	1E-9.8	1E-9.5	1E-9.6	1E-8.1	1E-8.7	1E-8.3
$k_{Calcite-Ca}$	1E-9.7	1E-9.6	1E-9.7	1E-9.7	1E-9.2	1E-9.4	1E-9.4	1E-9.4
$k_{Calcite-Mg}$	1E-10.7	1E-10.3	1E-10.3	1E-10.9	1E-10.4	1E-10.4	1E-10.4	1E-10.4
$k_{Pyrite}$	1E-14.8	1E-14.8	1E-14.8	1E-14.8	1E-14.8	1E-15	1E-18	1E-18
$k_{Mackinawite}$	1E-8.9	1E-8.9	1E-8.9	1E-8.9	1E-8.9	1E-8.9	1E-8.9	1E-8.9
$\delta^{13}C$ of methanogenic $CH_4$	-75	-75	-75	-75	-75	-55	-55	-55
$\delta^{13}C$ of methanogenic DIC	30	30	30	30	30	50	50	50
$\delta^{13}C_{OM}$	-23	-23	-23	-23	-23	-19	-19	-19
OM content	4	4.5	4	4	5	5.5	5	5
$\delta^{13}C_{CH_4}$ lower boundary condition	-77	-70	-77	-78.6	-71.5	-67.9	-65.8	-70.3
$\delta^{13}C_{DIC}$ lower boundary condition	7.6	10.0	7.6	5.0	7.5	-8.0	-8.5	-8.5

3 Units are as follow:  $k_{max}$  in mol/kg water/yr,  $K_{half}$  in mol/kg water,  $K_{in}$  in mol/kg water,

4  $k$  in mol/m<sup>2</sup>/sec, isotopic values in ‰, and OM content in %.

- 5 Table 5: Values of Gibbs free energy used to calculate the equilibrium constants of  
6 AOM and CO<sub>2</sub> reduction (source: Benjamin, 2002).

Species	$G_f^0$ (kJ/mol)
CH <sub>4(aq)</sub>	-34.39
HCO <sub>3</sub> <sup>-</sup>	-586.8
H <sub>2(aq)</sub>	17.57
H <sup>+</sup>	0
H <sub>2</sub> O <sub>(l)</sub>	-237.18
HS <sup>-</sup>	12.05
SO <sub>4</sub> <sup>-2</sup>	-744.6

7 Table 6: Depth integrated rates for all study sites

8 (A)  $\mu\text{mol DIC}/\text{cm}^2$  porous medium/yr

	UBGH2- 1_1	UBGH2- 2_1	UBGH2- 5	UBGH2- 6	UBGH2- 10	UBGH2- 3	UBGH2- 7	UBGH2- 11
Cal-Ca	-0.88	-0.93	-0.55	-0.74	-1.63	-0.30	-0.17	-0.45
Cal-Mg	-1.01	-1.50	-1.25	-0.44	-1.00	-0.28	-0.17	-0.40
POCSR	14.94	11.85	14.77	11.12	18.54	0.10	5.22	4.60
ME	0.33	2.92	0.41	2.22	0.49	10.66	2.93	6.03
AOM	4.03	8.95	4.01	6.43	5.45	58.80	28.34	58.87
CR	-1.34	-1.71	-1.13	-1.37	-1.55	-4.94	-2.71	-4.14
DIC flux	-16.07	-19.57	-16.25	-17.23	-20.30	-64.05	-33.43	-64.52

9

10 (B)  $\mu\text{mol CH}_4/\text{cm}^2$  porous medium/yr

	UBGH2- 1_1	UBGH2- 2_1	UBGH2- 5	UBGH2- 6	UBGH2- 10	UBGH2- 3	UBGH2- 7	UBGH2- 11
ME	0.33	2.92	0.41	2.22	0.49	10.66	2.93	6.03
AOM	-4.03	-8.95	-4.01	-6.43	-5.45	-58.80	-28.34	-58.87
CR	1.34	1.71	1.13	1.37	1.55	4.94	2.71	4.14
CH <sub>4</sub> flux	2.36	4.32	2.46	2.84	3.41	43.20	22.71	48.70

11

12 (C)  $\mu\text{mol HS}^-/\text{cm}^2$  porous medium/yr

	UBGH2 -1_1	UBGH2 -2_1	UBGH2 -5	UBGH2 -6	UBGH2 -10	UBGH2 -3	UBGH2 -7	UBGH2 -11
Pyrite	-4.08	-6.10	-5.18	-5.00	-6.45	-37.92	-20.13	-44.61
Mack	-7.42	-8.77	-6.21	-6.99	-8.27	-20.93	-10.82	-16.55
POCSR	7.47	5.92	7.39	5.56	9.27	0.05	2.61	2.30
AOM	4.03	8.95	4.01	6.43	5.45	58.80	28.34	58.87
Tot SO <sub>4</sub> reduction	11.50	14.87	11.39	11.99	14.73	58.85	30.95	61.17

13

14

Figure 1

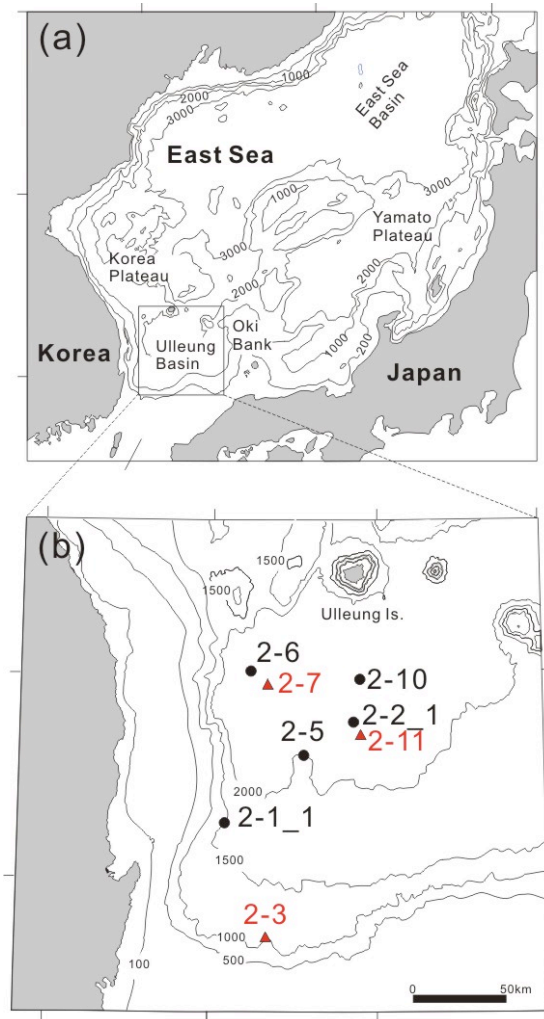


Figure 1: (a) Map of the eight sites drilled during the 2010 Ulleung Basin gas hydrate drilling expedition (UBGH2) used in this study. The three sites drilled on acoustic chimneys (Torres et al., 2011) were plotted in red triangles. (b) Profiles illustrating seismic characteristics of non chimney (UBGH2-1\_1) and acoustic chimney (UBGH2-3) sites.

Figure 2

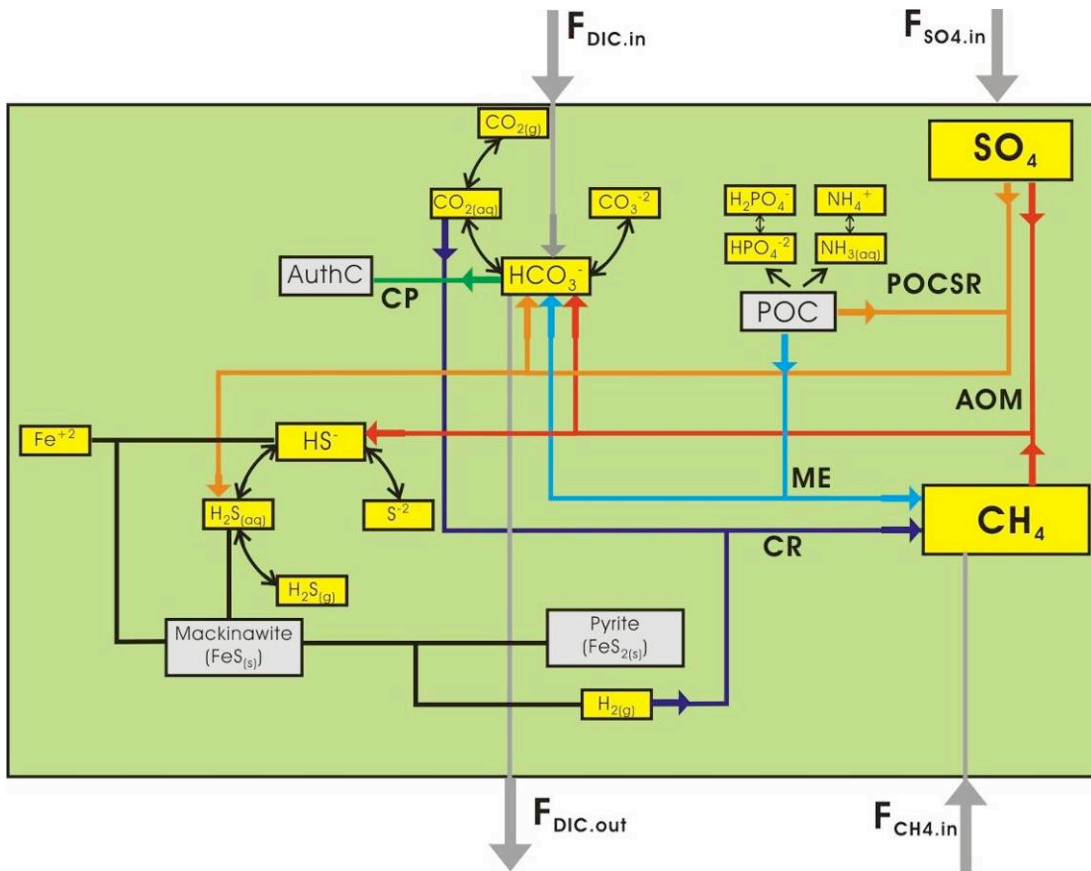


Figure 2: Reaction network considered in our kinetic model. Dissolved species are denoted by yellow boxes and solids are shown in grey. Grey lines and arrows show the input/output of DIC, sulfate, and methane from outside the model domain. The five principal reactions (AOM, CR, POCSR, ME, and CP) are labeled by arrows with different colors. These are the same reactions considered in Hong et al. (2013) and are listed in Table 3.

Figure 3

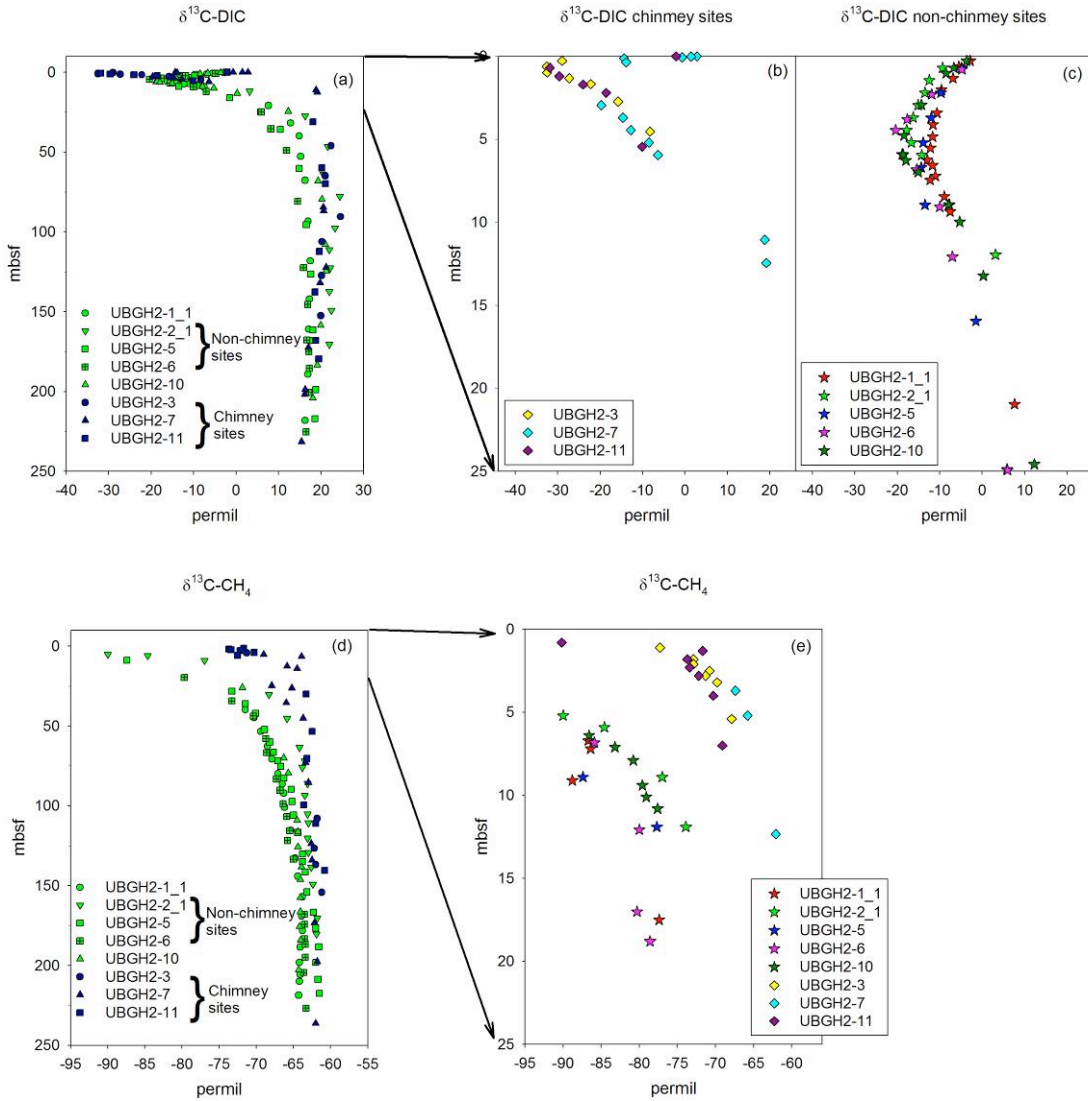


Figure 3: Carbon isotopic profiles of dissolved inorganic carbon (DIC) and methane. (a) DIC carbon isotopes from all eight sites investigated. Detailed DIC isotope profiles in the upper 25 meters are plotted in (b) and (c) for chimney and non-chimney sites, respectively. (d) Methane carbon isotopes in the void and headspace gas samples from all sites. (e) The methane carbon isotope for the first 25 m. These DIC and methane carbon isotopic profiles suggest that the fluid source ( $> 150$  mbsf) is not noticeably different in terms of the carbon isotopic signature at all sites. It is the reactions/processes around the SMTZ cause the observed variation.

Figure 4a

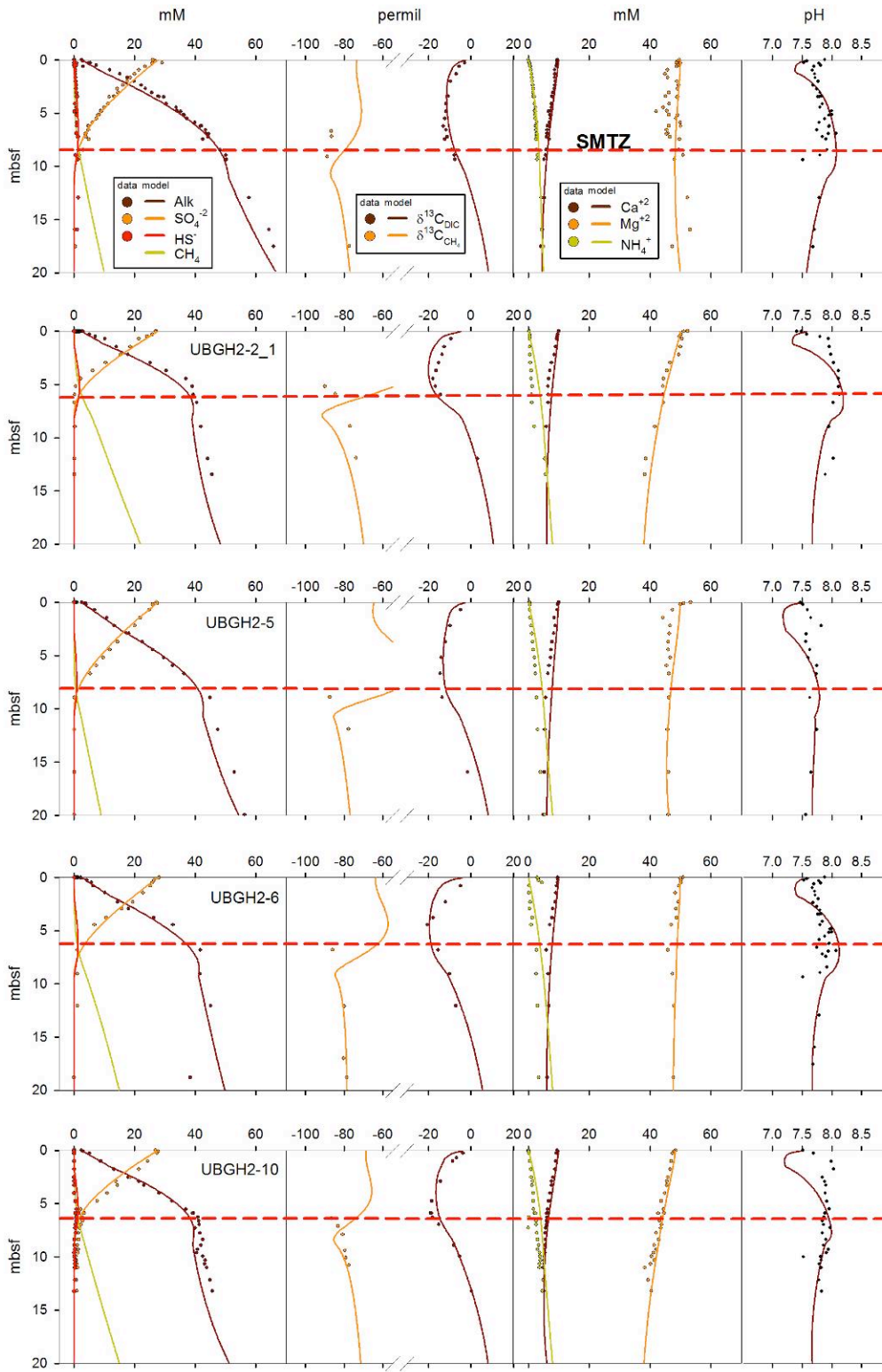


Figure 4b

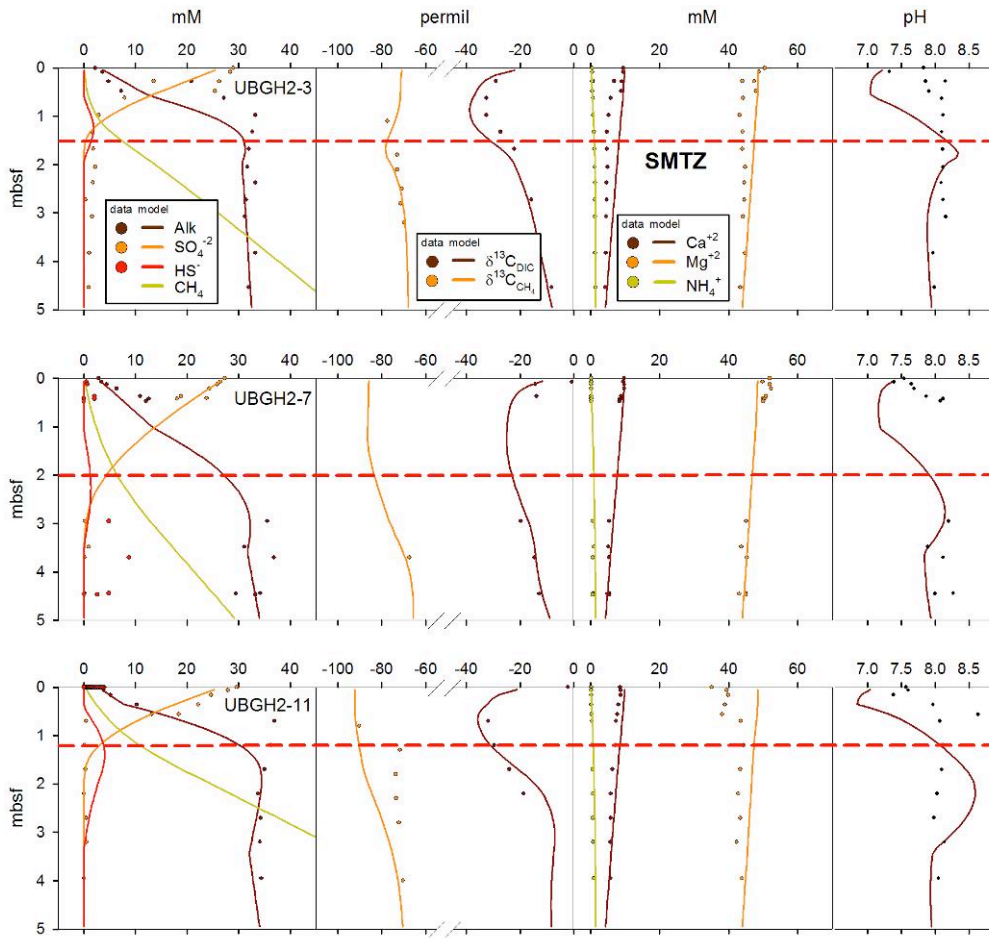


Figure 4: Model results for (a) the five non-chimney sites and (b) the three chimney sites, showing good fit to pore water composition and isotopic profiles.

Figure 5a

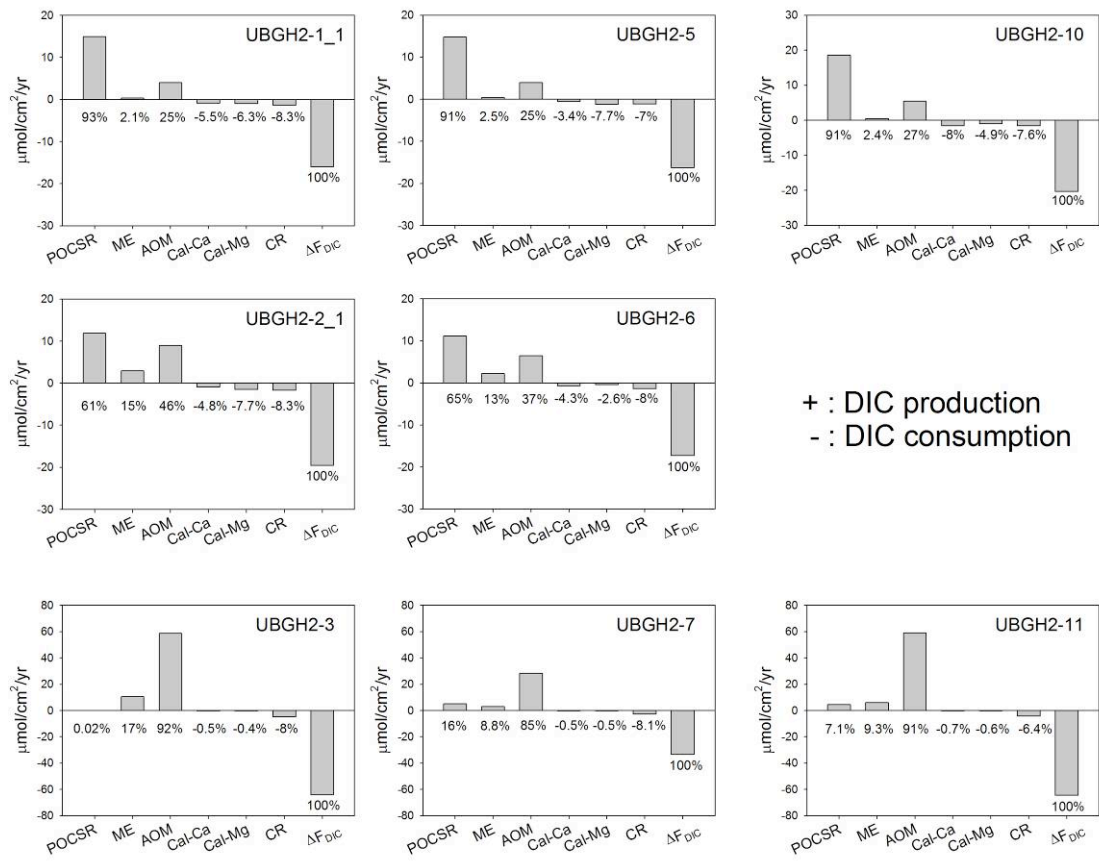


Figure 5b

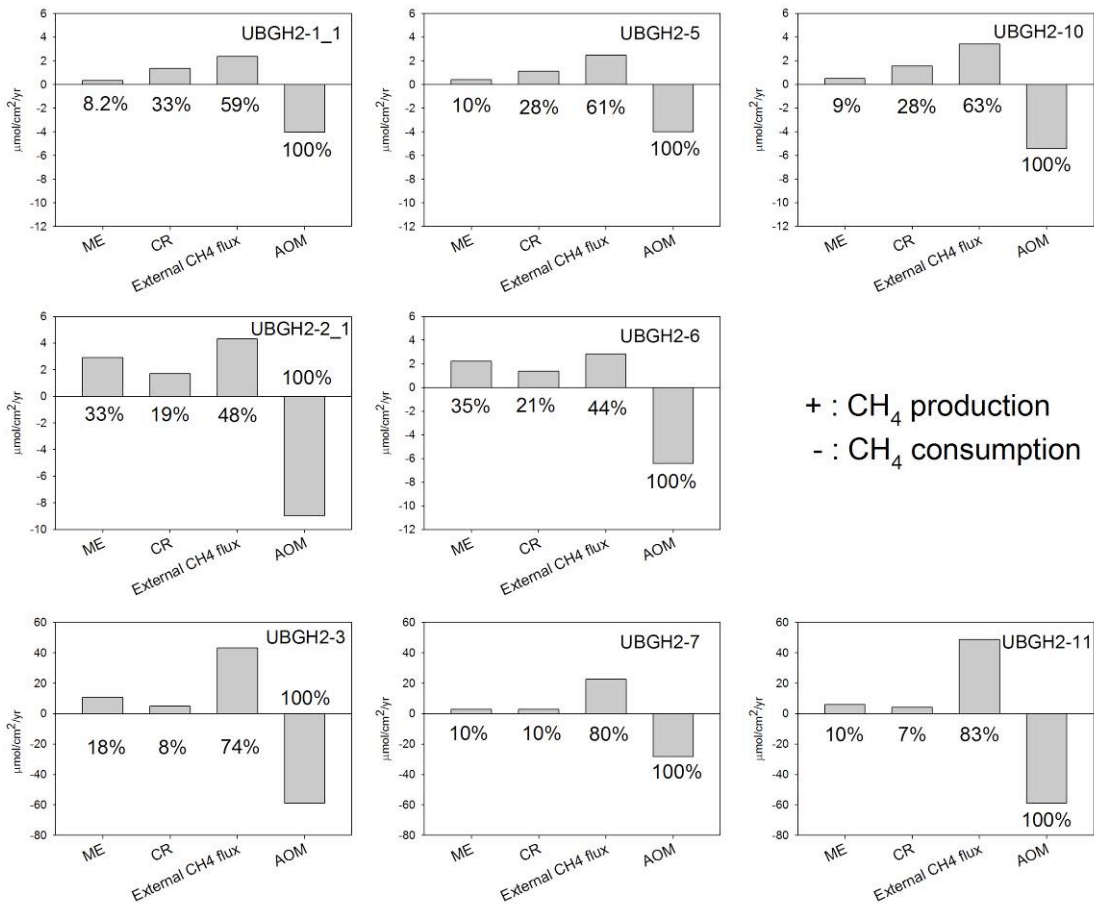


Figure 5c

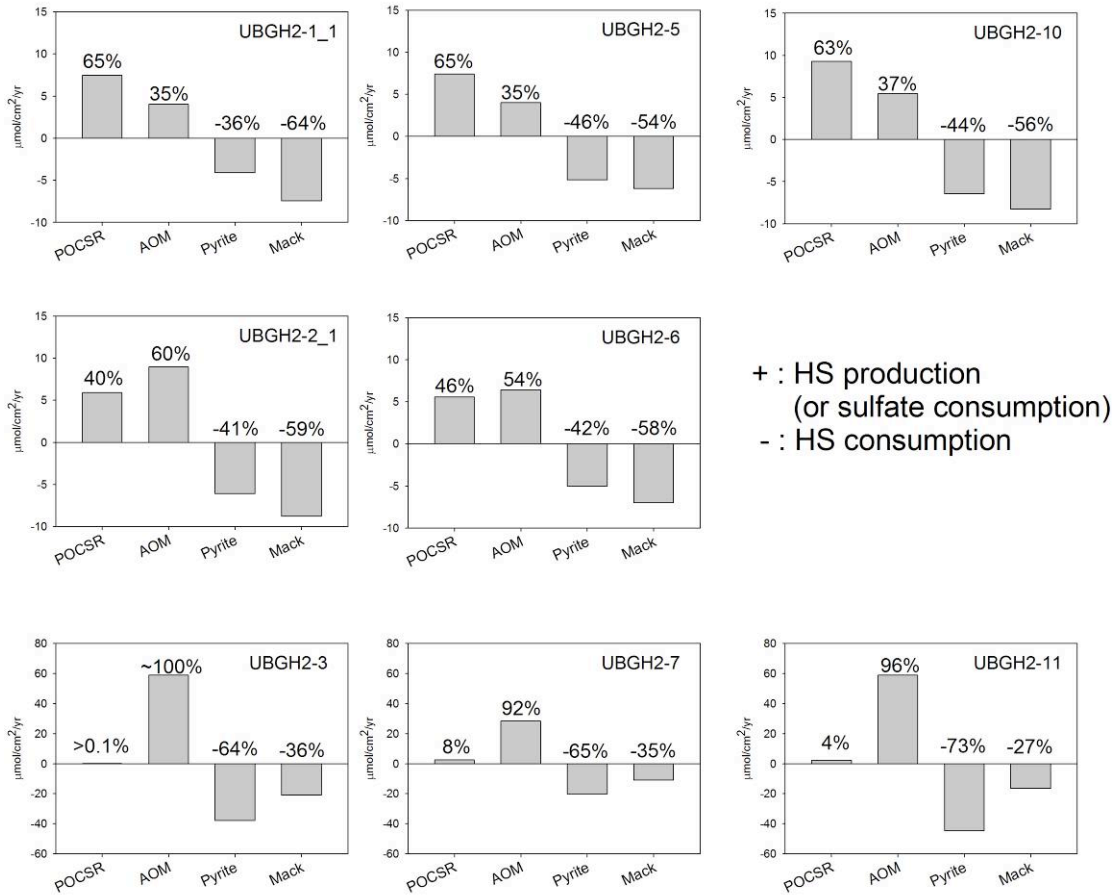


Figure 5: Depth-integrated rates estimated from our kinetic model at all sites. Note the different scales between the non-chimney (upper 5 panels) and chimney (lower 3 panels) sites. (a) Rates of the five DIC production/consumption reactions and their percentages relative to the  $\Delta F_{dic}$ , defined as the flux difference of input and output DIC (negative values represent net outflux). (b) Rates of the three methane sources and their percentages relative to AOM rate. (c) Rates of the four hydrogen sulfide production/consumption reactions and their percentage relative to total hydrogen sulfide production rate (or total sulfate reduction rate, total sulfate influx from seafloor). The very different carbon and sulfur cycles between the chimney and non-chimney sites are apparent from this comparison. See text for detail.

Figure 6

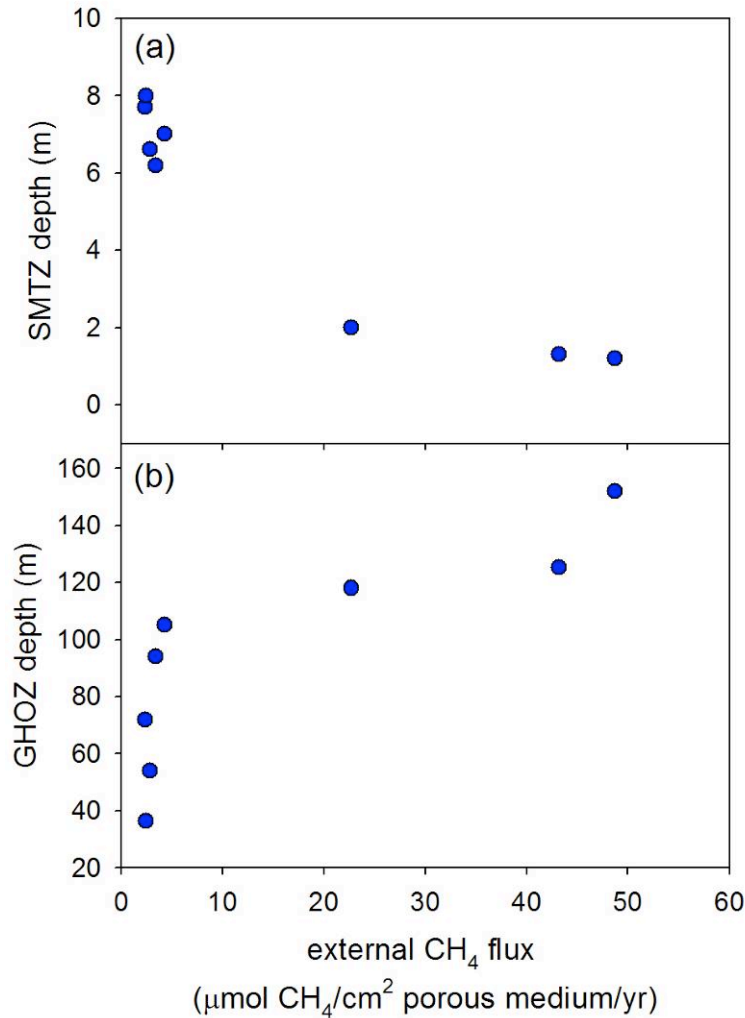


Figure 6: Correlations between external methane flux and (a) SMTZ depth and (b) thickness of gas hydrate occurrence zone (GHOZ). Thickness of GHOZ is calculated from the difference between depths of BSR and first gas hydrate occurrence listed in Table 2. SMTZ depth is negative proportional while GHOZ thickness is proportional to the external methane fluxes derived from the model. The non-linearity in both plots suggests that both SMTZ depth of GHOZ thickness are not solely dependant on external methane flux. Other factors or processes are may be of the same importance.

Figure 7

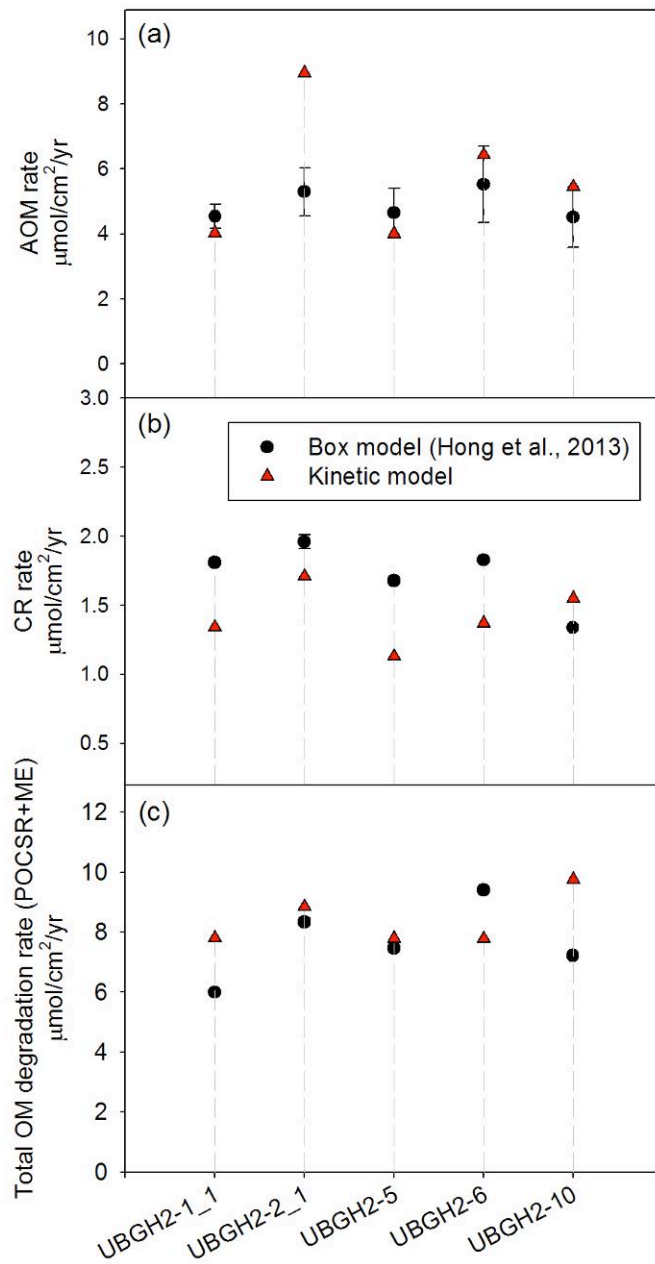


Figure 7: Comparisons of reaction rates estimated by the box model (Hong et al., 2013) and the current kinetic model. Error bars show the ranges of box model estimation (the range is smaller than the symbol size for CR and the total OM degradation rate). Both models provide similar estimations on three rates.

Figure 8

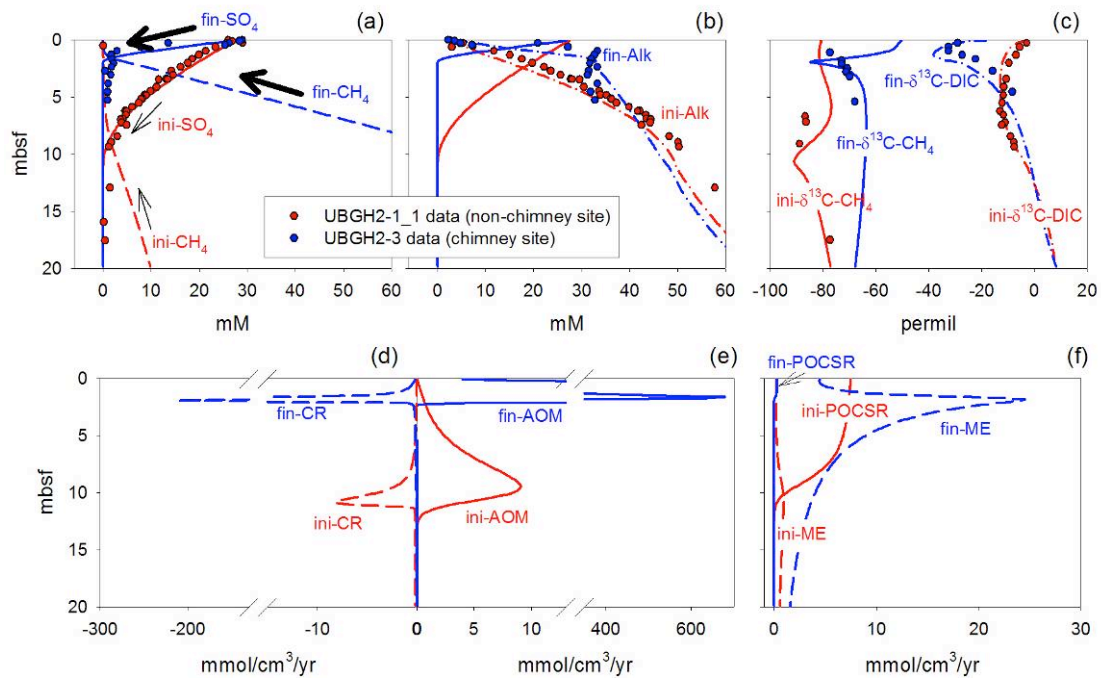


Figure 8: Evolution of a system from a low methane flux (non-chimney site UHGH2-1\_1) to one of high methane flux (chimney site UBGH2-3). In response to an increase in bottom methane supply, the AOM and CR rates increase by two orders of magnitude (note change in x axis scale), but the fraction of AOM fueled by CR drops from 30% in the initial low flux condition to 10% in the final high flux condition. POC is the primary organic matter degradation pathway in the initial low flux condition while more organic matter is degraded through ME in the final condition. Such shift in degradation pathway is related to the shoaling of SMTZ driven by an increase in bottom methane supply.

Figure 9

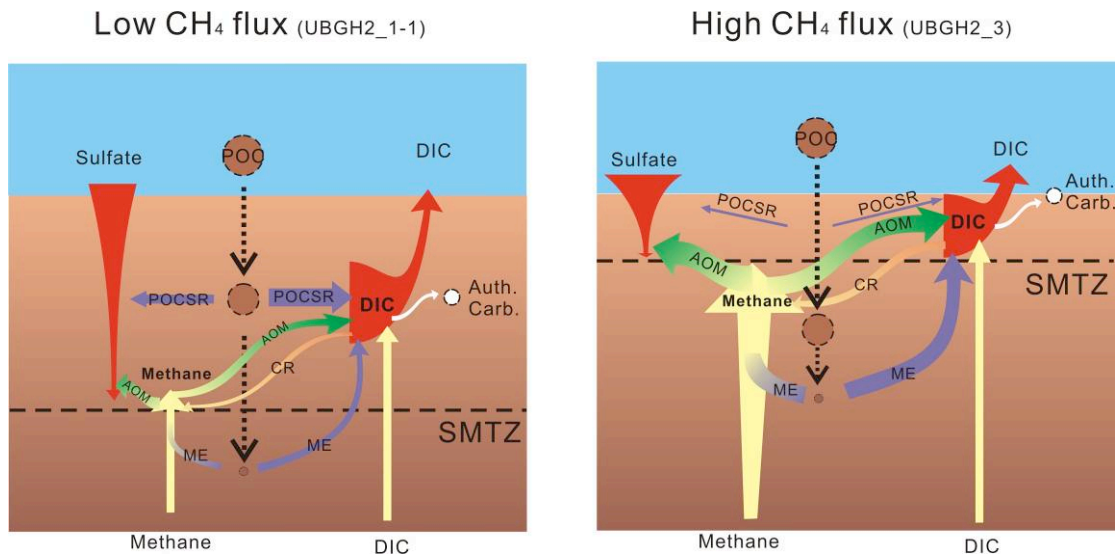


Figure 9: Cartoon illustrates the different modes of carbon cycling around SMTZ in the (a) non-chimney and (b) chimney environments in the Ulleung Basin. Size of the arrows represent the strength of fluxes or rates. See text for detail.

## **Appendix 2**

### **Quantifying paleo-methane flux in Cascadia margin with barite record in the sediments**

## **Quantifying paleo-methane flux in Cascadia margin with barite record in the sediments**

### **Abstract**

We successfully extended our Crunch Flow model to account for the precipitation/dissolution of authigenic barite. Records of authigenic barite distribution in the sediments can be used to infer the depth of SMTZ, which can be linked to the strength of methane flux in the past. The complexity behind this effort lies in the fact that barite could be both authigenic and detrital origin. Besides, increases in methane flux could result from external sources, such as gas hydrate dissociation, or intense methanogenesis from organic matter degradation when a layer of organic matter rich sediments is deposited. It is very difficult to decouple one factor from another from the records alone. In our current kinetic model, the detrital input of barite is accounted for by an assigning boundary barite condition, which can be time dependent. Moreover, the effect from organic matter degradation was teased out by matching the observed TOC profile. Methane produced through methanogenesis can shoal the SMTZ; however, as our model suggest, this amount of methane is not enough to account for the observed barite records and the need for an external methane source (i.e., methane inflow from outside the model regime) is established. Our model results revealed that a pulse of high methane flux occurred between 75.7 ka and 33 ka. As this period of time is sandwiched by two slope failure events and does not correlate to any specific change in paleo-oceanographic circulation, we conclude that such high methane flux is likely the result of sediment disturbance by slope failures.

## Model architecture

### *Chemical species and reaction network*

Most of the chemical species and reaction network considered in this work is from the model we developed for the carbon cycling in Ulleung Basin and are illustrated in Figure 1. The reaction networks includes anaerobic oxidation of methane (AOM), particulate organic matter sulfate reduction (POCSR), methanogenesis from organic matter (ME), authigenic carbonate precipitation (CP), and CO<sub>2</sub> reduction (CR). Besides, the dissolution and precipitation of authigenic barite, whose saturation is largely determined by the concentration of sulfate and barium in the pore water, are included. We treated the rate expressions of barite dissolution and precipitation differently follows the expressions proposed experimentally by Christy and Putnis (1993) and Bosbach (2002) with some modifications so that they can be formulated by CrunchFlow:

$$R_{\text{barite.diss}} = k_{\text{barite.diss}}(\Omega-1)$$

and

$$R_{\text{barite.prec}} = k_{\text{barite.prec}}(1-\Omega)^2$$

where  $k_{\text{barite.diss}}$  and  $k_{\text{barite.prec}}$  are the kinetic constants (mol/m<sup>2</sup>/sec) and  $\Omega$  describes the saturation of barite. Complete lists of the species and reactions considered are listed in Table 1 and 2, respectively.

### *Boundary and initial conditions*

We used the sea water value, except for the particulate barium in the sediments, as the upper boundary condition (UBC) and the measurements at 100 mbsf (meters below seafloor) as the lower boundary condition (LBC). We initiated the model with a pre-existing sulfate methane transition zone (SMTZ) which we use the current day condition as a reference. As we execute the model in ten separate steps to account for the different sedimentation rates (more details later), the initial condition (IC) for each step inherits from the output of the previous step.

### *Modeling strategy*

We considered different mechanisms that barite can appear in the sediments (detrital or authigenic) as well as the different reactions that affecting the solubility of barite (Figure 2), which is a function of both pore water barium and sulfate concentrations. Pore water sulfate is determined by the strength of POCSR and AOM. The former is fueled by organic matter degradation and the later relates to the flux of methane, which can be produced internally through methanogenesis or delivered from external sources outside the model frame. We have to quantify the effect on particulate barite from each of these mechanisms and processes to estimate on how much methane was delivered to our site from external sources. All these processes can be quantify by pore water pH, alkalinity methane, and sulfate, as well as barite and TOC in the sediments.

### *Age model and sedimentation rate*

We compiled age constrains from three different sources to construct our age model (Figure 3): radiocarbon dating (Johnson et al., 2010), oxygen isotope records from benthic foraminifera (Hong et al., 2013), and diatom biostratigraphy (Watanabe, 2006). Radiocarbon dating constrains the age up to ~45 ka (thousand years before present) or ~30 mbsf (meters below seafloor). We extended the record using oxygen isotope data to ~100 ka or ~50 mbsf. The last age constrain at ~96 mbsf comes from diatom biostratigraphy, which only tells us that the first hundred meters were younger than marine isotope stage (MIS) 5 (Watanabe, 2006). Due to the accuracy of each dating method, our age model is most reliable to 50 mbsf. For the deeper sections, where only diatom biostratigraphy is available, the results are less well constrained. We include the entire 120 kyr in the model; however, we focus primarily after 100 ka.

There are two issues associated with incorporating the age model into our kinetic model. First of all, because of the anomalously high sedimentation rate associated with SF events, these periods need special considerations. The sedimentation rate estimates for the SFs came from dating of such events at Site 1251 at Hydrate Ridge (Johnson et al., 2010) and on the northern Cascadian margin (Cosma et al., 2008; Chang et al., 2008). Sedimentation rate for the remaining calm periods was excluded from the effect of SFs.

For example, the section between 8.8 and 26 mbsf (Figure 2) was constrained by age picks of ~34.9 ka and 44.3 ka. The average sedimentation rate for the entire 17.2 meters of sediment is 1.8 m/ky (ky: thousand years). However, since the last 5 meters of this section (21-26 mbsf) was affected by slope failures, whose sedimentation rate is assumed to be 3.5 m/ky, the sedimentation rate for the pelagic sediment section from 8.8 to 21 mbsf has been calculated as:

$$\frac{21 - 8.8}{44.3 - 34.9 - \left(\frac{5}{3.5}\right)} = 1.53 \text{ (m/ky)}$$

The same strategy was applied to the entire sediment column. The age model and calculated sedimentation rates are shown in Figure 2.

The second issue with applying this age model is the sediment compaction during burial. The sedimentation rate calculated is based on the thickness of sediments after compaction which is different from the kind of rate, rate of deposition at time zero (Berner, 1980), required for the kinetic model. Therefore the sedimentation rate calculated above needs to be corrected for compaction based on the porosity. The way to do this is to correct the thickness of sediments between any age constraint by applying law of volume conservation (Berner, 1980):

$$(1 - \phi)h_x = (1 - \phi_0)h_0 \quad (3)$$

where  $\phi$  is the present porosity,  $h_x$  is the thickness of a layer at depth  $x$ ,  $\phi_0$  is the porosity at time zero which is assumed to be the core top porosity measurement, and  $h_0$  is the thickness of that layer at time zero which is what we need to calculate sedimentation rate at time zero.

*Incorporation of effect from slope failures in the model*

Effects of SFs are two-fold: higher sedimentation rate and dilution effect on particulate elements. High sedimentation rate will enhance sediment compaction and result in high advection flow and sediment burial rate. Dilution effect is most obvious from the distribution of particulate species. Our previous observations (Hong et al., 2013) suggested that both TOC and S contents are low during the periods of SF because of dilution by sediments brought by mass transport. The same effect is also apparent in particulate barium. In order to incorporate these two effects into model, we divided the total modeling time span (~120 ky) into 10 blocks (Table 3). Higher sedimentation rate (2.5 m/ky) and lower particulate barium content relative to values for calm periods were assigned to blocks affected by SFs (i.e. block 2, 4, 6, and 8 in Table 3). The depth range for each SF can be determined from magnetic susceptibility profile, and time span of each event is calculated by dividing depth by sedimentation rate. For the calm periods (block 1, 3, 5, 7, 9, and 10), the time span and depth range were determined in the same fashion. The time and depth spans of each of these 10 blocks and their assigned sedimentation rates and particulate barium upper boundary conditions (UBCs), are listed in Table 3.

The model was executed repeatedly 10 times to account for each of the time blocks. For each of the blocks, we applied different time lengths, sedimentation rates, and particulate barium UBCs which were assigned according to the values list in Table 3. The IC for the first run references the current day condition. The rest of ICs were derived from the outcome of each of the previous runs. For example, the first run was executed for 8.2 ky assuming a SMTZ at ~7 mbsf, constant particulate barium UBC and IC of 700 ppm, and a sedimentation rate of 1.96 m/ky. The outcome of this run shows that, due to the high sedimentation rate, the SMTZ was buried to 14 mbsf and there is a significantly elevated particulate barium content at 120 ka relative to the initial content. Such outcome was then applied as the IC for second run, which indicates a SF. This run was executed for 4 ky with a sedimentation rate of 2.5 m/ky and a LBC for particulate barium of 700 ppm. The outcome of this run shows that the depth of SMTZ was even deeper (~20 mbsf) due to a higher sedimentation rate relate to the previous run. This outcome was then applied as the IC of block 3.

## **Results**

We first test the hypothesis that our barite profile reflects the fluctuation of methane flux from external sources, such as gas hydrate dissociation. We match the pore water sulfate profile by allowing only one sulfate consumption reaction (i.e., the 2, 3, 4 pathway in Figure 2). This test suggests that methane from external sources is mandatory to form the observed barite profile and therefore confirms our hypothesis (Figure 4). We then adjusted all parameters to fit the model results without constraints (pore water pH, alkalinity, methane, sulfate profiles and barite, TOC profiles in the sediments) to reconstruct the history of methane flux. Our result suggests that a pulse of high methane flux is required between 75.7 ka and 33 ka. As this period of time was sandwiched by two slope failure events and does not correlate to any specific change in paleo-oceanographic circulation, we would conclude that such high methane flux may be the result of sediment disturbance by slope failures.

Table 1

<i>Primary Species</i>	<i>Secondary Species</i>	<i>Gases</i>	<i>Minerals</i>
$\text{H}^{12}\text{CO}_3^-$	$^{12}\text{CO}_{2(\text{aq})}$	$^{12}\text{CO}_{2(\text{g})}$	Calcite-Ca
$\text{H}^{13}\text{CO}_3^-$	$^{13}\text{CO}_{2(\text{aq})}$	$^{13}\text{CO}_{2(\text{g})}$	Calcite-Mg
$^{12}\text{CH}_{4(\text{aq})}$	$^{12}\text{CO}_3^{-2}$	$\text{H}_2\text{S}_{(\text{g})}$	$\text{CH}_2\text{O}$
$^{13}\text{CH}_{4(\text{aq})}$	$^{13}\text{CO}_3^{-2}$	$^{12}\text{CH}_{4(\text{g})}$	Pyrite
$\text{NH}_4^+$	$\text{NH}_{3(\text{aq})}$	$^{13}\text{CH}_{4(\text{g})}$	Mackinawite
$\text{HPO}_4^{-2}$	$\text{H}_3\text{PO}_{3(\text{aq})}$		Barite
$\text{HS}^-$	$\text{H}_2\text{PO}_4^-$		
$\text{SO}_4^{-2}$	$\text{PO}_4^{-3}$		
$\text{Fe}^{+2}$	$\text{H}_2\text{S}_{(\text{aq})}$		
$\text{H}^+$	$\text{S}^{-2}$		
$\text{H}_{2(\text{aq})}$			
$\text{Cl}^-$			
$\text{Ca}^{+2}$			
$\text{Mg}^{+2}$			
$\text{Na}^+$			
$\text{Ba}^{+2}$			

Table 2

*Homogeneous reactions**Abbreviation**in Fig. 1*

Acid-base	$\text{H}_2\text{O} + {}^{12/13}\text{CO}_2 \rightleftharpoons \text{H}^{12/13}\text{CO}_3^- + \text{H}^+$ $\text{H}^{12/13}\text{CO}_3^- \rightleftharpoons {}^{12/13}\text{CO}_3^{-2} + \text{H}^+$ $\text{NH}_4^+ \rightleftharpoons \text{NH}_{3(\text{aq})} + \text{H}^+$ $\text{H}_3\text{PO}_4 \rightleftharpoons \text{H}_2\text{PO}_4^-$ $\text{H}_2\text{PO}_4^- \rightleftharpoons \text{HPO}_4^{-2}$ $\text{HPO}_4^{-2} \rightleftharpoons \text{PO}_4^{-3}$ $\text{H}_2\text{S}_{(\text{aq})} \rightleftharpoons \text{HS}^- + \text{H}^+$ $\text{HS}^- \rightleftharpoons \text{S}^{-2} + \text{H}^+$ $\text{FeS}_{(\text{aq})} + \text{H}^+ \rightarrow \text{HS}^- + \text{Fe}^{+2}$	
Gas-dissolvent	${}^{12/13}\text{CH}_{4(\text{g})} \rightleftharpoons {}^{12/13}\text{CH}_{4(\text{aq})}$ ${}^{12/13}\text{CO}_{2(\text{g})} \rightleftharpoons {}^{12/13}\text{CO}_{2(\text{aq})}$ $\text{H}_2\text{S}_{(\text{g})} \rightleftharpoons \text{H}_2\text{S}_{(\text{aq})}$	
Aquatic redox	${}^{12/13}\text{CH}_{4(\text{aq})} + \text{SO}_4^{-2} \rightleftharpoons \text{H}^{12/13}\text{CO}_3^- + \text{HS}^- + \text{H}_2\text{O}$ $\text{H}^{12/13}\text{CO}_3^- + \text{H}^+ + 4\text{H}_{2(\text{aq})} \rightleftharpoons {}^{12/13}\text{CH}_{4(\text{aq})} + 3\text{H}_2\text{O}$	AOM CR
<i>Heterogeneous reactions</i>		
Calcite	$(\text{Ca}, \text{Mg})\text{CO}_{3(\text{s})} + \text{H}^+ \rightleftharpoons (\text{Mg}^{+2}, \text{Ca}^{+2}) + (1-a)\text{H}^{12}\text{CO}_3^- + a\text{H}^{13}\text{CO}_3^-$	CP
CH <sub>2</sub> O-SO <sub>4</sub>	$(\text{CH}_2\text{O})_{106}(\text{NH}_3)_{16}(\text{H}_3\text{PO}_4) + 53\text{SO}_4^{-2} + 14\text{H}^+ \rightleftharpoons 53\text{H}_2\text{S} + (106-b)\text{H}^{12}\text{CO}_3^- + b\text{H}^{13}\text{CO}_3^- + 16\text{NH}_4^+ + \text{HPO}_4^{-2}$	POCSR
CH <sub>2</sub> O-ME	$(\text{CH}_2\text{O})_{106}(\text{NH}_3)_{16}(\text{H}_3\text{PO}_4) + 14\text{H}_2\text{O} \rightleftharpoons (53-c)^{12}\text{CH}_4 + c^{13}\text{CH}_4 + (39-d)^{12}\text{CO}_2 + d^{13}\text{CO}_2 + (14-e)\text{H}^{12}\text{CO}_3^- + e\text{H}^{13}\text{CO}_3^- + 16\text{NH}_4^+ + \text{HPO}_4^{-2}$	ME
Pyrite (FeS <sub>2(s)</sub> )	Pyrite + H <sub>2(aq)</sub> $\rightleftharpoons$ Mackinawite + H <sub>2</sub> S <sub>(aq)</sub>	
Mackinawite (FeS <sub>(s)</sub> )	Mackinawite + H <sup>+</sup> $\rightarrow$ Fe <sup>+2</sup> + HS <sup>-</sup>	
Ammonium adsorption	$\text{NH}_4^+ + \text{MX} \rightleftharpoons \text{NH}_4\text{X} + \text{M}^+$	

Barite            Barite  $\rightleftharpoons$   $\text{Ba}^{+2} + \text{SO}_4^{-2}$   
dissolution  
and  
precipitation

Table 3

Blocks	Time span (ka)		Depth range (mbsf)		Sedimentation rate (m/ky)	Particulate Ba LBCs (ppm)	CH <sub>4</sub> LBC (mM)
1	128.2	120	96	80	1.96	700	1-10 <sup>2</sup>
2*	120	116	80	70	2.5	650	1-10 <sup>2</sup>
3	116	110.4	70	59	1.96	700	1-10 <sup>2</sup>
4*	110.4	108.8	59	55	2.5	600	1-10 <sup>2</sup>
5	108.8	91	55	46	0.5	650	1
6*	91	89.4	46	42	2.5	600	1-10 <sup>2</sup>
7	89.4	46.8	42	31	0.26	600	10 <sup>2</sup>
8*	46.8	42.8	31	21	2.5	600	1-10 <sup>4</sup>
9	42.8	35.4	21	8.75	1.65	600	1-10 <sup>4</sup>
10	35.4	13.7	8.75	0	0.4	600	10 <sup>4</sup>

Figure 1: The reaction network considered in this study. The various reactions (see Table 2 for the full list) affecting the cycles of carbon and sulfur are the center of the network.

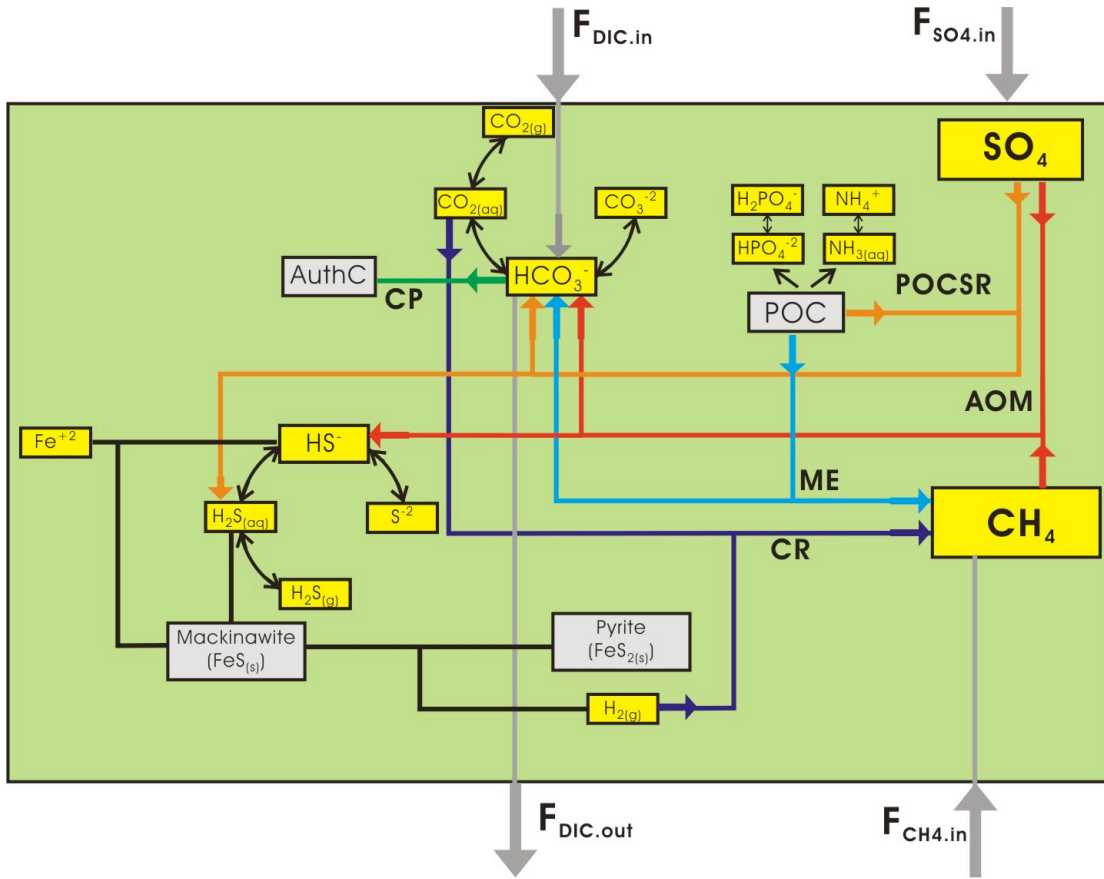


Figure 2: Different barite delivery mechanism (detrital and authigenic) and sulfate consumption pathways considered in this study.

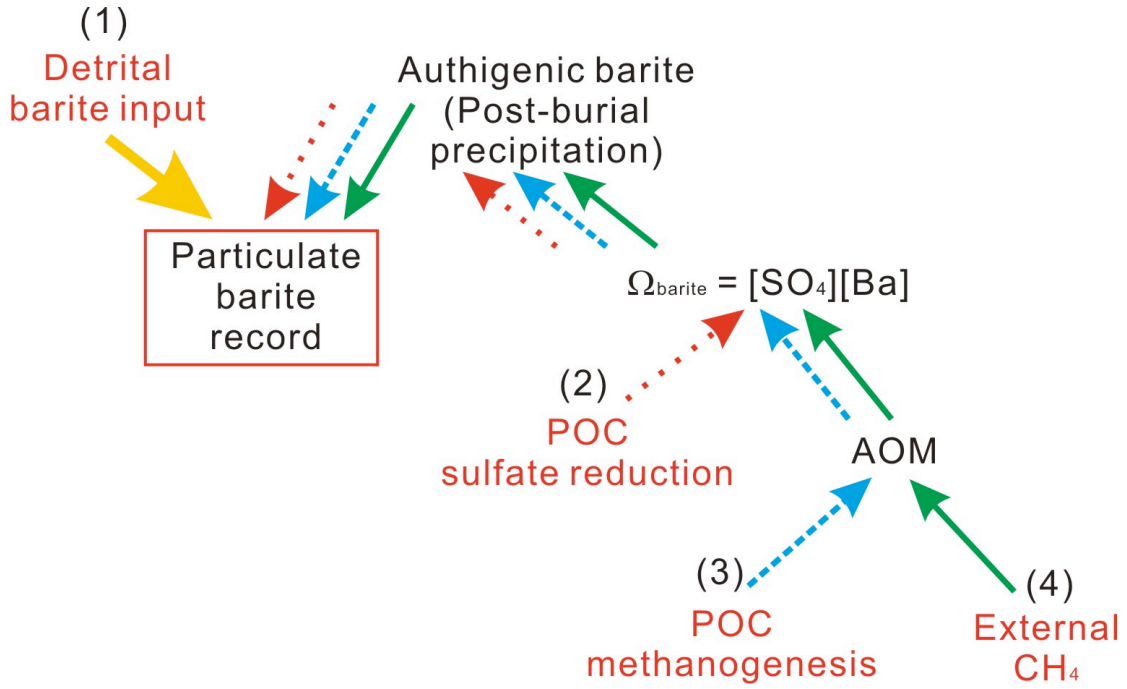


Figure 3: Age model used in the simulation.

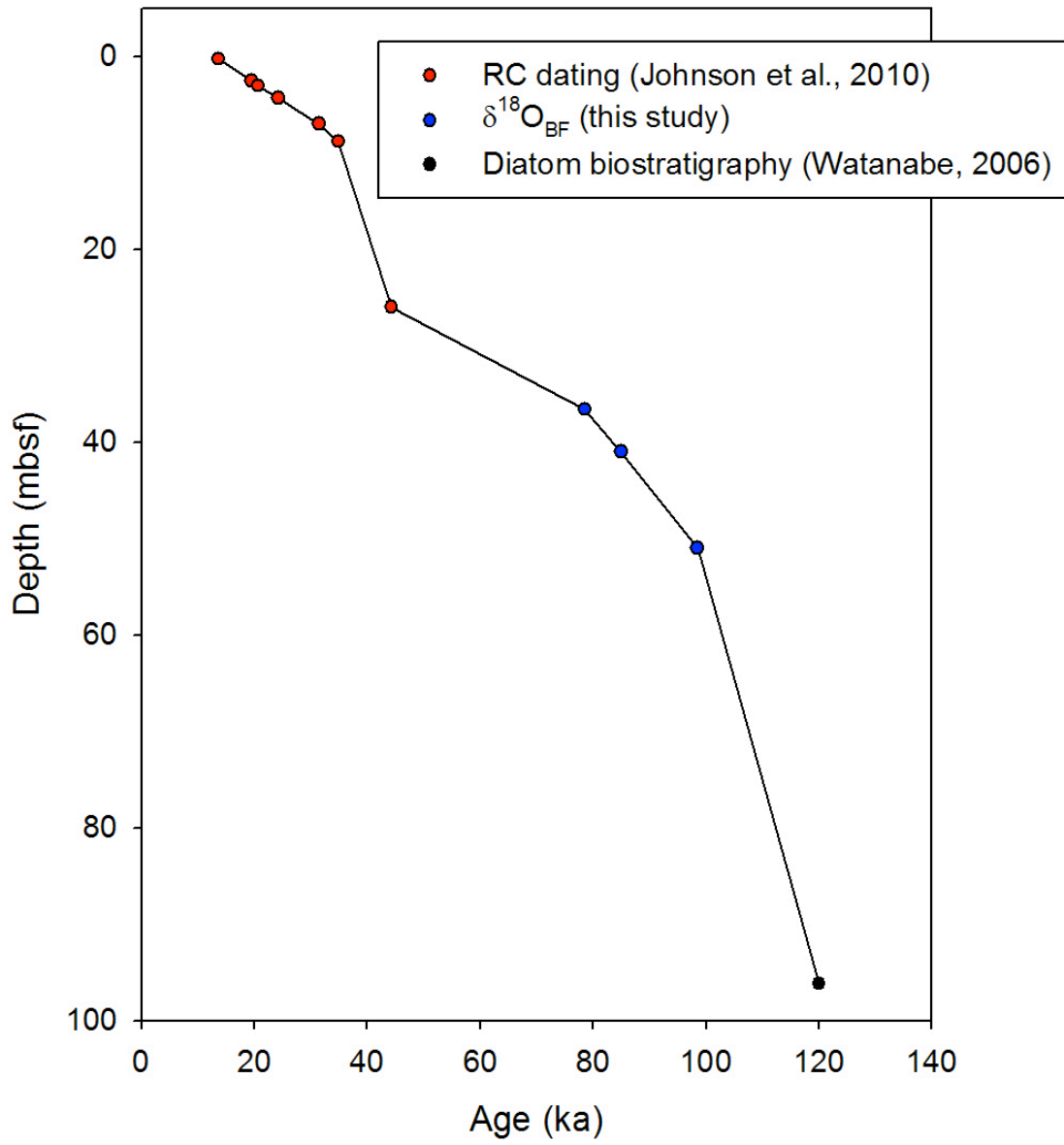


Figure 4: Model fit assuming sulfate is consumed by methane produced from internal methanogenesis (ME) alone (4a), by organic matter coupled sulfate reduction (POCSR) alone (4b), or by methane delivered from external sources (4c). This result confirms our hypothesis that external methane is required to result in the observed barite profile.

Figure 4a: ME

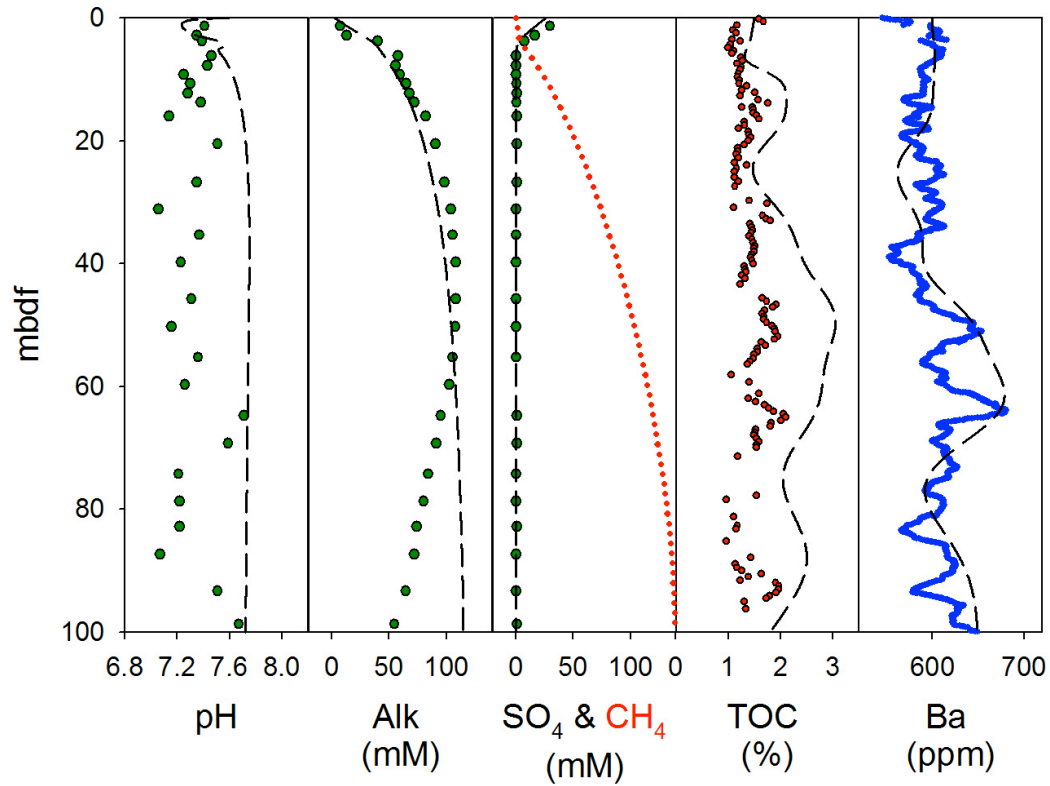


Figure 4b: POCSR

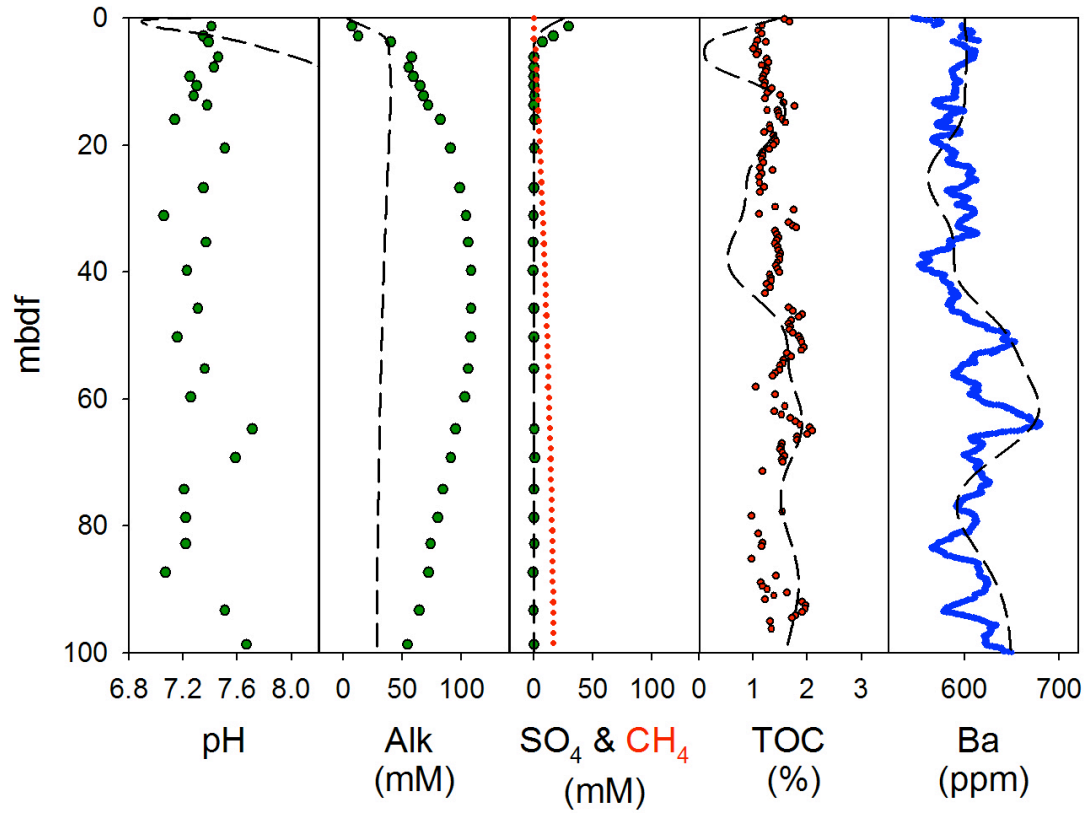
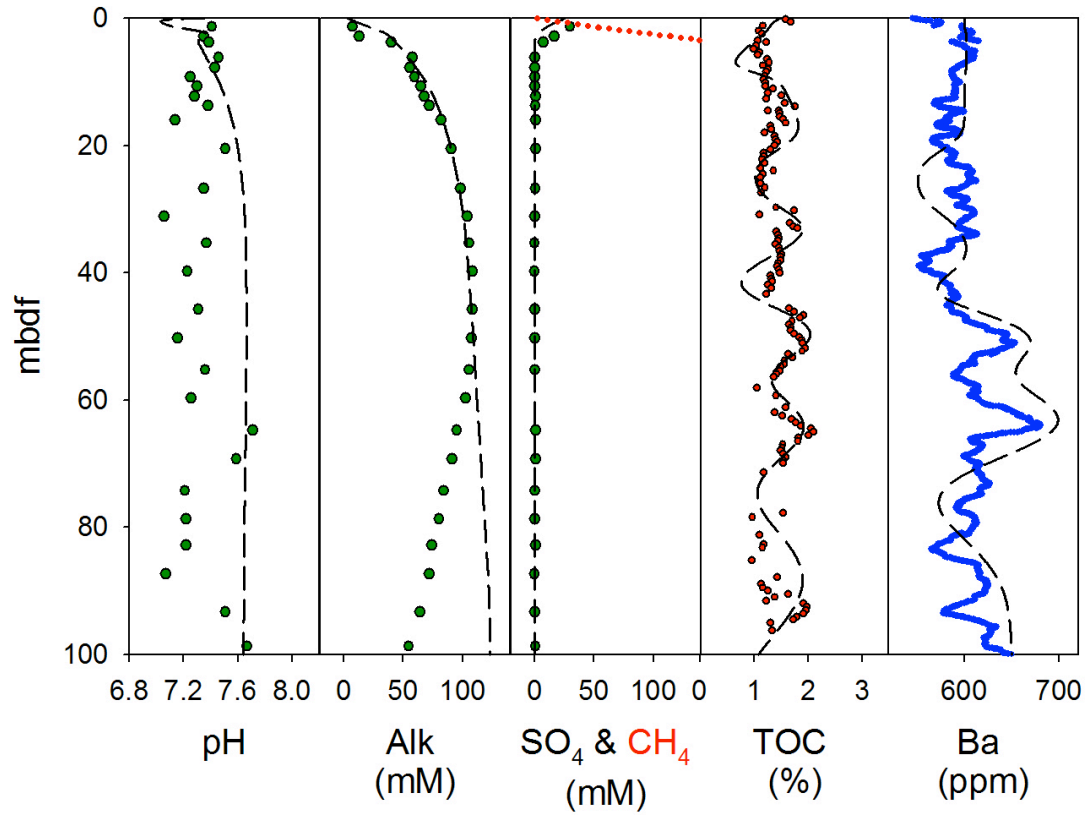


Figure 4c: external CH4



## **Appendix 3**

### **Dynamic of gas hydrate and transport of methane gas in Ulleung Basin**

## **Dynamic of gas hydrate and transport of methane gas in Ulleung Basin**

### **Abstract**

The primary goal of this project is to develop a model scheme that can simulate gas hydrate dissociation, dissolution, and formation in the shallow sediments of Ulleung Basin. This model can be constrained by pore water Cl profiles from this basin, where positive anomalies of Cl (up to 1400 mM) was observed from the depth as shallow as 25 mbsf. Cl is considered as an inert tracer since it is free from most of the biogeochemical reactions and reflects only transport processes and the amount of water in the sediments. We intended to develop the model scheme by using CrunchFlow, which was used throughout this project to simulate various biogeochemical reactions in the sediments. However we discovered that CrunchFlow alone is not capable of dealing with this topic as some of the important properties (e.g., temperature, permeability, porosity, and Darcy velocity) are not time-dependent. CrunchFlow is still attractive to attain our project goal because of its full capability in dealing with biogeochemical reactions and its very efficient built-in mathematical engine to solve the partial differential equations. We therefore developed a hybrid model scheme by coupling a home-made MATLAB code with CrunchFlow. The MATLAB code is used to calculate all reactions and the corresponding changes in sediment and fluid properties, whereas CrunchFlow will be used to redistribute chemical species based on their transport behaviors. Such scheme will provide us the flexibility we need for our task while we can still take advantage of the computational capability and geochemistry database in CrunchFlow. A preliminary version of this model has been built to simulate the chloride profile at UBGH2-3. To fit the profile, transport of free gas methane is essential which agrees with previous observations.

### **Project goal overview**

The primary goal of this project is to develop a model scheme that can simulate gas hydrate dissociation, dissolution, and formation in the shallow sediments of Ulleung Basin. This model will be constrained by pore water Cl profiles from this basin, where positive anomalies of Cl (up to 1400 mM) was observed from the depth as shallow as 25

mbsf. Cl is considered as an inert tracer since it is free from most of the biogeochemical reactions and reflects only transport processes and the amount of water in the sediments. We intent to develop the model scheme by using CrunchFlow, which was used throughout this project to simulate various biogeochemical reactions in the sediments. We however discovered that CrunchFlow may be incapable of dealing with such topic as some of the important properties (e.g., temperature, permeability, porosity, and Darcy velocity) are not time-dependent. CruchFlow is still attractive to our project goal due to its full capability in dealing with biogeochemical reactions and very efficient built-in mathematical engine to solve the partial differential equations. We therefore developed a hybrid model scheme by coupling a home-made MATLAB code with CrunchFlow. The MATLAB code will be used to calculate all reactions and the corresponding changes in sediment and fluid properties whereas CrunchFlow will be used to redistribute chemical species based on their transport behaviors. Such scheme will provide us the flexibility we need for our task while we can still take advantage of the computational capability and geochemistry database in CrunchFlow.

### **The hybrid model scheme**

The entire model scheme consists of two parts: the set-up for initial environment and the looping between MATLAB and CrunchFlow. The sequence of this hybrid model scheme is illustrated in Figure 1 and detailed in the following paragraphs.

#### *Initial setup of the sediment and fluid properties (Figure 1a)*

The MATLAB code reads the initial condition assigned to CrunchFlow and uses it to calculate the initial value for the properties such as liquid saturation, porosity, formation temperature, Darcy velocities for fluid and gas, and permeability. As CurnchFlow calculates only the partial pressure of gases, we need to assume an initial volume of gas ( $10^{-5}$  m<sup>3</sup>/m<sup>3</sup>). The volume of gas, together with the porosity, is used to calculate the fraction of each phase (water, gas, hydrate, and sediments). The liquid saturation can then be calculated from the fraction of gas and water. Permeability is calculated based on liquid saturation and the fractions of sediment grain and hydrate. Pressure of water phase, which is needed to calculate the density of gas, can be derived from the ambient pressure

(hydrostatic pressure), liquid saturation, and density of pore water (assumed to be seawater initially). The Darcy velocities for water and gas can be computed from many of the aforementioned information. Liquid saturation, porosity, formation temperature, Darcy velocities for fluid and gas, and permeability are then feed to CrunchFlow for next step.

#### *Setup of the CrunchFlow environment (Figure 1b)*

With the information calculated from the previous step, a CrunchFlow simulation is initiated by considering dissolved chloride, sodium, and methane in the pore water as well as gaseous methane and gas hydrate. The CrunchFlow code reads in information of sedimentation rate, liquid saturation, porosity, formation temperature, Darcy velocities for fluid and gas, and permeability and redistribute chemical species based on laws of diffusion and advection of fluid and gas. We now assumed constant formation factor, but this could potentially be time-dependent if a proper link with the abundance of hydrate is mathematically described. CrunchFlow then outputs the resulting concentration profiles of all species from different phases (i.e., water, gas, and solid).

#### *Reassessment of the sediment and fluid properties (Figure 1c)*

The new distribution of chemical species among different phases is used by the MATLAB code to update the fraction of the four phases. Reaction rates of hydrate formation, hydrate dissociation, hydrate dissolution, and gas dissolution are calculated based on the updated phase fractions. As hydrate and methane gas appear (or disappear), the densities, pressures, and the Darcy velocities of gas and water will change accordingly, as well as the formation temperature. Many of these properties are mutually dependent. For example, pressure of water is a function of water density, chloride content, and formation temperature. The density of water depends on the density of gas which is a function of water pressure. To solve these mutually depended parameters, a Newton-Raphson iterative scheme is implemented.

### **Preliminary model results**

A preliminary version of the model has been built which allows reactions and transport can be calculated separately. This version, however, the update of sediment and fluid properties (e.g., Darcy flow, permeability, temperature, density) in the modeling loop has not yet been included due to some numerical issues. We simulated the pore water chloride profile at site UBGH2-3 with this preliminary model (Figure 2). In order to fit the chloride profile, transport of gas form of methane is essential. This conclusion agrees with the conclusion by Torres et al. (2004) in Hydrate Ridge.

Figure 1: The hybrid model scheme

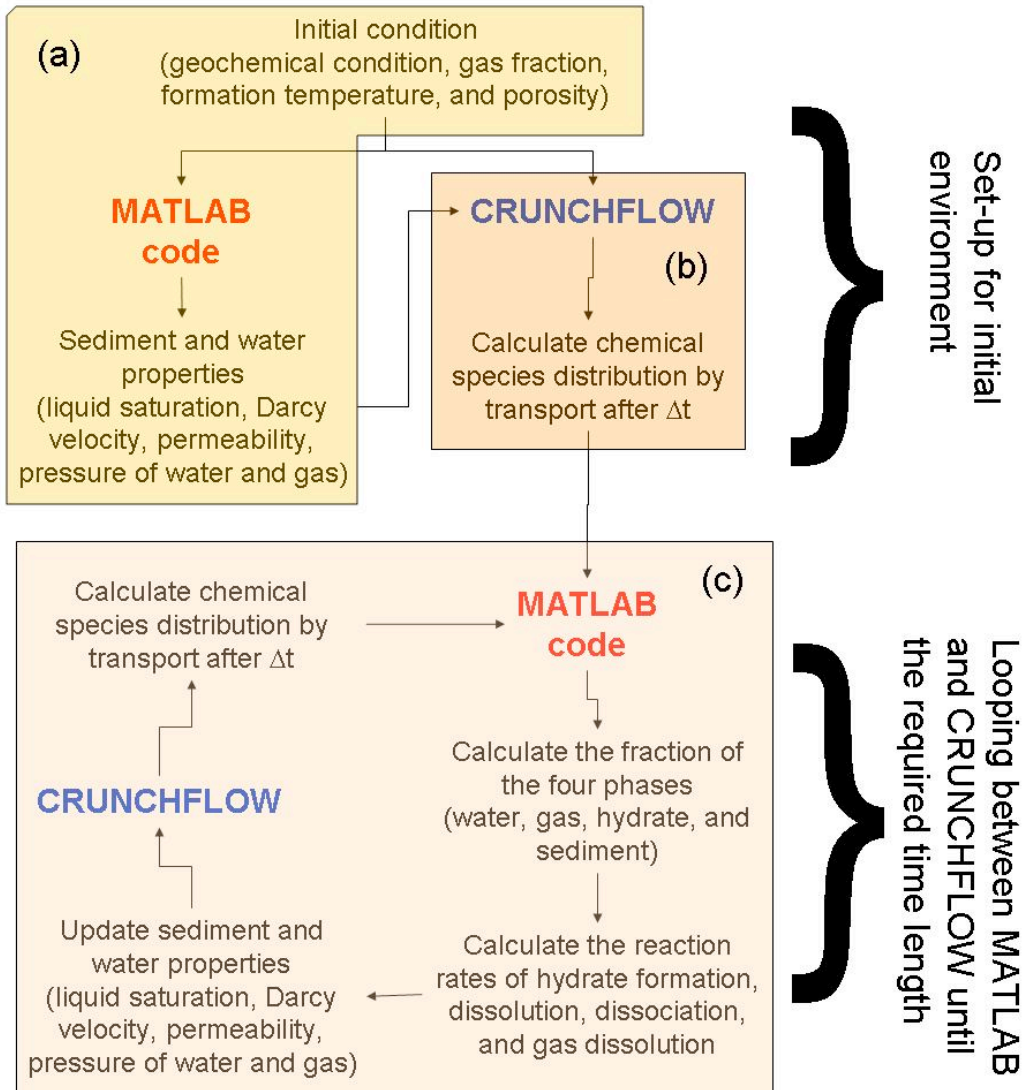
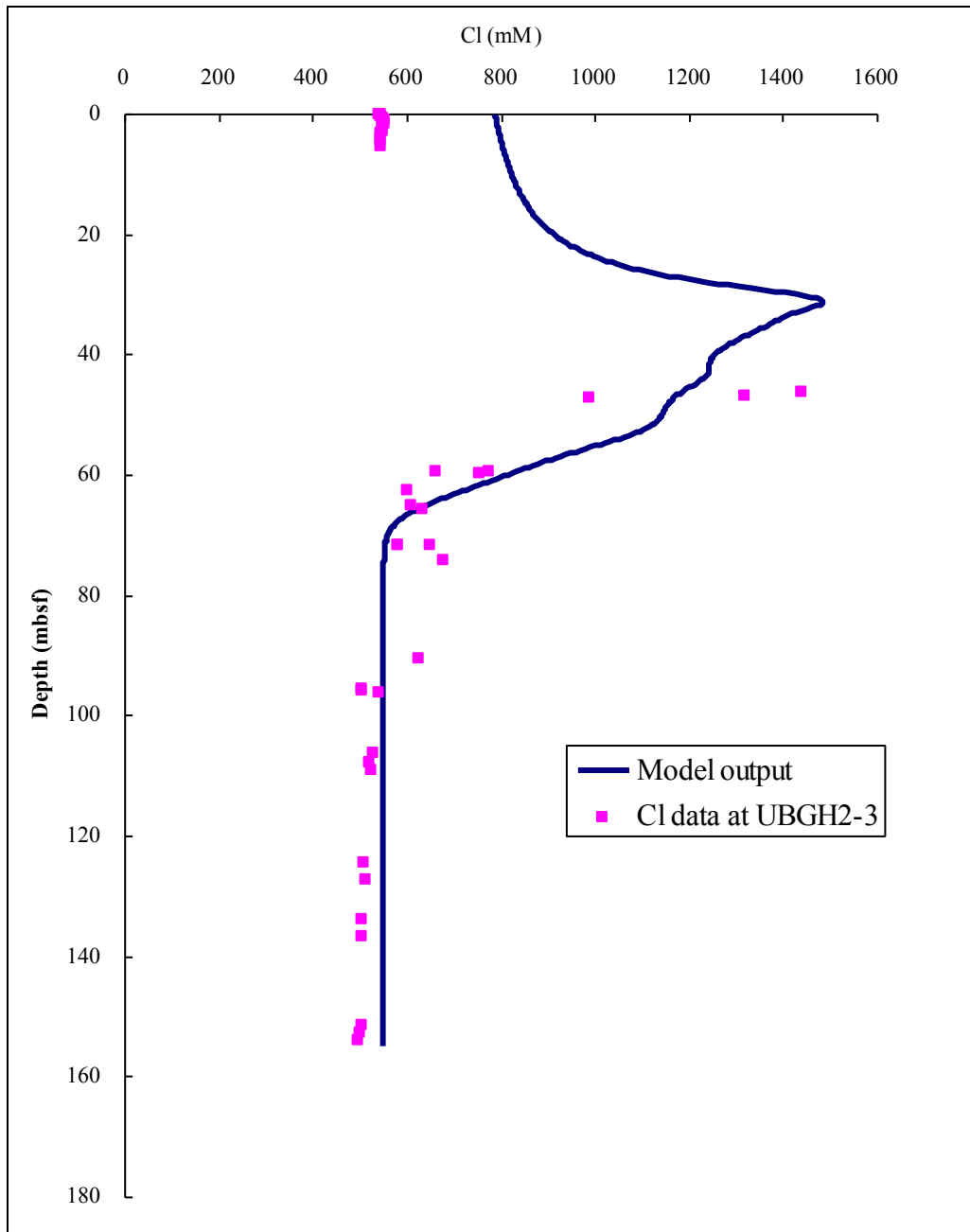


Figure 2: Model fitting with chloride data from UBGH2-3



## **Appendix 4**

**A kinetic-model approach to quantify the effect of mass transport deposits on pore water profiles in the Krishna-Godavari Basin, Bay of Bengal**

A kinetic-model approach to quantify the effect of mass transport deposits on pore water profiles in the Krishna-Godavari Basin, Bay of Bengal

Wei-Li Hong<sup>1</sup>, Evan Solomon<sup>2</sup>, Marta Torres<sup>1</sup>

<sup>1</sup>College of Earth, Ocean, and Atmospheric Sciences, Oregon State University, 104 CEOAS administration bldg, Corvallis, OR 97331, USA.

<sup>2</sup>School of Oceanography, University of Washington, Seattle, WA 98195

### **Abstract**

Mass transfer deposits (MTDs) in the Krishna-Godavari Basin on the eastern Indian margin are common sedimentary features over the modern continental slope. Quantitative understanding of the scale and age of these MTDs is especially relevant to understanding their triggering mechanisms and environmental feedbacks, as well as for interpreting pore water chemical profiles. Pore water profiles in sediments recovered during the 2006 Indian National Gas Hydrate Project (NGHP-01) expedition suggest that MTDs are present at seven of the sites cored in the Krishna-Godavari Basin. Kinetic modeling of the S-shaped pore water sulfate and ammonium profiles from these sites provides quantitative estimates of the thickness of individual MTDs, time elapsed after the MTD event, rate of sulfate reduction in the MTD, and time required to reach a new steady state. The model results suggest that the MTDs at the seven study sites are 8 to 25 meters thick and are 300 to 1600 years old. Within the MTD sections, sulfate reduction rates are 126 to 1215 mmol/m<sup>2</sup>/yr and the time needed to reach a new steady state ranges from 2000 to 3800 years. In comparison to depth-integrated sulfate reduction rates estimated in other regions, our estimates are relatively high reflecting a much thicker sulfate reduction zone that results from the MTDs. A positive correlation is observed between water depth and the sedimentation rate in the MTD sections (i.e., thickness of MTD divided by its age), which agrees with previous studies of MTDs in this region. We caution against using the pore water data from sites experiencing significant MTDs to infer metabolic processes

and to quantify steady-state reaction rates as our model results confirm the remarkable influence of transient MTDs on pore water profiles.

## **Introduction**

The Krishna-Godavari (K-G) Basin on the eastern Indian margin is characterized by extensive mass-transport deposits (MTDs) formed by sliding/slumping of river-delivered sediments (Forsberg et al., 2007; Ramana et al., 2009; Shanmugam et al., 2009; Ramprasad et al., 2011). MTDs in the K-G Basin may be related to variations in regional climate and changes in sediment discharge from the Krishna and Godavari rivers (Forsberg et al., 2007; Ramana et al., 2009; Ramprasad et al., 2011). However, the regional variability, magnitude, and age of the individual events are poorly constrained. Furthermore, sediments deposited by these abrupt events likely alter the pore water geochemical records in the shallow sediments, and hinder development of quantitative models for early diagenetic processes in this margin.

Pore water composition is very sensitive to localized and recent slumping events, as previously shown by Hensen et al. (2003) and Holsein and Wirtz (2010). The pore water profiles sampled during the recent Indian National Gas Hydrate Project (NGHP-01) expedition (Figure 1) provide a unique opportunity to quantify the timing and magnitude of these deposits. In this study, we apply a transport-reaction model to pore water data from seven sites drilled in the K-G basin (Table 1) to quantify the thickness of the deposits and the time elapsed after each event. This information is potentially important for future studies focusing on the control and/or feedback mechanisms of these episodic sediment transport events. Our work also highlights the importance of these events on the shape of pore water solute profiles and on their interpretation.

## **Study region**

The modern K-G Basin in the eastern passive margin basin of India receives large sediment inputs from the Krishna and Godavari Rivers. The delta fronts exhibit MDTs, scars and irregular topography over the modern upper continental slope formed by sliding/slumping (Forsberg et al., 2007; Ramana et al., 2009; Ramprasad et al., 2011). Sediments transported through large canyons also contribute to the total sediment accumulations (Kotha, 2002; Bastia, 2004; Murthy, 1999). Recent seismic and bathymetric surveys in this area imaged widespread MTDs (Solheim et al., 2007;

Forsberg et al., 2007; Shanmugam et al., 2009; Ramprasad et al., 2011), and were used to guide drilling during the NGHP-01 expedition in 2006.

Sediment thickness in the K-G basin varies from 3 to 5 km and may exceed 8 km in the offshore region (Prabhakar and Zutshi, 1993). Drilling during NGHP-01 sampled the upper 200-300 meters at 15 sites, aimed at characterizing the gas hydrate potential of this region (Figure 1). Here we focus only on the first 40-60 meters of the sediment column (Table 2), in an effort to unravel the relative magnitude and frequency of slumping events, as their effect on pore water profiles impact ongoing efforts to quantify organic carbon cycling and methane dynamics in this passive margin. The sediments studied all correspond to the same Quaternary lithostratigraphic unit primarily composed of clay with variable amounts of carbonates (4-60%), and trace amounts of quartz, feldspar, mica, and iron sulfide (Collett et al., 2008). Frequent silt/sand beds are observed at each site (Collett et al., 2008). The distribution of authigenic carbonate is not necessarily correlated with the current sulfate-methane-transition-zone (SMTZ), defined by the pore water sulfate and methane profiles, suggesting migration of the SMTZ in the past (Collett et al., 2008) or simply burial of authigenic carbonates produced at the SMTZ through time, perhaps punctuated by sediment slumping.

### **Effect of MTDs on the pore water data**

Shipboard pore water analyses, including sulfate concentration, were reported in Collett et al. (2008). Shorebased pore water ammonium analyses were reported in Solomon et al. (this issue). Pore water profiles in seven of the 15 sites drilled in the K-G Basin suggest a non-steady-state condition (Figure 2). The concentration of all pore water species, especially sulfate, at these seven sites changes rapidly in a relatively short depth interval, indicating the importance of non-diffusional processes. A rapid drop in sulfate content and the concordant increases of both ammonium and dissolved inorganic carbon (DIC) concentrations at the first ~5 meters in the sediments (Collett et al., 2008) are indicative of sulfate consumption due to organic matter degradation (abbreviated as POCSR, particulate organic carbon sulfate reduction, hereafter). As no methane present in this interval, POCSR should be the only reaction consuming sulfate. Between 15 to 25 meters

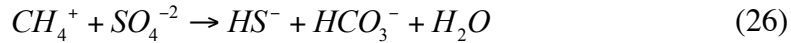
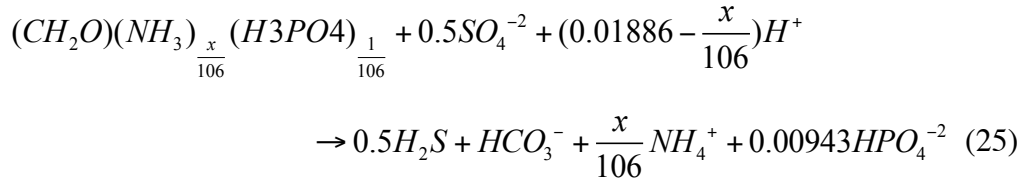
below seafloor (mbsf), sulfate content remains constant until it is again consumed by methane through anaerobic oxidation of methane (AOM) at greater depths (Figure 2). We hypothesize that these sulfate profiles reflect recent mass transfer events at each site, and that the slumping is too recent for diffusion to smooth the dissolved sulfate distribution between the two sulfate reduction zones.

Before slumping, sulfate supplied by diffusion from overlying seawater is consumed by both POCSR and AOM, which forms a distinct SMTZ (Figure 2A). In environments devoid of slumping these processes act together to generate a smooth decrease in dissolved sulfate with depth (e.g., Claypool and Kaplan, 1974; Froelich et al., 1979; Borowski et al., 1999; Hong et al., 2013; Figure 2A). If then a layer of sediment with fresh labile organic matter is rapidly deposited by a MTD (Figure 2B), the SMTZ is buried deeper while the reactive organic matter in the newly deposited sediments also consumes sulfate, leading to the shallow-most drop in sulfate content and effectively separating both sulfate consuming processes (Figure 2C). This produces the S-shaped profiles observed and clearly indicates that the system is out of steady state. Eventually, the persistent bottom methane supply will move the SMTZ upward until a new steady state is reached (Figure 2D). We use a kinetic modeling approach to explore the conditions leading to the S-shape of sulfate profiles from these seven sites to unravel the effects of MTDs on pore water geochemistry (Figure 2C).

## **Model architecture**

### *Reactions and model logistics*

In these simulations we use the FORTRAN routine CrunchFlow, as described in Steefel (2009). Hong et al. (2013; 2014) has listed the various reactions involved around the SMTZ, among which we focus only on POCSR and AOM. Above SMTZ, where there is no methane present, POCSR is responsible for all of the sulfate consumption; whereas, AOM becomes more significant closer to the SMTZ. These two reactions can be summarized as:



where x is the stoichiometry of nitrogen in the organic matter and was calculated from the C/N ratio at each site (Table 3; data from Phillips and Johnson, this volume). We are aware that such calculation maybe an oversimplification, as the amount of ammonium released from organic matter degradation depends on the C/N ratio in the pool of reactive carbon instead of the bulk organic matter. However, the good agreement with the  $NH_4$  data, as we will show later, indicates that this is still a reasonable approximation.

In order to constrain the rate of organic matter degradation in the first sulfate reduction zone (Figure 2C), we simulate pore water ammonium, which can be described as a function of both organic matter degradation and ion exchange on mineral surfaces (Von Breyman et al., 1988a, 1988b, 1990; Wallmann et al., 2006; 2008). To formulate ion exchange with CrunchFlow, we chose the *Gaines-Thomas* activity convention and specify a cation exchange capacity for the bulk sediment. Solid density is calculated based on the sum of mineral volume fractions. In the K-G Basin, ~80-90% of the sediment is composed of clay minerals (Collett et al., 2008), ~50-80% of which is smectite (Venkatarathnam and Biscaye, 1973; Pattan et al., 2008; Underwood, pers. comm.). Using a CEC for smectite of 80-150 meq/100 g of sediment (Hang and Brindley, 1970; Jaynes and Bigham, 1986), we estimated the CEC of K-G Basin sediments to range from 32 to 80 meq/100 g of sediment. The values used at each site were further constrained by data fitting using pore water measurements, and are specified for each site in Table 2.

POCSR was formulated as Monod-type reaction with one Monod term (half saturation constant of 100  $\mu$ M for sulfate was adopted; Wegener and Boetius, 2009). AOM was

formulated as a double-Monod-type kinetic reaction with (half-saturation constants of 500  $\mu\text{M}$  were used, Wegener and Boetius, 2009). Detailed formulation for the reactions is given in Hong et al. (2014). The *Dirichlet*-type boundary conditions were used for all species, including methane. A fixed concentration of methane was assigned at the bottom of the simulation frame at each site ( $L$  in Figure 2 and Table 2). This concentration is constrained by the observed methane and sulfate profiles as this bottom supply of methane induces AOM at a rate, together with POCSR, that lead to the observed methane and sulfate profiles. It is important to notice that the observed methane concentration can only partly constrain the model as the onboard measurement of gas concentration always suffers from the gas lost issue when the in-situ pressure is higher than atmospheric level.

In order to constrain the thickness of each MTD ( $\Delta x$  in Figure 2B) and the time elapsed since deposition ( $\Delta t_1$  in Figure 2C), we evolved the model simulation in two steps. In the first step (Figure 2A), we used bottom seawater composition as the initial condition. Giosan (pers. comm. 2009) have reported variations in sedimentation rates among the different sites ranging from 0.15 m/kyr at Site 10 to 0.85 m/kyr at Site 5. Therefore, we used a range of sedimentation rates to test its influence on the model results. We observed no significant effect when varying sedimentation rates from 0.15 to 0.85 m/kyr, which is not surprising since the time scale considered in this study is only on the order of several thousand years. We used then an average sediment deposition rate at all sites of 0.15 meter per thousand years, based on estimates listed in Collett et al., (2008) and Mazmudar et al. (2009).

The kinetic constant for organic matter degradation ( $k_{\text{OM}}$ ) is constrained by simulating the ammonium profile at each site. The sediment depth modeled ( $L$  in Figure 2) varies from site to site, as the depth at each site is based on its dissolved sulfate profile (Table 2). In this time step, the assigned values for the reactivity for organic matter and minerals (e.g., calcite and pyrite) were kept constant among all sites, but we varied the bottom methane flux to match the observed sulfate and methane gradients at the lower sections of the profiles. The time allowed in our model for the first step was calculated by dividing the modeled depth of each sediment column,  $L$ , by a sedimentation rate of 0.15 m/kyr. The

resulting time spans (200 to 400 kyrs) are long enough for sulfate profiles to reach steady state. After this time span, when the system has reached steady state, we add an instantaneous sediment layer with a thickness denoted as  $\Delta x$  (Figure 2B).

The second step of model was initiated from the steady state conditions and SMTZ depths established during the first step, with a new instantly deposited layer of sediments (i.e., the MTD) bearing fresh and reactive organic matter and sea water sulfate content of 28 mM (Figure 2B). From these initial conditions, we let the model evolve until it fits the observed pore water profiles. The thickness of this organic matter rich layer ( $\Delta x$  in Figure 2B) is unknown but is one of the two parameters that are estimated by the pore water simulation. The amount of time required to reach the current observed profile ( $\Delta t_1$  in Figure 2C) provides an indication of the time spanned since the MTD at each site. The assigned bottom methane supply was kept constant between the two steps.

#### *Porosity, formation factor, and formation temperature*

Diffusion rates of sulfate and ammonium are the most important parameters in this model assessment. To provide a realistic estimate of the diffusion rates, the porosity, tortuosity and the in-situ temperature of sediments need to be thoroughly considered. The porosity profile at each site was obtained by fitting the observed profiles (Collett et al., 2008) with the equation for depth-dependent porosity (Boudreau, 1997):

$$\phi(z) = \phi_f + (\phi_0 - \phi_f) \exp(\gamma z) \quad (27)$$

where  $\phi_f$  and  $\phi_0$  are the asymptotic porosity and porosity at the water-sediment interface, respectively.  $\gamma$  is an empirical constant obtained from data-fitting of the depth interval that covers the modeled depth (i.e.,  $L$  in Figure 2). These parameters are reported in Table 2.

In order to account for the different diffusivities of solutes in pure fluid and porous media, a tortuosity value is required to adjust the diffusion coefficients in pure media.

One way to quantify the effect of tortuosity is by calculating the formation factor (FF) from resistivity log, which tracks current flow to analogue fluid transport in the porous medium. In CrunchFlow, this can be done by providing a parameter named cementation factor ( $m$ ), which can be calculated using the FF data calculated from resistivity logs obtained from logging while drilling (LWD) and shipboard laboratory measurements with a four-pin Wenner array and a temperature probe (Collett et al., 2008). The  $m$  values calculated for each site through Archie's law (Steeffel, 2009):

$$FF = \phi(z)^{-m} \quad (28)$$

and are listed in Table 2.

In-situ temperatures were measured at each site during coring operations with the APCT-3 (advanced piston corer temperature tool 3) (Collett et al., 2008). Several temperature measurements, which include seafloor temperature, were made at each site to determine the geothermal gradient. This information is also included in Table 2.

### *Sensitivity tests*

We ran a sensitivity test to constrain the variability of  $\Delta x$ ,  $\Delta t_1$  and  $k_{OM}$  using data from Site 5C.  $\Delta x$  and  $\Delta t_1$  are primarily constrained with the sulfate profile whereas  $k_{OM}$  was constrained with both sulfate and ammonium profiles. In this exercise we used the best fit values for  $\Delta x$ ,  $\Delta t_1$  and  $k_{OM}$ , which are 13m, 1600 years and  $10^{-9.3}$  (blue lines in Figure 3), and run the model by varying these parameters from 8 to 18m (Figure 3A), 1300 to 1900 years (Figure 3B) and from  $10^{-9.5}$  to  $10^{-9.1}$  (Figure 3C). The results of this exercise indicate that our model is able to constrain the three parameters with good sensitivity and therefore it can provide a reliable quantification of the magnitude and timing of the most recent MTDs, as well as provide information on the  $k_{OM}$  in KG basin sediments.

## **Results and discussion**

### *Model-estimated MTD magnitude and age*

Our model assessment, in light of the geological background of this area, confirm our hypothesis that the S-shape sulfate profiles result from organic matter degradation driven by a rapid and recent input of fresh organic matter associated with a MTD. Our model can reproduce the observed sulfate and ammonium profiles at the seven sites where sulfate profiles indicate that the system is out of steady-state (Figure 4). The MTD thickness ( $\Delta x$ ) and the time elapsed ( $\Delta t_1$ ) since the mass transfer event are summarized in Table 3. We also ran the model until it reaches a new steady state after the MTD event to estimate the maximum time the anomalous sulfate profiles can survive ( $\Delta t_2$ ).

The thickness of the MTDs estimated from the model ranges from 8 to 25 meters. Seismic profiles at Sites 10 and 12 image a shallow debris flow (Collett et al., 2008), which indirectly support our results, although the resolution is different from what we infer here (<25 m). High resolution multibeam bathymetry profiles also document prevalent and widespread distribution of mass transfer deposits in the upper and midslope areas of the K-G basin with a thickness similar in magnitude to what we estimated with our model (Ramprasad et al., 2011). Frequent observations of silt/sand laminae in the cores were also attributed to the influence of MTDs in the basin (Collett et al., 2008). However, our results show no correlation between the magnitude of the model-derived  $\Delta x$  and the frequency of laminae (Figure 4), suggesting processes other than MTD may have led to the formation of these laminae.

Using  $^{14}\text{C}$  dating, Ramprasad et al. (2011) estimated the sediment deposition rate in one MTD to be 40 m/kyr, which is much faster than the sedimentation rate for the other hemipelagic sequence in their study (2.1m/kyr).  $^{14}\text{C}$  dating from Mazumdar et al. (2012) also revealed a dramatic change in sedimentation rate between two deposition modes (i.e., hemipelagic sediment rain vs. MTDs). We can estimate an average deposition rate for each mass transfer event by dividing the thickness of the slump deposit by the time elapsed since deposition ( $\Delta x/\Delta t_1$ ) (Table 3). Our values are similar to those of Ramprasad et al. (2011) and similar or higher than those of Mazumdar et al. (2012). We also observe a positive correlation between the average deposition rate of each mass transfer event with water depth (Figure 5), if we exclude Site 15A. This correlation suggests that sites in

deeper water receive more sediments than those on shallower sections of the slope, which agrees with the previous observations in this region (Ramprasad et al., 2011).

#### *Sulfate reduction dynamics at Site 15A*

At all sites except for Site 15A, the model is able to reproduce the observed ammonium and sulfate profiles using  $k_{OM}$  values ranging from  $10^{-9.1}$  to  $10^{-9.5}$  moles /m<sup>2</sup>/sec. These values result in a depth-integrated POCSR rate ( $R_{POCSR}$ ), which equals to the total sulfate reduction rate, in the MTD section of 149 to 623 mmol SO<sub>4</sub><sup>-2</sup>/m<sup>2</sup>/yr (Table 3). POC (particulate organic matter) degradation rates estimated by Wallmann et al. (2006) from the sediments of the Sea of Okhotsk and Blake Ridge range from 2.8 to 122 mmol SO<sub>4</sub><sup>-2</sup>/m<sup>2</sup>/yr. Dale et al. (2008) estimated the organoclastic sulfate reduction rate from the coast of Denmark to be as high as 1150 mmol SO<sub>4</sub><sup>-2</sup>/m<sup>2</sup>/yr. Chuang et al. (2013) recently estimated the contribution of sulfate reduction from organic matter degradation to be 4.2 to 47 mmol SO<sub>4</sub><sup>-2</sup>/m<sup>2</sup>/yr in southwestern offshore Taiwan. Hong et al. (2014) estimated the rates of POCSR in the sediments of Ulleung Basin to be in the range of 0.5 to 74.7 mmol SO<sub>4</sub><sup>-2</sup>/m<sup>2</sup>/yr. The rates we estimated for the K-G basin are on the high end of these estimates, which may be due to the fact that we estimated the  $R_{SR}$  by integrating over the 8 to 25 m-thick MTD sections. These depth sections are two to five times thicker than the typical thickness of the sulfate reduction zone, which is only a couple meters at these other sites.

The sulfate profile from Site 15A is distinctly different from the other six sites in two ways. First, the first measurement at 1.4 mbsf yielded only 8.27 mM of sulfate (Figure 4), which is significantly lower than the bottom seawater value. Such low sulfate content together with the low initial porosity measurement (69.75% at 0.78 mbsf) suggests that the top of the sediment column at this site may have been removed by a recent erosional event (Figure 6A). Second, the drop of sulfate concentration in the upper 9 m of the hole is more dramatic compared to other sites (Figure 4). In order to match the observed, unique sulfate and ammonium profiles at Site 15A, we have to assign a distinctly higher  $k_{OM}$  that results in a higher  $R_{POCSR}$  (1215 mmol SO<sub>4</sub><sup>-2</sup>/m<sup>2</sup>/yr; Table 3) at this site. This difference may suggest that the organic matter at this site may be more labile than other

sites; however, the characterization of organic matter composition and provenance (Phillips and Johnson, this volume) at this site does not support this inference.

Another explanation for the higher  $R_{\text{POCSR}}$  is that the initial sulfate concentration when MTD deposited at Site 15A is not sea water value as what we assigned in the model (Figure 2B). Therefore, a  $R_{\text{POCSR}}$  similar to other sites and lower initial sulfate content can result in the current pore water profile observed at Site 15A. We hypothesized that a layer of MTD deposited at Site 15A with its pore water composition unaltered. The upper portion of this MTD was later removed by another erosion event and result in the lower porosity currently observed (Figure 6A). The remaining sulfate in the intact part of the MTD was consumed by POCSR at a rate similar to other sites (Figure 6B). These combined processes result in the different sulfate profile observed at Site 15A (Figure 6C). This inference, however, assumes unchanged pore water profiles during mass transport, which does not seem to be very realistic. Although no satisfactory conclusion is arrived at this point, the combined data reveal suggest the very dynamic conditions at Site 15A.

#### *Influence of MTDs on pore water profiles*

Although only sulfate and ammonium profiles are modeled in this study, we expect MTDs to influence the distribution of all pore water species as the entire system is still in a transient state. Therefore, any inferred reaction that assumes a steady state condition will result in erroneous conclusions and rate estimates. For example, our model results question the postulated new metabolic pathway by Schrum et al. (2009). These authors explain the low ammonium concentration observed within the first sulfate reduction zone at Site 14A as indicative of a sulfate-reducing ammonium oxidation reaction. Although their estimates of Gibbs energies for the reaction support the potential role of this metabolic process, our model clearly demonstrates that the sulfate and ammonium profiles of the K-G basin can be well explained by rapid deposition of sediment (Figure 2B), and do not necessarily require a sulfate-reducing ammonium oxidation reaction.

S-shape sulfate profiles have been reported by Hensen et al. (2003) in the west Argentine Basin. They explained such profiles as resulting from two independent slides, each of which brought a sediment package with distinct pore water compositions. The different pore water compositions from these two sediment packages, which are also different from the bottom water composition, reflect the different origins of the sediment sections. By numerically simulating this scenario, Hensen et al. (2003) concluded that the sedimentary process leading to the observed sulfate profile must have happened very recently (i.e., several tens of years). Holstein and Wirtz (2010) observed similar sulfate profiles on a tidal sand flat sediment along the northern Germany coast. They explained this observation as resulting from a rapid organoclastic sulfate reduction fueled by a downward transport of labile organic matter during flat progression. In both cases, the authors agreed upon the transient nature of the observed S-shape profiles, and propose episodic sediment pulses as their causal mechanisms. The fast sedimentation in the shallow part of sediment column rapidly buries sulfate before it diffuses out or it is entirely consumed. Such sulfate burial results in the section with almost constant sulfate concentration. If this is the only process altering sulfate profile, then “kink type” profiles of sulfate (Zabel and Schulz, 2001; Hensen et al., 2003) may be expected. Consumption of sulfate through POCSR in the section with rapid sedimentation is required for the s-shape profiles, as were observed in the K-G Basin, Argentine Basin, northern Germany coast, and probably elsewhere along continental margins worldwide.

The MTDs inferred from our analyses of pore water data from the K-G basin are much larger in scale and significantly older than those discussed previously, which span only 2-8 meters in thickness and are thought to reflect events that occurred several tens of years before sampling (Hensen et al., 2003 and Holstein and Wirtz, 2010). By simulating the profiles until they reach a new steady state (Figure 2D), we estimated the maximum amount of time ( $\Delta t_2$ ) that these anomalous sulfate profiles can survive to range from 2000 to 3800 years (Table 3). Mazumdar et al. (2009) observed the similar s-shape sulfate profile from a site close to the Site 10D in our study. The rapid sedimentation for the first 6 meters of their sediment core suggests influence from MTDs which were dated as ~5 kyr old. Collectively, our results and the dating from Mazumdar et al. (2009) suggest that

such S-shape sulfate profiles may survive longer than previously assumed, if MTDs are large enough in scale. The fact that we observed the influence of MTDs from the seven sites over 90 km in the basin is consistent with the observations of the widespread occurrence of MTDs in the K-G Basin. However, our modeling approach identified the influence of MTDs from some sites that were not recognized by geophysical or core observations, and points to the value of this technique in identifying MTDs and quantifying their magnitude and age.

## Conclusions

By simulating the pore water sulfate and ammonium concentrations measured at seven sites drilled in the K-G Basin during the NGHP-01 expedition, we provide a quantitative description of how the MTDs can affect the geochemistry profiles. Our model provides reliable estimates of the MTDs thickness ( $\Delta x=8-25$  meters), the time elapsed after the most recent event ( $\Delta t_1=450$  to 1600 years), and the organoclastic sulfate reduction rate ( $R_{\text{POCSR}}=126$  to 1215 mmol  $\text{SO}_4^{2-}/\text{m}^2/\text{yr}$ ) at these seven sites. We also estimated the time required for the system to reach a new steady state after the MTD events ( $\Delta t_2=2000$  to 3800 years).

If we exclude site 15A we observe a positive correlation between water depth and the average depositional rate ( $\Delta x/\Delta t_1$ ), in agreement with the previous observations of mass transport processes in this basin. The depth-integrated sulfate reduction rates estimated here are higher than published values from other sites. This is because the rates in the K-G basin were estimated by integrating over sediment depths that correspond to the thickness of the MTDs, and are two to five times thicker than the sulfate reduction zone in other studies. Site 15A is anomalous in its sulfate and porosity data which suggest that this site may be more dynamic than the other study sites.

We caution against using the pore water profiles of sites experiencing significant MTDs to infer metabolic processes before considering the role that sediment transport can have on the pore water distributions. In particular, we question the postulated sulfate-reducing ammonium oxidation pathway by Schrum et al. (2009), based on the low ammonium

concentration observed within the first sulfate reduction zone at Site 14A. The results from our model show that the data at Site 14A reflects a non-steady state condition triggered by MTD in this basin.

### **Acknowledgement**

The authors would like to thank co-chief scientists, captain, crew members and science party during the NGHP-01 expedition for their assistance with sample collection and onboard analyses. Funding support from Department of Energy (DE-FOA-0000668, DE-FE-0010496) for this work is also greatly appreciated.

## References

- Bastia R (2004) Depositional model and reservoir architecture of tertiary deep water sedimentation, Krishna-Godavari Offshore Basin, India. *Journal of the Geological Society of India* 64: 11-20
- Borowski WS, Paull CK & Ussler W (1999) Global and local variations of interstitial sulfate gradients in deep-water, continental margin sediments: Sensitivity to underlying methane and gas hydrates. *Marine Geology* 159: 131-154
- Boudreau BP (1997) Diagenetic models and their implementation: modeling transport and reactions in aquatic sediments. Springer, Berlin
- Chuang PC, Dale AW, Wallmann K, Haeckel M, Yang TF, Chen NC, Chen HC, Chen HW, Lin S, Sun CH, You CF, Horng CS, Wang YS & Chung SH (2013) Relating sulfate and methane dynamics to geology: Accretionary prism offshore SW Taiwan. *Geochemistry Geophysics Geosystems* 14: 2523-2545
- Claypool G & Kaplan I (1974) The Origin and Distribution of Methane in Marine Sediments. In: Kaplan IR (Ed) *Natural gases in marine sediments* (p 99). Plenum Publishing Corporation, New York
- Collett T, Riedel M, Cochran J, Boswell R, Presley J, Kumar P, Sathe A, Sethi A, Lall M, Sibal V & Scientists NE (2008) Indian national gas hydrate program expedition 01 initial reports. New Delhi, India
- Dale AW, Regnier P, Knab NJ, Jorgensen BB & Van Cappellen P (2008) Anaerobic oxidation of methane (AOM) in marine sediments from the Skagerrak (Denmark): II. Reaction-transport modeling. *Geochimica Et Cosmochimica Acta* 72: 2880-2894
- Forsberg C, Solheim A, Kvalstad T, Vaidya R & Mohanty S (2007) Slope instability and mass transport deposits on the Godavari River Delta, east Indian margin from a regional geological perspective. In: *Submarine Mass Movements and Their Consequences* pp 19-27). Springer,
- Froelich PN, Klinkhammer G, Bender Maa, Luedtke N, Heath GR, Cullen D, Dauphin P, Hammond D, Hartman B & Maynard V (1979) Early oxidation of organic matter in pelagic sediments of the eastern equatorial Atlantic: suboxic diagenesis. *Geochimica et Cosmochimica Acta* 43: 1075-1090
- Hang PT & Brindley G (1970) Methylene blue absorption by clay minerals. Determination of surface areas and cation exchange capacities (clay-organic studies XVIII). *Clays and Clay Minerals* 18: 203-212
- Hensen C, Zabel M, Pfeifer K, Schwenk T, Kasten S, Riedinger N, Schulz HD & Boettius A (2003) Control of sulfate pore-water profiles by sedimentary events and the significance of anaerobic oxidation of methane for the burial of sulfur in marine sediments. *Geochimica et Cosmochimica Acta* 67: 2631-2647
- Holstein JM & Wirtz KW (2010) Organic matter accumulation and degradation in subsurface coastal sediments: a model-based comparison of rapid sedimentation and aquifer transport. *Biogeosciences* 7: 3741-3753
- Hong WL, Torres ME, Kim JH, Choi J & Bahk JJ (2013) Carbon cycling within the sulfate-methane-transition-zone in marine sediments from the Ulleung Basin. *Biogeochemistry* 115: 129-148
- Hong W-L, Torres ME, Kim J-H, Choi J & Bahk JJ (2014) Towards quantifying the reaction network around the sulfate-methane-transition-zone in the Ulleung Basin,

- East Sea, with a kinetic modeling approach. *Geochimica et Cosmochimica Acta* (in review)
- Jaynes W & Bigam J (1987) Charge reduction, octahedral charge, and lithium retention in heated, Li-saturated smectites. *Clays and Clay Minerals* 35: 440-448
- Kotha Y (2002) Sedimentology and sequence stratigraphy of hydrocarbon-bearing Mandapeta pays: A braided fluvial reservoir, Krishna-Godavari basin. *Journal of the Geological Society of India* 60: 249-270
- Mazumdar A, Dewangan P, Joao HM, Peketi A, Khosla VR, Kocherla M, Badesab FK, Joshi RK, Roxanne P, Ramamurty PB, Karisiddaiah SM, Patil DJ, Dayal AM, Ramprasad T, Hawkesworth CJ & Avanzinelli R (2009) Evidence of paleo-cold seep activity from the Bay of Bengal, offshore India. *Geochemistry Geophysics Geosystems* 10: Q06005.
- Mazumdar A, Joao HM, Peketi A, Dewangan P, Kocherla M, Joshi RK & Ramprasad T (2012) Geochemical and geological constraints on the composition of marine sediment pore fluid: Possible link to gas hydrate deposits. *Marine and Petroleum Geology* 38: 35-52
- Murthy K (1999) Continental margin of Andhra Pradesh: Some new problems and perspectives. *Visakha Science Journal* 3: 21-28
- Pattan JN, Parthiban G, Babu CP, Khadge NH, Paropkari AL & Kodagali VN (2008) A note on geochemistry of surface sediments from Krishna-Godavari basin, East Coast of India. *Journal of the Geological Society of India* 71: 107-114
- Phillips SC & Johnson JE (2014) Data Report: Long-timescale particulate carbon and nitrogen variability in the Bay of Bengal and Arabian Sea. *Marine and Petroleum Geology* (this volume)
- Prabhakar K & Zutshi P (1993) Evolution of southern part of Indian east-coast basins. *Journal of the Geological Society of India* 41: 215-230
- Ramana M, Ramprasad T, Paropkari A, Borole D, Rao BR, Karisiddaiah S, Desa M, Kocherla M, Joao H, Lokabharati P, Gonsalves MJ, Pattan J, Khadge N, Prakash Babu C, Sathe A, Kumar P & Sethi A (2009) Multidisciplinary investigations exploring indicators of gas hydrate occurrence in the Krishna-Godavari Basin offshore, east coast of India. *Geo-Marine Letters* 29: 25-38
- Ramprasad T, Dewangan P, Ramana MV, Mazumdar A, Karisiddaiah SM, Ramya ER & Sriram G (2011) Evidence of slumping/sliding in Krishna-Godavari offshore basin due to gas/fluid movements. *Marine and Petroleum Geology* 28: 1806-1816
- Schrum HN, Spivack AJ, Kastner M & D'Hondt S (2009) Sulfate-reducing ammonium oxidation: A thermodynamically feasible metabolic pathway in subseafloor sediment. *Geology* 37: 939-942
- Shanmugam G, Shrivastava SK & Das B (2009) Sandy debrites and tidalites of pliocene reservoir sands in upper-slope canyon environments, offshore Krishna-Godavari basin (India): implications. *Journal of Sedimentary Research* 79: 736-756
- Solheim A, Forsberg C, Yang S, Kvalstad T, Longva O & Rise L (2007) The role of geological setting and depositional history in offshore slope instability. *Offshore Technology Conference*.
- Solomon EA, Spivack AJ, Kastner M, Torres ME & Robertson G (2014) Synthesis of pore fluid geochemistry in the Krishna-Godavari Basin - Gas hydrate distribution

- and carbon sequestration through coupled microbial methanogenesis and silicate weathering. *Marine and Petroleum Geology* (this issue)
- Steeffel CI (2009) CrunchFlow- Software for Modeling Multicomponent Reactive Flow and Transport: User's Manual. (p 91).
- Venkatarathnam K & Biscaye PE (1973) Clay mineralogy and sedimentation in the eastern Indian Ocean. *Deep Sea Research and Oceanographic Abstracts* pp 727-738). Elsevier,
- Von Breymann MT, Collier R & Suess E (1990) Magnesium adsorption and ion-exchange in marine-sediments - a multicomponent model. *Geochimica et Cosmochimica Acta* 54: 3295-3313
- Von Breymann MT & Suess E (1988a) Magnesium in the marine sedimentary environment – Mg-NH<sub>4</sub> ion-exchange. *Chemical Geology* 70: 359-371
- Von Breymann MT, Ungerer CA & Suess E (1988b) Mg-NH<sub>4</sub> exchange on humic-acid - a radiotracer technique for conditional exchange constants in a seawater medium. *Chemical Geology* 70: 349-357
- Wallmann K, Aloisi G, Haeckel M, Obzhirov A, Pavlova G & Tishchenko P (2006) Kinetics of organic matter degradation, microbial methane generation, and gas hydrate formation in anoxic marine sediments. *Geochimica et Cosmochimica Acta* 70: 3905-3927
- Wallmann K, Aloisi G, Haeckel M, Tishchenko P, Pavlova G, Greinert J, Kutterolf S & Eisenhauer A (2008) Silicate weathering in anoxic marine sediments. *Geochimica et Cosmochimica Acta* 72: 2895-2918
- Wegener G & Boetius A (2009) An experimental study on short-term changes in the anaerobic oxidation of methane in response to varying methane and sulfate fluxes. *Biogeosciences* 6: 867-876
- Zabel M & Schulz HD (2001) Importance of submarine landslides for non-steady state conditions in pore water systems - lower Zaire (Congo) deep-sea fan. *Marine Geology* 176: 87-99

Table 1: Water depth and the location of the seven study sites.

	Water Depth (m)	latitude	longitude
Site 5C	945	16°01.722N	82°02.677E
Site 7B	1285	16°31.2785N	82°40.8672E
Site 10D	1038	15°51.8609N	81°59.0749E
Site 12A	1038	15°51.8609N	81°59.0749E
Site 14A	895	16°03.5577N	82°05.6218E
Site 15A	926	16°05.6983N	82°09.7467E
Site 20A	1146	15°48.5671N	81°50.5760E

Table 2: Input parameters for model simulations.

	L (m)	Sea floor Temperatur e (°C)	Geothermal gradient (°C/m)	m	$\phi_0^b$ (%)	$\phi_f^b$ (%)	$\gamma^b$	C/N	CEC <sup>c</sup>
Site 5C	50	7.1	0.044	2.75	77.5	57.5	-0.04	13	80
Site 7B	60	5.3	0.052	2.75	77.5	52.5	-0.04	8.5	80
Site 10D	40	6.5	0.045	3.5	77.5	63	-0.1	8.5	80
Site 12A	40	6.5 <sup>a</sup>	0.045 <sup>a</sup>	3.5 <sup>a</sup>	80	60	-0.07	12	80
Site 14A	40	7.9	0.038	2.5	77	50	-0.03	13	80
Site 15A	60	7.7	0.04	2.5	70	57.5	-0.05	14	50
Site 20A	50	5.5	0.049	2.25	80	55	-0.12	10	70

<sup>a</sup> Assuming the same as Site 10.

<sup>b</sup> These parameters were estimated from the first 40 to 60 meter of the core sediments

<sup>c</sup> cation exchange capacity

Table 3: Model-derived results ( $\Delta x$ : thickness of MTD;  $\Delta t_1$ : time elapsed after the MTD event;  $\Delta t_2$ : times requires to reach a new steady state;  $k_{OM}$ : kinetic constant for POCSR;  $R_{SR}$ : depth-integrated sulfate reduction rate)

	$\Delta x$ (m)	$\Delta t_1$ (yr)	$\Delta t_2$ (yr)	$k_{OM}$ ( $10^x$ moles/m <sup>2</sup> /sec)	$\Delta x/\Delta t_1$ (m/kyr)	$R_{SR}$ in $\Delta x$ (mmol SO <sub>4</sub> <sup>-2</sup> /m <sup>2</sup> /yr)
Site 5C	13	1600	3350	-9.3	8.13	204
Site 7B	25	450	2200	-9.1	55.56	623
Site 10D	11	800	3800	-9.3	13.75	173
Site 12A	15	1050	2100	-9.5	14.29	149
Site 14A	13	1400	3800	-9.3	9.29	204
Site 15A	18	525	2000	-8.65	34.29	1215
Site 20A	8	300	3800	-9.3	26.67	126

Figure 1: map of the study area

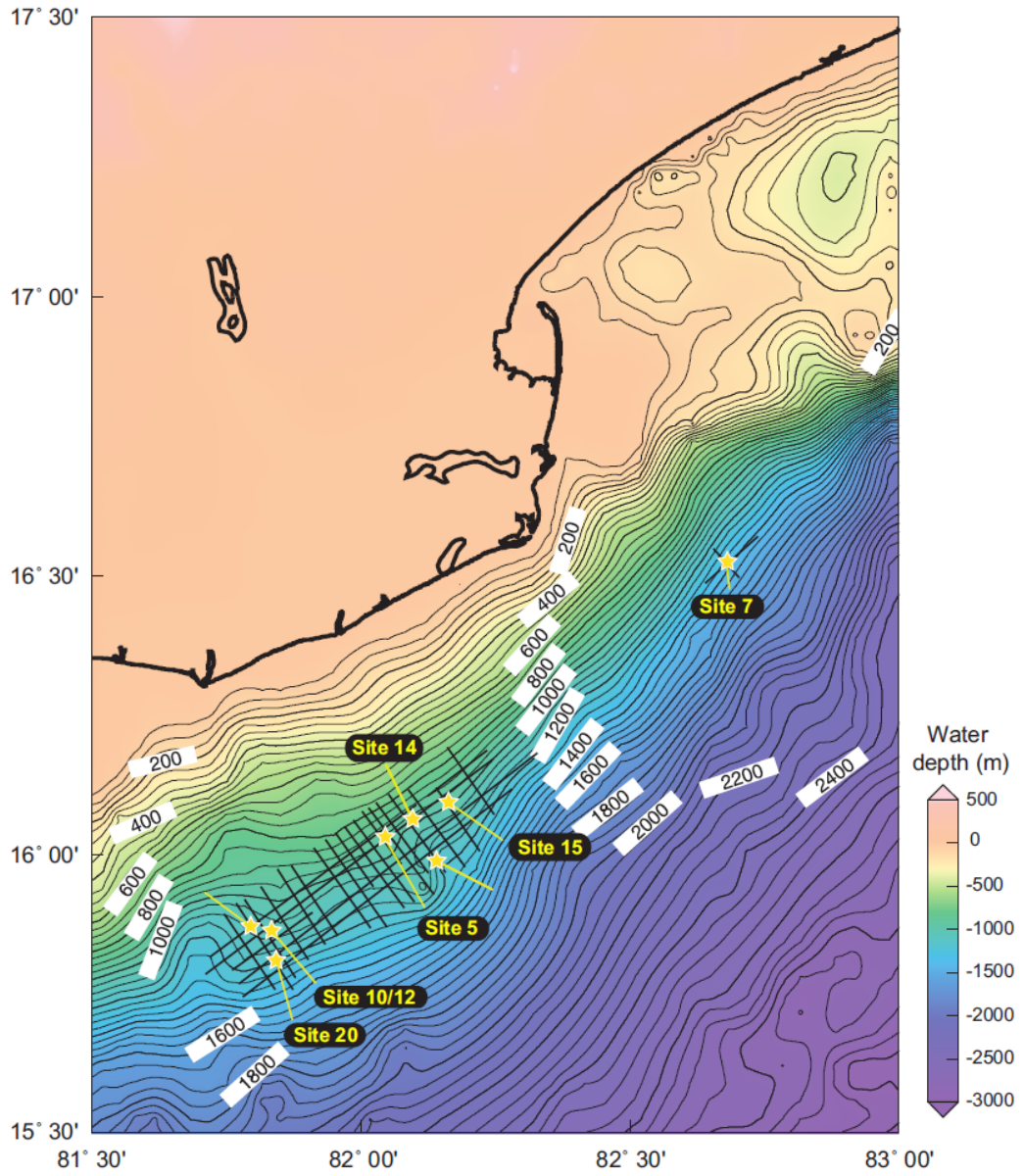


Figure 2: Schematic diagram showing the steps involved in the transport-reaction model to simulate the effect of MTDs on pore water sulfate profiles. (A) The pre-MTD pore water profiles (step 1) were set by simulating a L-meter long sediment column to steady state using sea water composition as the initial condition. Methane flux assigned here is constrained by the both sulfate and methane profiles (i.e., the assigned methane flux has to be at least higher than the observed flux). (B) The MTD (the grey rectangle) with fresh labile organic matter is deposited instantaneously onto the sediment column and buries the SMTZ to a greater depth. (C) In step 2, the pore water profiles and methane flux resulting from step 1 are used as the initial condition. Due to the addition of reactive labile organic matter in the MTD, sulfate is consumed at shallow depth through POCSR (the first sulfate reduction zone) whereas methane exhausts sulfate from below by AOM (the second sulfate reduction zone). The SMTZ in (B) and (C) illustrate this non-steady-state condition, which is observed at seven KG basin sites. The  $\Delta x$  (thickness of MTD) and  $\Delta t_1$  (time required to reach present observed profile) are estimated by fitting data at each site and are reported in Table 3. (D) The system is expected to reach another new steady state condition after  $\Delta t_2$  years (Table 3).

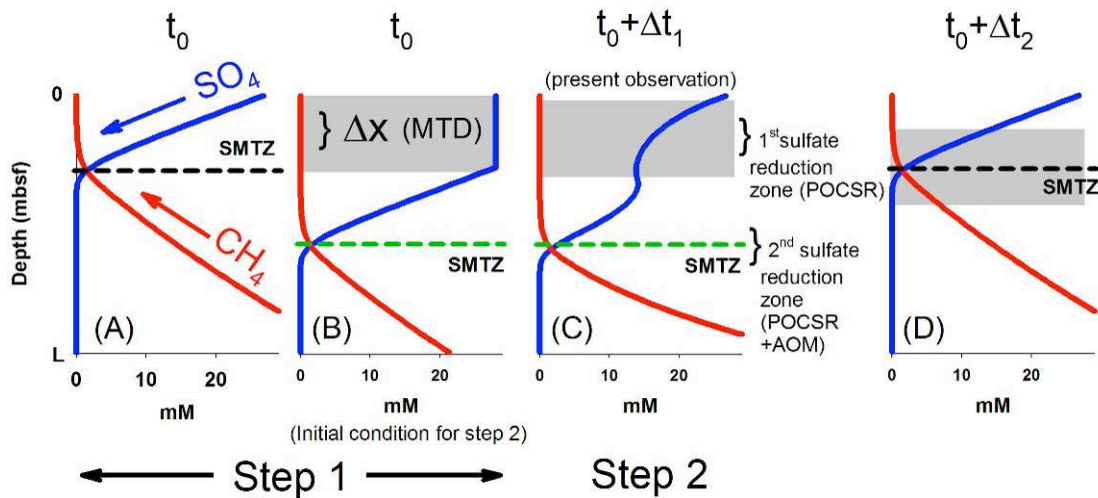


Figure 3: Simulation conducted at Site 5C to test the sensitivity of the model to the  $\Delta x$ ,  $\Delta t$  and  $k_{OM}$  parameters. Blue lines in each panel indicate the best fit to the data, and red lines show changes that would result from small variations in the values assigned to these parameters. As the results indicate, the three parameters can be well constrained by fitting the observed sulfate and ammonium profiles.

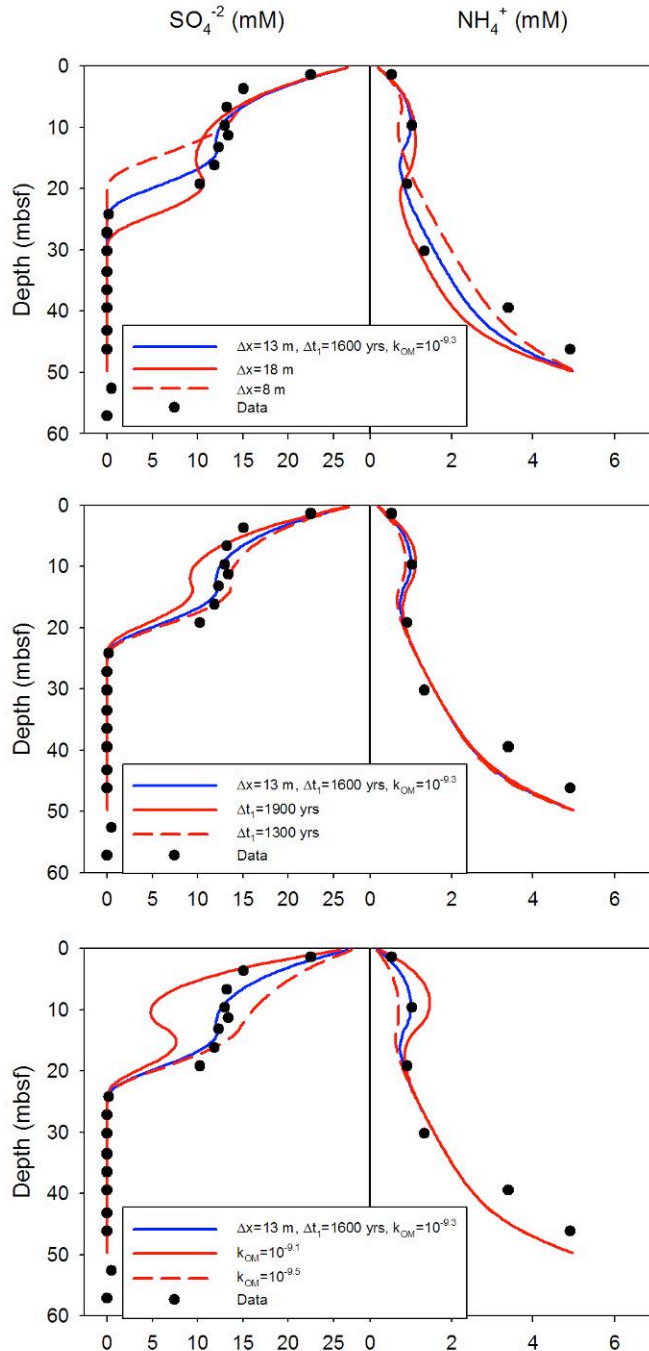


Figure 4A: Model results and the observed sulfate (blue lines and circles), methane (red lines and squares), and ammonium (pink lines and diamonds) profiles at the seven study sites. The depths where thin silt laminae and beds (grey lines) were observed at each site were also plotted for comparison although no apparent correlation was observed between the frequency of laminae and the thickness of MTDs ( $\Delta x$ , Green lines).

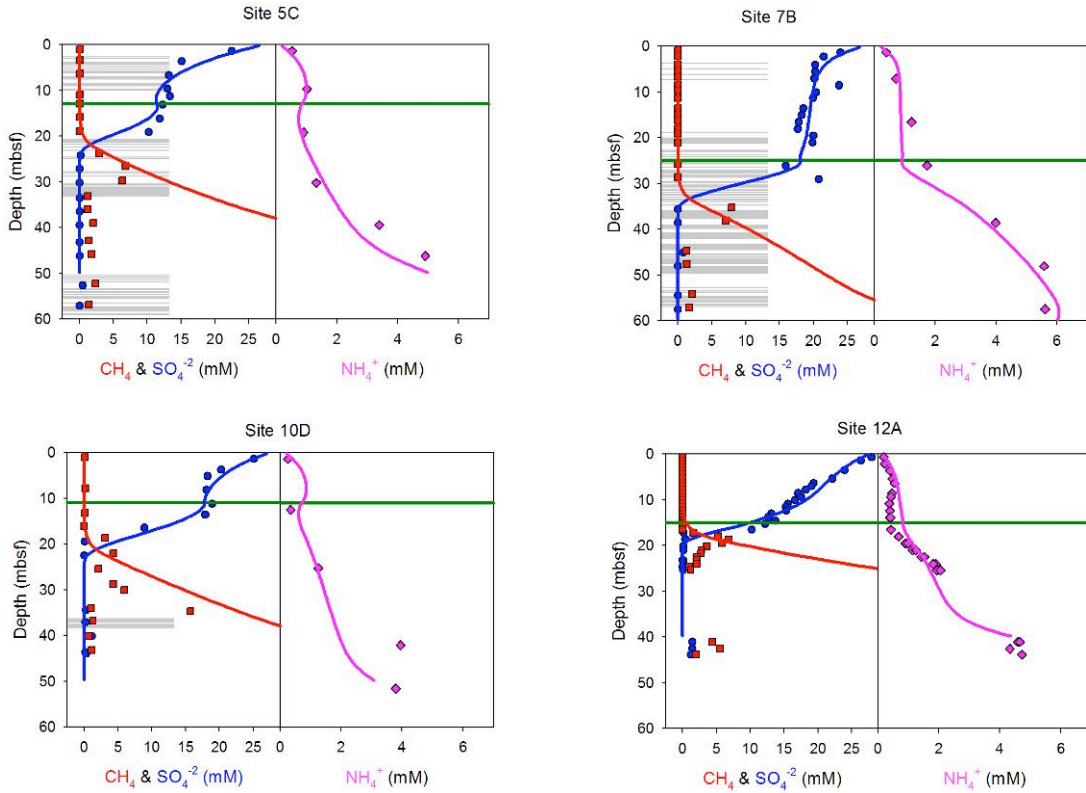


Figure 4B

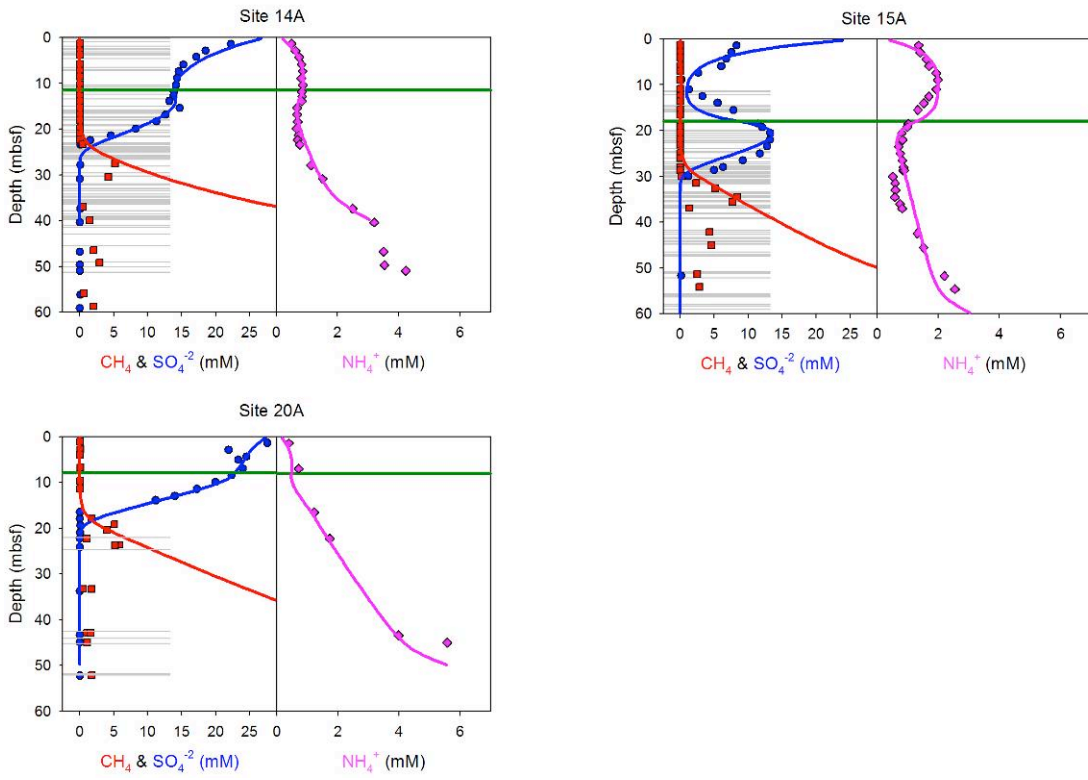


Figure 5: Correlation between water depth and the average depositional rate ( $\Delta x/\Delta t$ ). The positive correlation, if Site 15A is excluded, suggests that sites at greater water depth receive more sediments than those located in shallower water. In order to fit the sulfate profile in Site 15A, a higher  $k_{OM}$  is required which may suggest more dynamic conditions at this site as described in the text.

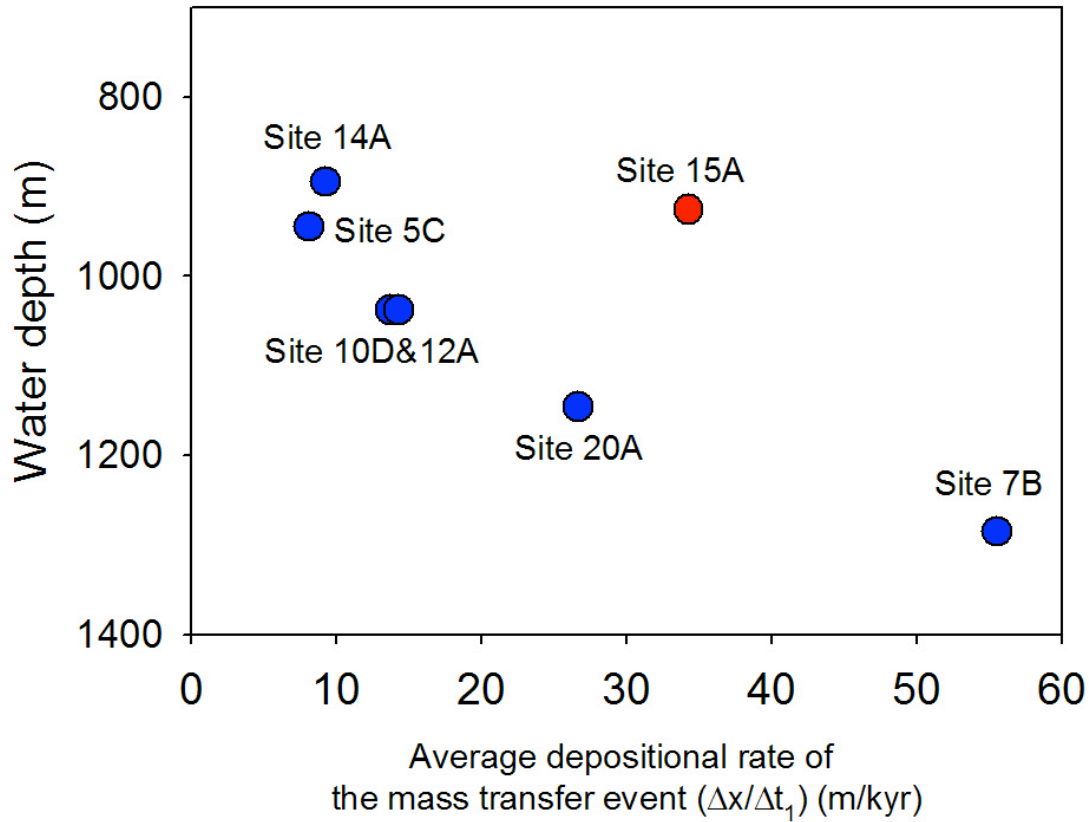
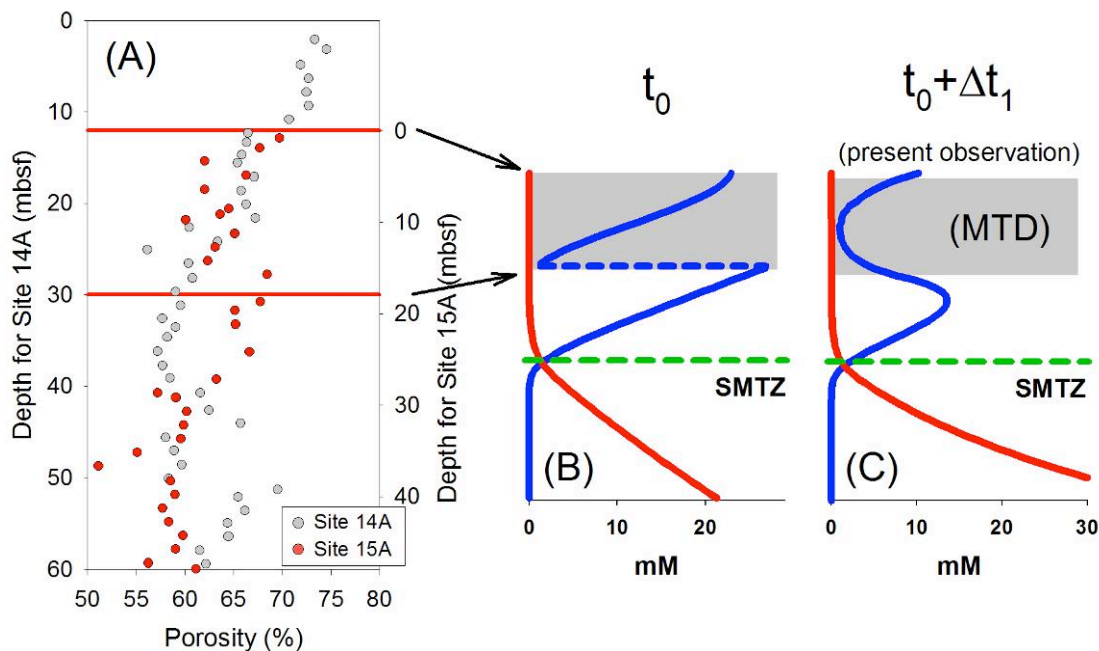


Figure 6: Conceptual model to explain the sulfate profile at Site 15A. (A) Comparison of porosity profiles between Site 14A and 15A, two adjacent sites. The first measurement at Site 15A is  $\sim 5\%$  lower than that at Site 14A suggesting that the MTD section in Site 15A may have undergone recent erosion. The two red lines mark our estimated thickness of MTD at Site 15A. In contrast to the initial homogenous sulfate content in the MTD sections at all other sites (Figure 2B), the initial sulfate profile in the MTD section at Site 15B is already low in sulfate and the total depletion of sulfate within the MTD suggests that this sediment column had experienced POCSR for a period of time before the emplacement at Site 15A. Such that immediately after emplacement, the system had a sulfate distribution as shown in (B) The continuous consumption of sulfate by POCSR in the MTD section after depositing result in the present observed sulfate profile at Site 15A, as shown in (C)



## **National Energy Technology Laboratory**

626 Cochran's Mill Road  
P.O. Box 10940  
Pittsburgh, PA 15236-0940

3610 Collins Ferry Road  
P.O. Box 880  
Morgantown, WV 26507-0880

13131 Dairy Ashford, Suite 225  
Sugarland, TX 77478

1450 Queen Avenue SW  
Albany, OR 97321-2198

2175 University Ave. South  
Suite 201  
Fairbanks, AK 99709

Visit the NETL website at:  
[www.netl.doe.gov](http://www.netl.doe.gov)

Customer Service:  
1-800-553-7681

